AD-A046 354 AIR FORCE INST OF TECH WRIGHT-PATTERSON AFB OHIO SCH--ETC F/G 20/5
INVESTIGATION OF DIATOMIC CESIUM AS A LASER MEDIUM BY ABSORPTIO--ETC(U)
JUN 77 R P BENEDICT

UNCLASSIFIED AFIT/DS/PH/77-3 NL

2 OF 2
ADA
046354

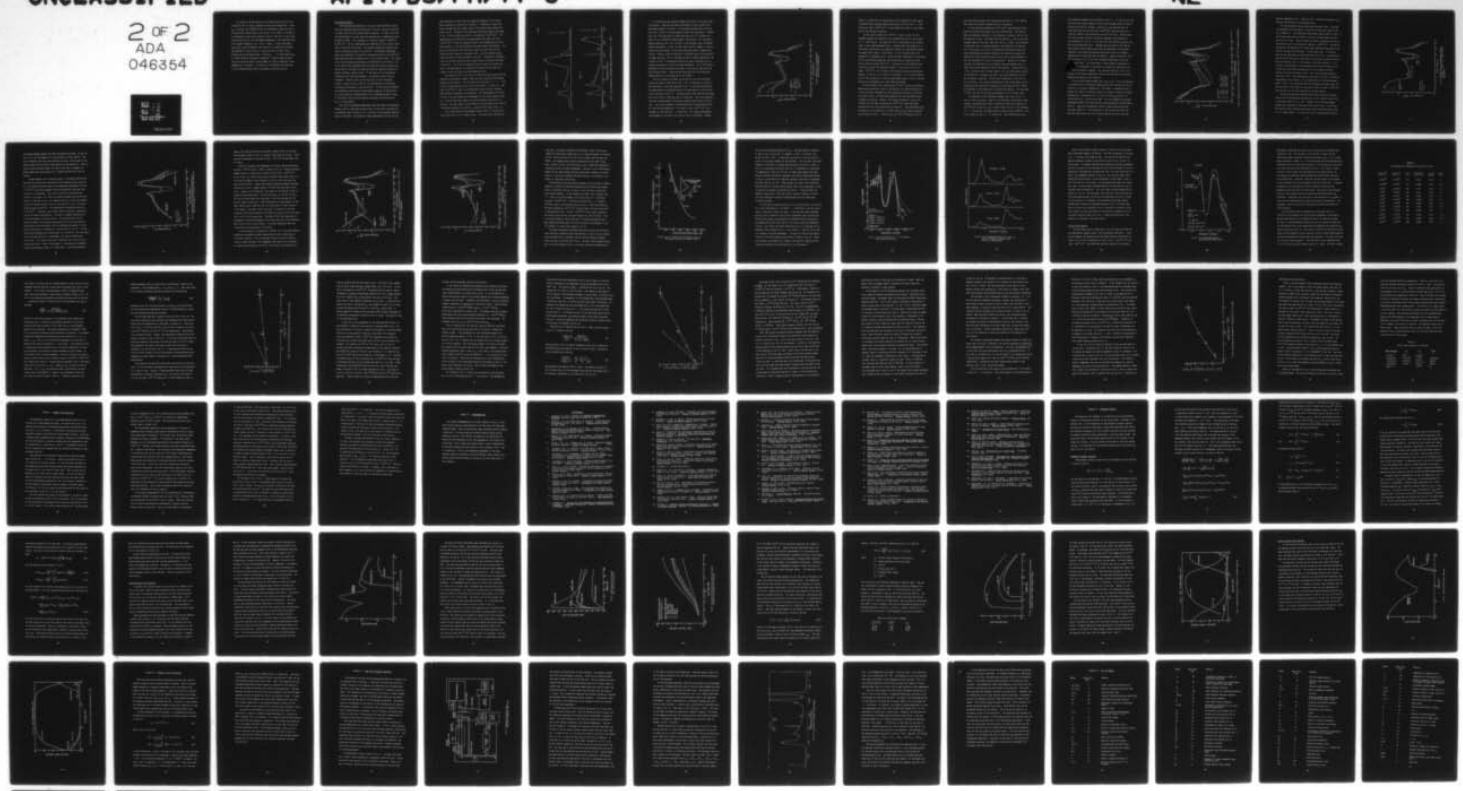

END
DATE
FILMED
12-77
DDC

The ratios of excited molecules to excited atoms can also be calculated for the $a^3\pi$ state, although with much more uncertainty. Since $K_{eq} \propto \exp(\beta D_e)$, the $[Cs_2^*]/[Cs^*]$ will be considerably larger for the $a^3\pi$ no matter which atomic state is the origin. Also, there is a factor of six advantage in statistical weights to the $a^3\pi$ over the $A^1\Sigma$ due to the spin multiplicity of 3 and the twofold degeneracy in the absolute value of the angular momentum, ($|\pm 1|$ for a π state). If only the case(c) state, $a0_u^+$, were considered, that factor of six would not be correct. The $[Cs_2^*]/[Cs^*]$ ratios of the $a^3\pi$ state are given in Table V also, assuming the parent atomic state is the $6^2P_{1/2}$. If it were the $6^2P_{3/2}$, all ratios would be increased by exp(800/T). Clearly they are quite large and one would expect a large number of $Cs_2^*(a^3\pi)$ molecules at the temperatures of interest. The ratios will be checked with those seen in the fluorescence data that is presented in the next section.

Fluorescence Results

The fluorescence experiments in $Cs/Cs_2/Xe$ were performed to determine the stimulated emission coefficient in Cs_2 per excited Cs atom and to obtain rates for the primary kinetic processes. In order to do this, the fluorescence of a Cs/Xe vapor was measured over a temperature range of 235°C to 360°C. This represents a Cs density range of 2.6×10^{15} to 6×10^{16} cm^{-3}. The Cs_2 fluorescence was normalized to the Cs atomic emission via the CsXe D1 red wing. The resultant normalized intensity was used to calculate the gain in Cs_2 per Cs^*. Fluorescence experiments were also conducted as a function of Xe density from zero to 5×10^{19} cm^{-3}. These data were used to determine the critical kinetic rates. The results of all the fluorescence experiments are presented in this section. All of the results are presented before any detailed discussion because the description of the atomic and molecular behavior required reference to several different spectral plots. If the causes of all the spectral differences were discussed piecemeal, no cohesive picture could be presented. Therefore, most of the discussion of the fluorescence results in terms of gain, kinetics, and explanations of the spectral differences are delayed to the next section. In that section estimates are presented of the inversion requirements necessary to achieve gain in Cs_2 and contain an interpretation of the fluorescence data in terms of the kinetic rates that are required to project the usefulness of Cs_2 as a laser medium.

The initial fluorescence experiments were performed with broad-band pumping, that is, there was no pump filter, so excitation occurred over a wavelength range of about 0.4 to 1.5 microns, the approximate spectral output of the lamp. The purpose of these experimental runs was to gain

some preliminary in-sight into the shape and features of the fluorescence spectrum as a function of Xe density. Furthermore, because the signal strength was much higher, many of the features were sharper and easier to see. Pictures of the unreduced fluorescence spectra are shown in Fig. 17 for no buffer gas and for a Xe density of 5×10^{19} cm^{-3}. The temperatures and Cs densities are approximately the same, 340°C and 4.5×10^{16} cm^{-3}, so the Cs_2 absorption doesn't vary between the two plots. The Xe density is the only parameter that does change significantly. Two points to mention are the fairly good signal-to-noise (S/N) and the relatively small amount of scattered light. The S/N was good because there was plenty of light incident on the cell. The amount of scattered light can be seen from the non-zero signal below 0.74 microns and above 1.28 microns. This ratio of scattered light to signal was typical for most of the experiments. Of course when a pump filter was used, the signals in the two regions just mentioned were zero.

The spectra in Fig. 17 are similar to what one would expect from the absorption experiments; however, there are some significant differences between the two spectra. For the lower one where [Xe] = 0, t[illegible] sig-nificant B-state emission from 0.76 to 0.83 microns. For the up[illegible] one, [Xe] ≈ 5×10^{19} cm^{-3}, there is no observable B-state emission implying some Xe density dependent loss mechanism. The fluorescence at line center (D1 or D2) has essentially disappeared for the high Xe density spectra. Most of that light comes out on the CsXe wings from 0.9 to 1.0 microns. The small bump at 0.84 microns is the blue satellite of the D2 line which originates from the $B^2\Sigma_{1/2}$ state of CsXe shown in Fig. 11.

All of the emission at wavelengths greater than 1.0 microns originates from the $A^1\Sigma$ or $a^3\pi$ states of Cs_2. The vibrational structure for

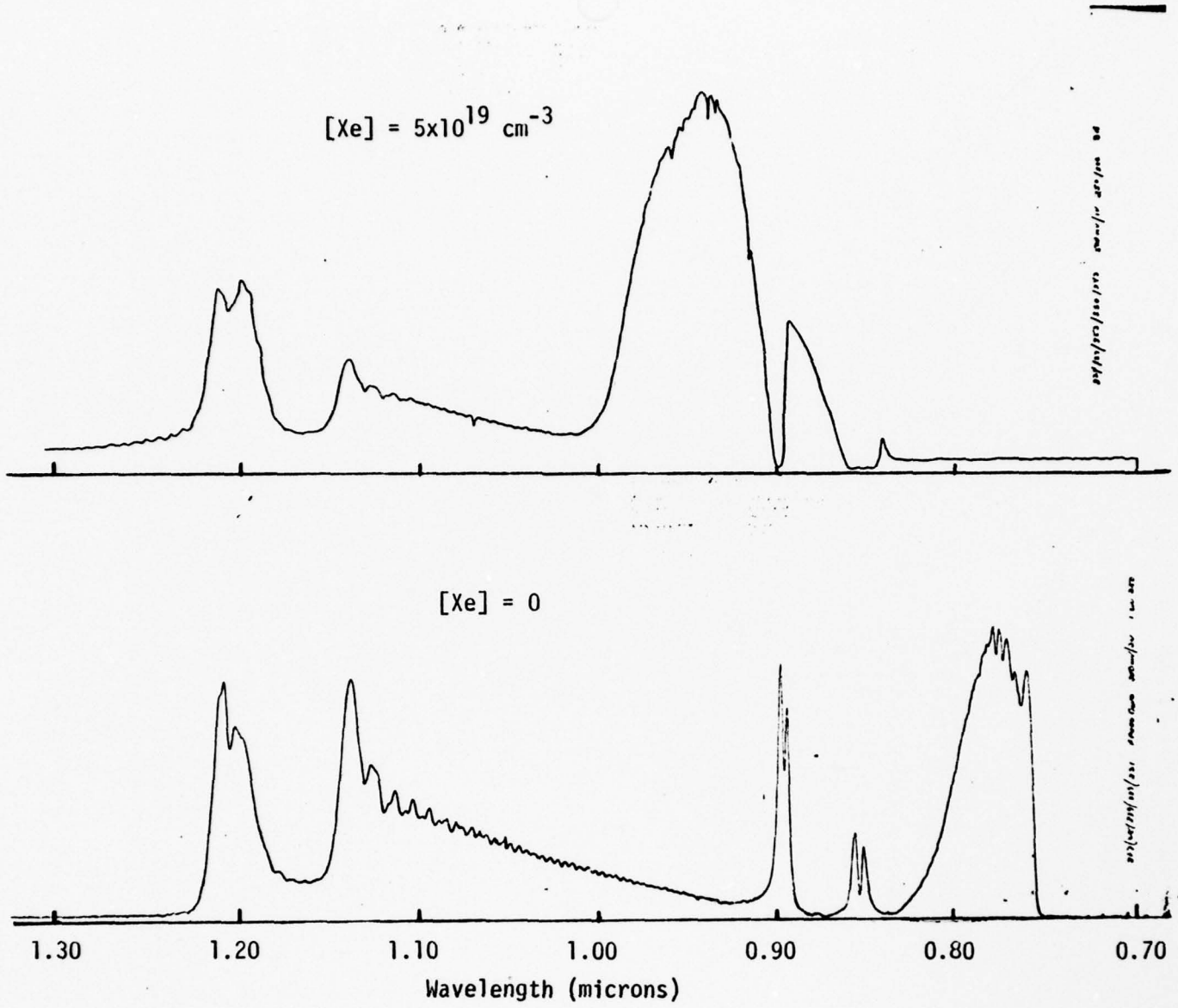

Fig 17 Cs_2 Fluorescence, Broad-Band Pumping, Unreduced Data T ≈ 340°C

λ > 1.14 microns has been smeared together much more in the high Xe density spectra. There are two other differences in the Cs_2 spectra for wavelengths beyond 1.0 microns. For the spectrum taken with no Xe present, the 1.14 and 1.21 micron peaks are about the same height. Furthermore, the 1.20 micron peak is lower than the one at 1.21 microns and there is no $a^3\pi$ emission evident beyond 1.225 microns. For the high Xe density spectrum, the 1.14, 1.20 and 1.21 micron peaks have a different height relationship. As will be seen later, they are roughly in the proportion one would expect if the A-state molecules were in thermal equilibrium. Finally, there is definite $a^3\pi$ emission beyond 1.225 microns in the upper spectrum. For all the spectra taken in these experiments, the increase of the $a^3\pi$ fluorescence relative to the $A^1\Sigma$ emission with increasing Xe pressure is one of the most noticeable. All of the features mentioned in this discussion are evident in the spectra taken with the various pump filters. They have been described using the broad-band pumped spectra as an introduction to the section.

The first question to answer was how well do the CsXe potentials predict the shape of the CsXe D1 wing. This is important as a check on the consistency of the CsXe potentials (Fig. 11) and the normalization. The experimental and predicted CsXe D1 red wing spectra for two Xe densities are shown in Fig. 18. The Atomic pump filter (the one that pumps both the D1 and D2 lines) was used for these data. The curves labeled A and B are the experimental fluorescence spectra normalized at 0.96 microns. The circles represent the predicted CsXe D1 wing predicted from Eq.1 and the CsXe potentials. For curve A, [Xe] = 5×10^{19} cm^{-3}, the agreement is very good for λ > 0.96 microns. For shorter wavelengths, the agreement is not good if only the D1 wing is considered. However,

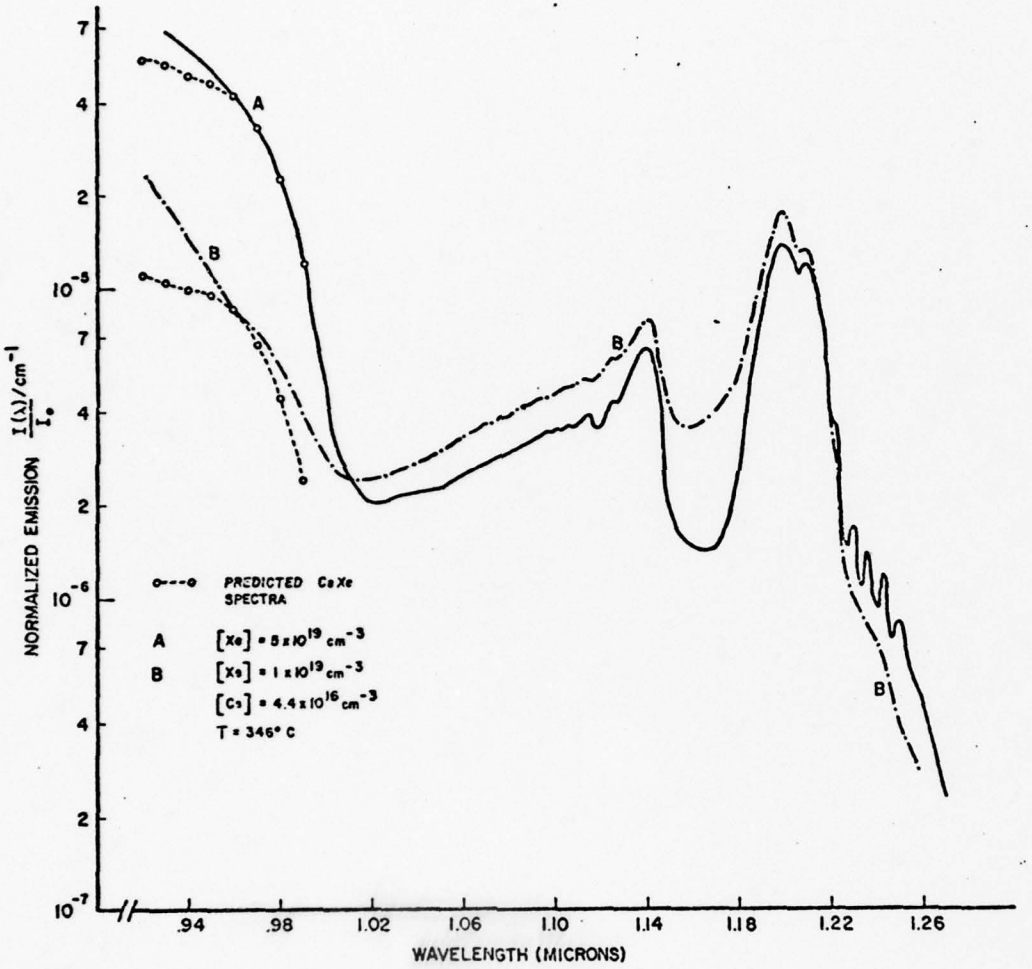

Fig 18 Normalized Cs_2 Fluorescence, Xenon Density Dependence

there is a significant D2 contribution to the intensity for that region. The observed and predicted spectra agree within 10% for $0.92 < \lambda < 0.99$ microns for $[Xe] = 5 \times 10^{19}$ cm^{-3}, if one assumes that there is one D2 atom per D1 atom and add intensities.

For the lower Xe density of 10^{19} cm^{-3}, curve B in Fig. 18, the agreement between the theoretical and observed CsXe wing is not as good for $\lambda > 0.96$ microns. The reason for this is that there is Cs_2 fluorescence in that same wavelength region. Assuming that the molecule is in vibrational equilibrium, the normalized intensity at 0.98 microns should be roughly 30% of that at 1.02 microns. As will be seen later, this assumption is reasonably valid. Using the dimer intensity at 1.02 microns, and the equilibrium assumption, the normalized Cs_2 intensity at 0.98 microns should be about 9×10^{-7}/cm^{-1}. Adding this to the predicted CsXe intensity, one gets the observed intensity. For curve B in Fig. 18 ($[Xe] = 10^{19}$ cm^{-3}), this is about a 20% correction and quite noticeable. However, in curve A, it is about a 4% correction. So it is the relative size of the Cs_2 emission in the long wavelength region of the D1 red wing that gives the appearance of a poor spectral matchup.

As the Xe density was lowered below 10^{19} cm^{-3}, the Cs_2 contribution became more significant, even at 0.96 microns, the normalization point. A trial and error procedure had to be employed to separate Cs_2 emission from that of CsXe. The CsXe shape appeared from the high density data to behave as expected. However, the relative increase of the Cs_2 contribution at the lowest Xe density (2.5×10^{18} cm^{-3}) added additional uncertainties into the normalization of about 20%. Some experiments were performed at low Cs densities ($T \sim 200°C$) where no Cs_2 could be observed and the CsXe D1 wing ($\lambda > 0.96$ microns) for 10^{19} cm^{-3} agreed within 5%

with the predicted shape first observed by HDG (Ref 27). This implies that there are no major inherent errors in the spectra.

For the spectrum obtained with 10^{19} Xe/cm^3, the wavelength region below 0.96 microns was checked for the D2 contribution. This time to match the observed intensity, it was necessary to assume a ratio of two D2 atoms per D1 atom. This means that for each $6^2P_{1/2}$ atom in the fluorescence region of the cell, there are two $6^2P_{3/2}$ atoms. The difference in the D2/D1 ratio is probably caused by the difference in Xe density. For all the spectra, this ratio increased with decreasing buffer gas. These differences are probably related to the excitation transfer between the D1 and D2 states by both Cs and Xe and to the differences in the CsXe absorption for each of the potentials. Because all of these processes are dependent on the Xe density and have unknown rates, no model could be put together to explain the behavior. Because the $6^2P_{3/2}$ - $6^2P_{1/2}$ transfer rate is larger (see Ch. II), one might expect that as the Xe density is increased, the D2/D1 ratio might decrease, and this was the behavior observed. The pertinent information is the ratio of D2 to D1 atoms. This could be determined for each fluorescence scan by subtracting the predicted D1 intensity from that measured and dividing the remainder by the theoretical D2 normalized intensity. This was done at 0.94, 0.93 and 0.92 microns and averaged to give the D2/D1 ratio.

The remainder of the differences between the curves in Fig. 18 occur in the Cs_2 spectra. These will be discussed in more detail later, however, one should notice that, although the normalized intensity for the 10^{19} cm^{-3} Xe density curve is more intense for most of the spectrum, for $\lambda > 1.22$ microns, the higher density curve has more intensity. That is the region of the $X^1\Sigma$ - $a^3\pi$ transition. This difference was even

more pronounced between the two spectra in Fig. 17. So, one can see that the buffer gas density appears to have a much stronger affect on the $a^3\pi$ emission than the $A^1\Sigma$ emission. Actually, it was expected that the normalized dimer emission for [Xe] = $5x10^{19}$ cm^{-3} would be about five times as intense as the emission for the 10^{19} cm^{-3} case. The fact that this did not occur implies a Xe density dependent loss mechanism in the denominator of Eq. 25. In the Laser Gain and Kinetics section, this will be discussed more fully. Although the variations of the fluorescence spectra with Xe density were the most pronounced, and the most important, some normalized emission spectra were taken at different temperatures for the same buffer gas density. Spectra with [Xe] = 10^{19} cm^{-3} are shown in Fig. 19 for four different temperatures using the atomic pump filter. The curves have all been reduced as described in Chapter III; normalized to line center, corrected for absorption, and corrected for spectral response. The structure seen from 1.08 to 1.14 microns at the higher temperatures could not be resolved for the lower temperatures because of the lower S/N.

The principle changes between the curves in Fig. 19 are the decrease in the CsXe wing for increasing temperature and the increase in the Cs_2 emission for increasing temperature. The former is expected from Eq. 1, whereas the latter is primarily caused by increased Cs density at higher temperatures. According to Eq. 1, a plot of $[\ln(I/I_0)]/[Cs]$ vs 1/T should give $V_u(\infty) - V_u(R)$ as the slope. This was attempted for several wavelengths beyond 1.0 microns and the slope was generally around 2000 $\pm$ 300 cm^{-1}. Based on the absorption results, these slopes should have been about 5000 cm^{-1}. The conclusion is that the excited atomic and molecular populations are not in chemical equilibrium and so the tem-

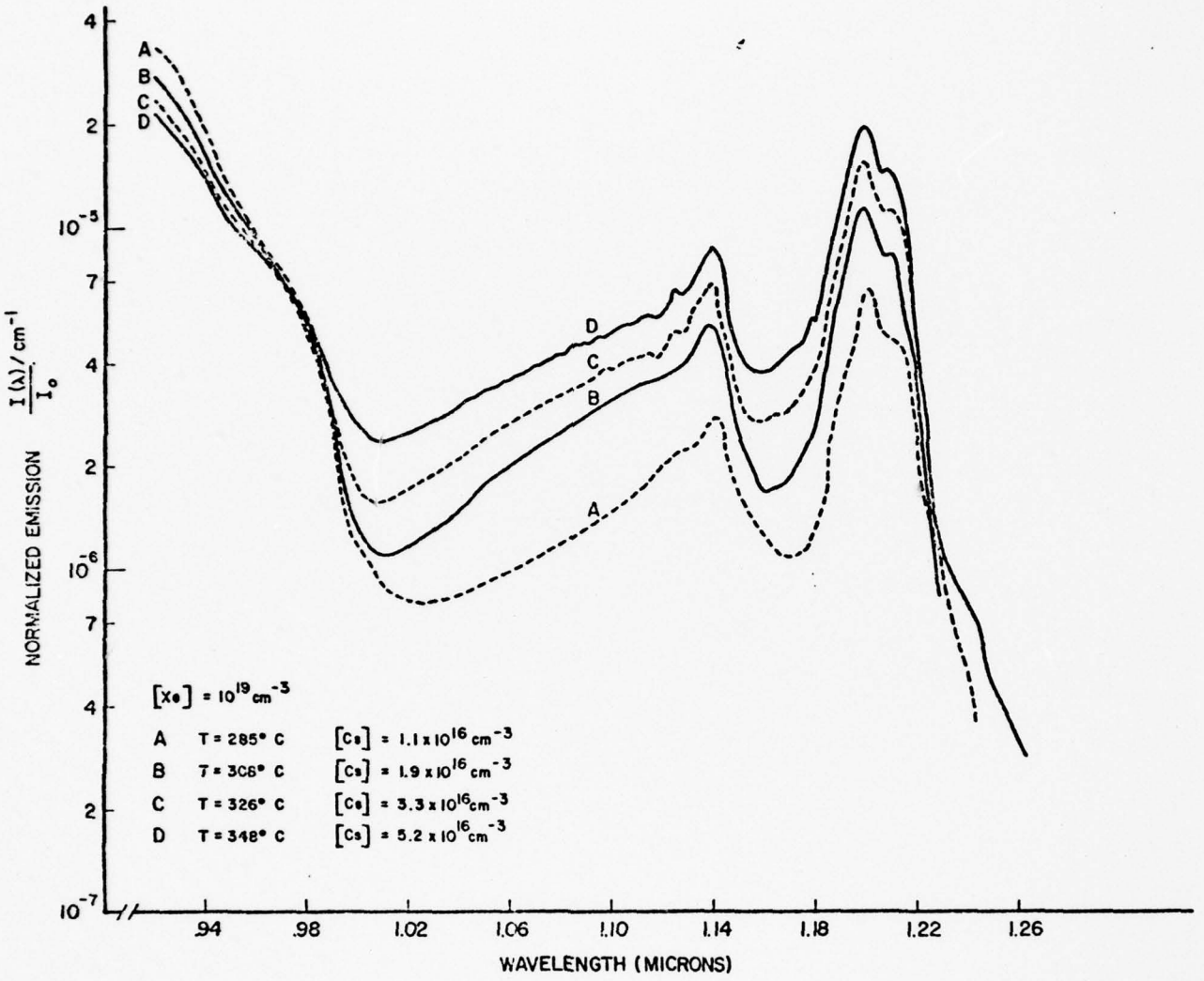

Fig 19 Normalized Cs_2 Fluorescence Spectra at [Xe] = 10^{19} cm^{-3}, Temperature Dependence

perature dependence of Eq. 1 does not hold. Evidence for molecular vibrational equilibrium will be presented later.

The next parameter that was varied was the pump filter. The pumping wavelengths for the Atomic, D1 and Dimer filters were shown in Fig. 10 in Chapter III. The normalized fluorescence spectra shown in Figs. 18 and 19 were taken with the Atomic filter that allowed pumping of both the D1 and D2 lines. Figure 20 shows the effect of pumping with each of the three filters for the highest Xe density - 5×10^{19} cm^{-3}. The spectra obtained for the Atomic and D1 filters were separately normalized to the CsXe D1 red wing at 0.96 microns. In the region 0.93 - 1.0 microns, both had the same shape, and the same D2/D1 ratio (1.0). The predicted CsXe D1 and D2 red wings are both given in the figure as dotted lines to show the relative size. In the region of the dimer emission ($\lambda > 1.0$ microns), the magnitude of the fluorescence for both the atomic and D1 filters was very similar although the D1 filter seemed to produce slightly less than the Atomic filter. This filter allowed pumping of only the D1 line. The difference was only about 10% which is within the experimental error; however, it was reproducible for different temperatures. That is, the normalized dimer fluorescence was always about 10% less for the D1 filter than for the Atomic filter, at $[Xe] = 5 \times 10^{19}$ cm^{-3}. The cause for this will be discussed in the next section.

The spectrum obtained using the Dimer filter could not be normalized to the D1 wing because there was very little intensity there (this is seen more clearly in Fig. 22). Instead, all of the dimer pumped spectra were normalized to the quasi-static satellite at 1.21 microns. This does not imply anything quantitative about the fluorescence intensity for these spectra. It only gives a way of observing the spectral

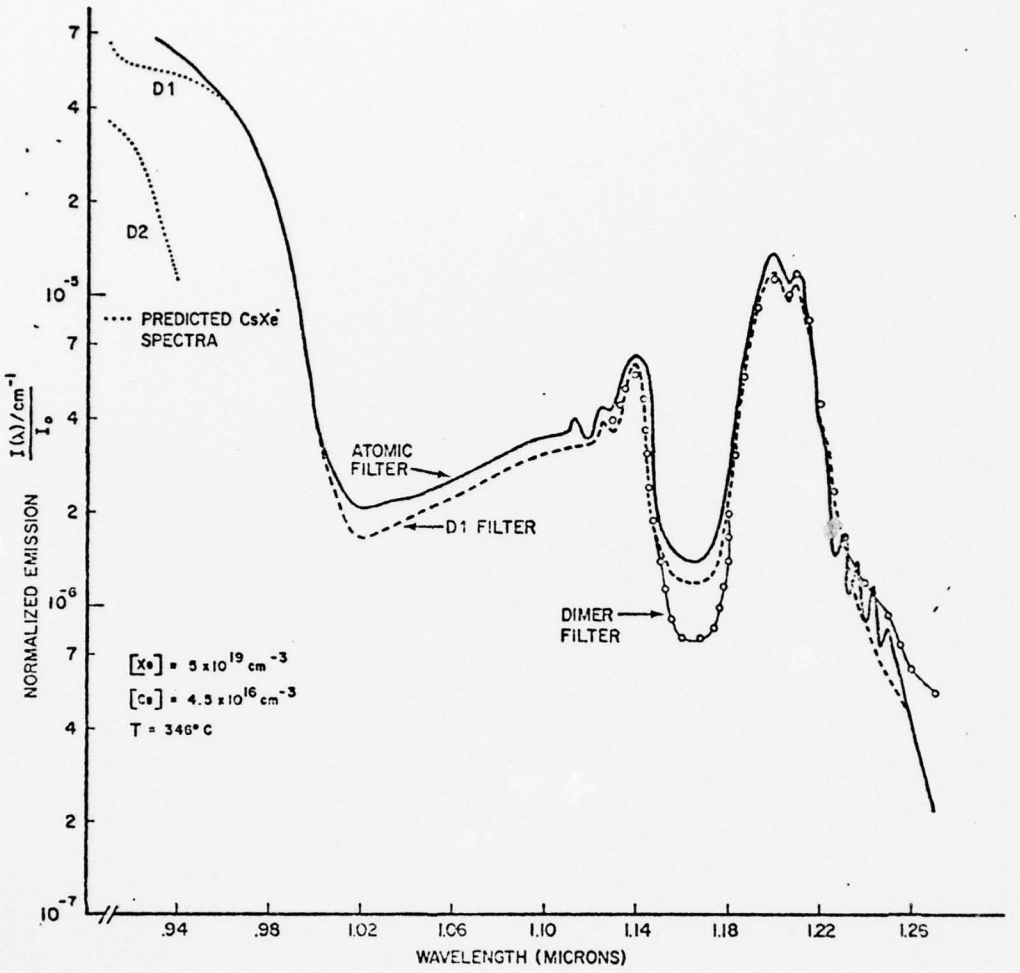

Fig 20 Normalized Cs_2 Fluorescence Spectra at [Xe] = 5×10^{19} cm^{-3}, Pump Filter Dependence

differences between pumping the dimer and pumping the atoms. As one can see in Fig. 20, the shapes of all three spectra are very similar. The only differences were that some vibration structure could be seen in the spectra taken with the atomic filter because of the better S/N. Since it does not seem to matter whether the atom or the dimer is pumped, one might assume that the molecules are in thermal equilibrium at this Xe density.

To check whether the $A^1\Sigma$ molecules were in vibrational equilibrium, the emission spectrum was calculated from the absorption data using Eq. 35. As already discussed, based on the temperature dependence for [Xe] = 10^{19} cm^{-3}, equilibrium between the excited molecular and atomic populations is not expected. This can be verified by calculating the value of I/I_o from Eq. 35. Since this equation assumes that equilibrium exists, it provides a test. For example, using Eq. 35 with the temperature and Cs density given in Fig. 20, the value of I/I_o at 1.2 microns should be about $5x10^{-4}/cm^{-1}$. The experimentally determined value was $1.3x10^{-5}/cm^{-1}$. Therefore, the excited atomic and molecular populations are not in chemical equilibrium. The cause is probably quenching and will be discussed in the next section. On the other hand, one can match the shape of the spectrum predicted by Eq. 35 and that obtained experimentally with the Atomic filter to determine the degree of vibrational equilibrium in the molecule. This was done in Fig. 21. The two spectra were adjusted to the same height at 1.10 microns. With the exception of the gap and the $a^3\pi$ fluorescence, the overall shapes agree fairly well. This implies that the $A^1\Sigma$ molecules are, close to vibrational equilibrium. There is not enough $a^3\pi$ fluorescence to determine whether that molecular state is in equilibrium. The emission spectra

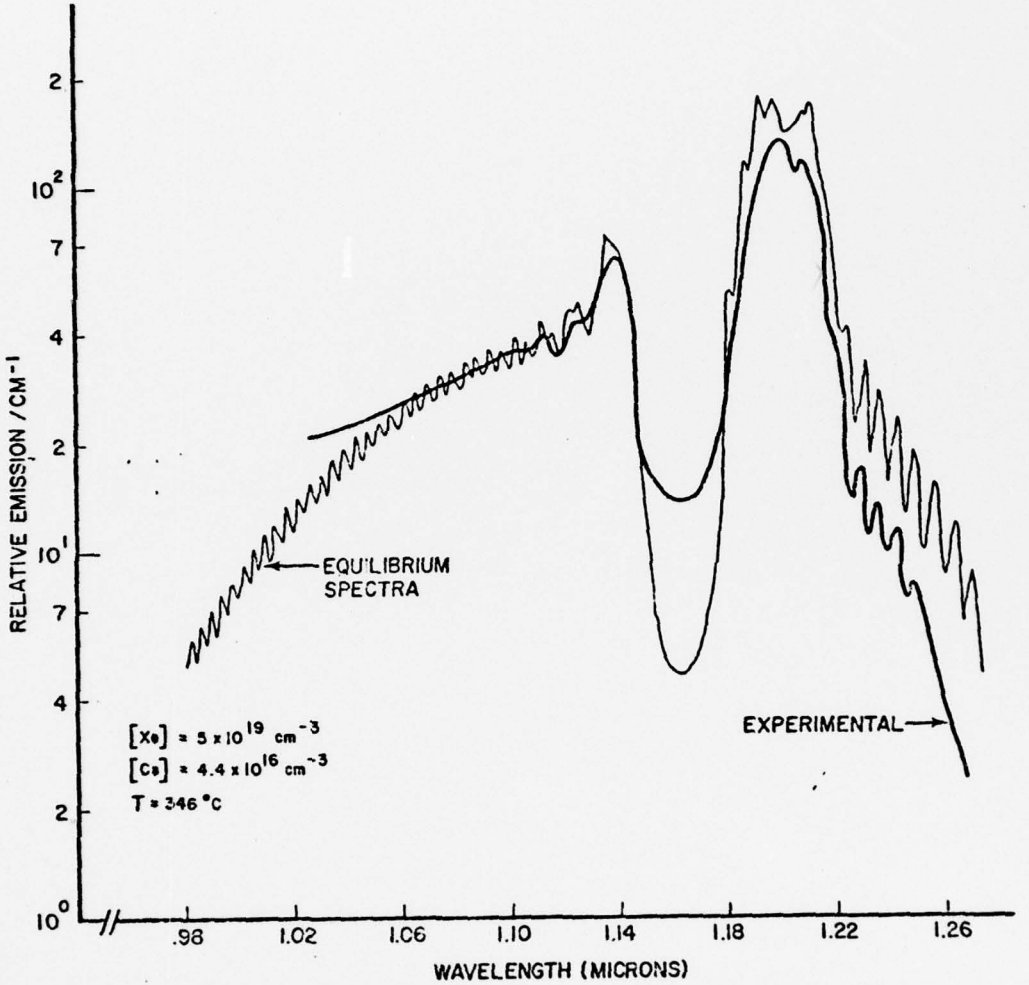

Fig 21 Normalized Cs_2 Fluorescence Compared with Equilibrium Spectra Calculated from Absorption

taken at the other Xe densities had overall shapes similar to the equilibrium spectra shown in Fig. 21, except in the region of the gap. There was more fluorescence in the gap for [Xe] < 10^{19} cm^{-3} and the Atomic and D1 filters.

A plot of the pump filter dependence of the Cs_2 normalized emission for [Xe] = 10^{19} cm^{-3} and T = 346°C is shown in Fig. 22. There are several changes from Fig. 20 which was a similar plot for [Xe] = $5x10^{19}$ cm^{-3}. First, in Fig. 22, the D1 filter gives a slightly lower D2/D1 ratio (1.5 vs 2) than the Atomic filter, whereas in Fig. 20, the ratios were the same for both filters. Second, the normalized emission spectra obtained using the D1 filter is weaker beyond 1.0 micons than the atomic filter curve. However, the differences in the region of the gap and in the $a^3\pi$ region are much more severe. Also the two peaks at 1.20 and 1.215 microns are the same height while the Atomic filter had the peak at 1.20 microns higher by about 30%. These differences are even sharper for the dimer pumping and,in addition, the 1.14 micron peak is larger relative to the others. The hump in that curve near 1.01 microns is just the scattered light coming through the transmission region of the filter (see Fig. 10 for filter transmission). The Dimer filter curve continues to get weaker at shorter wavelengths so that there was very little radiation near the D1 line (or the D2 either). This again emphasizes that very little molecular dissociation is occurring.

As the Xe density is lowered still further, all of the above effects become more pronounced, probably because they relate to some type of collisional transfer. This is discussed further in the next section. Figure 23 shows the pump filter dependence when there is no Xe present. All spectra were normalized to 100 at 1.215 microns since there was no

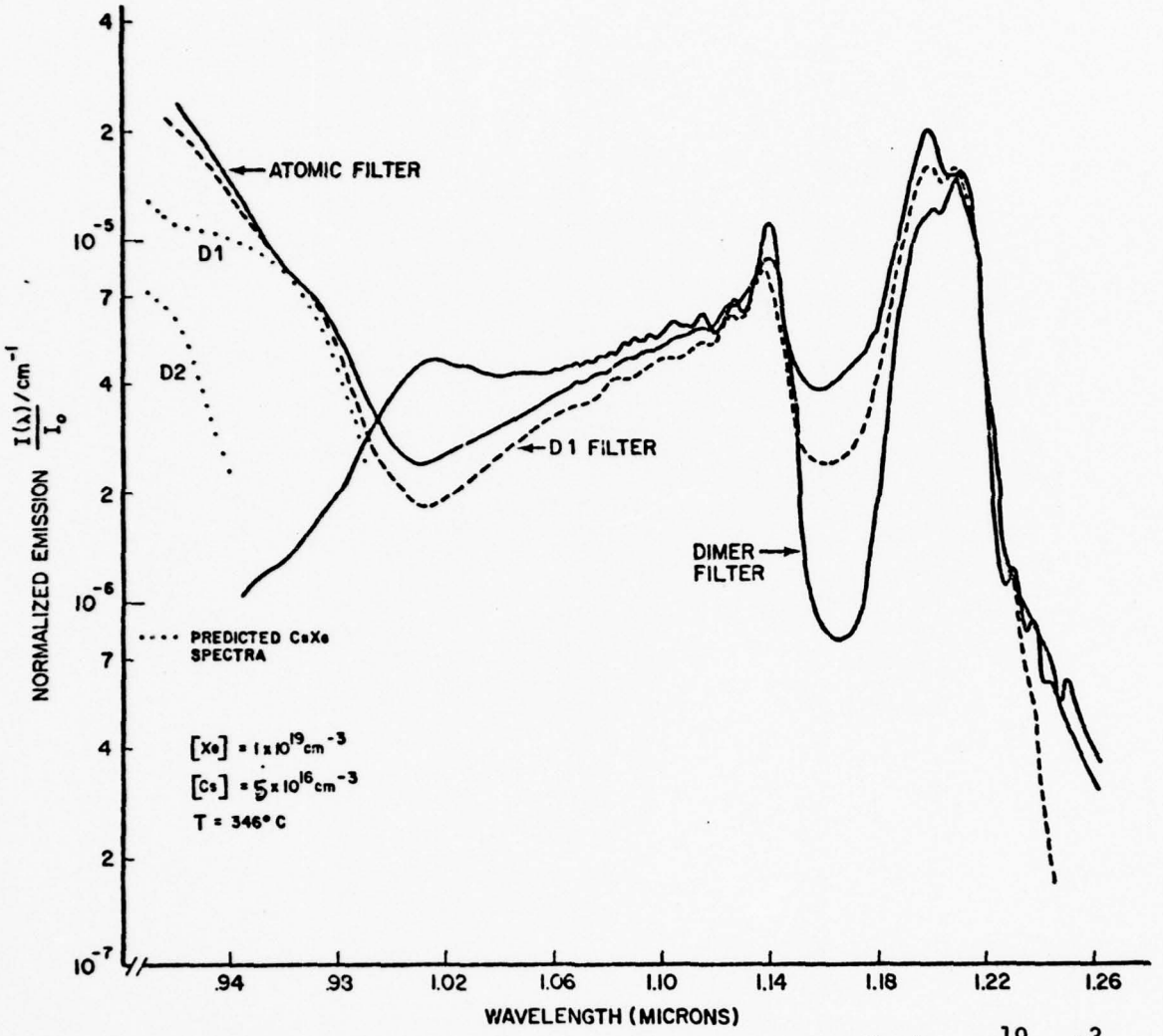

Fig 22 Normalized Cs_2 Fluorescence Spectra for [Xe] = 10^{19} cm^{-3}, Pump Filter Dependence

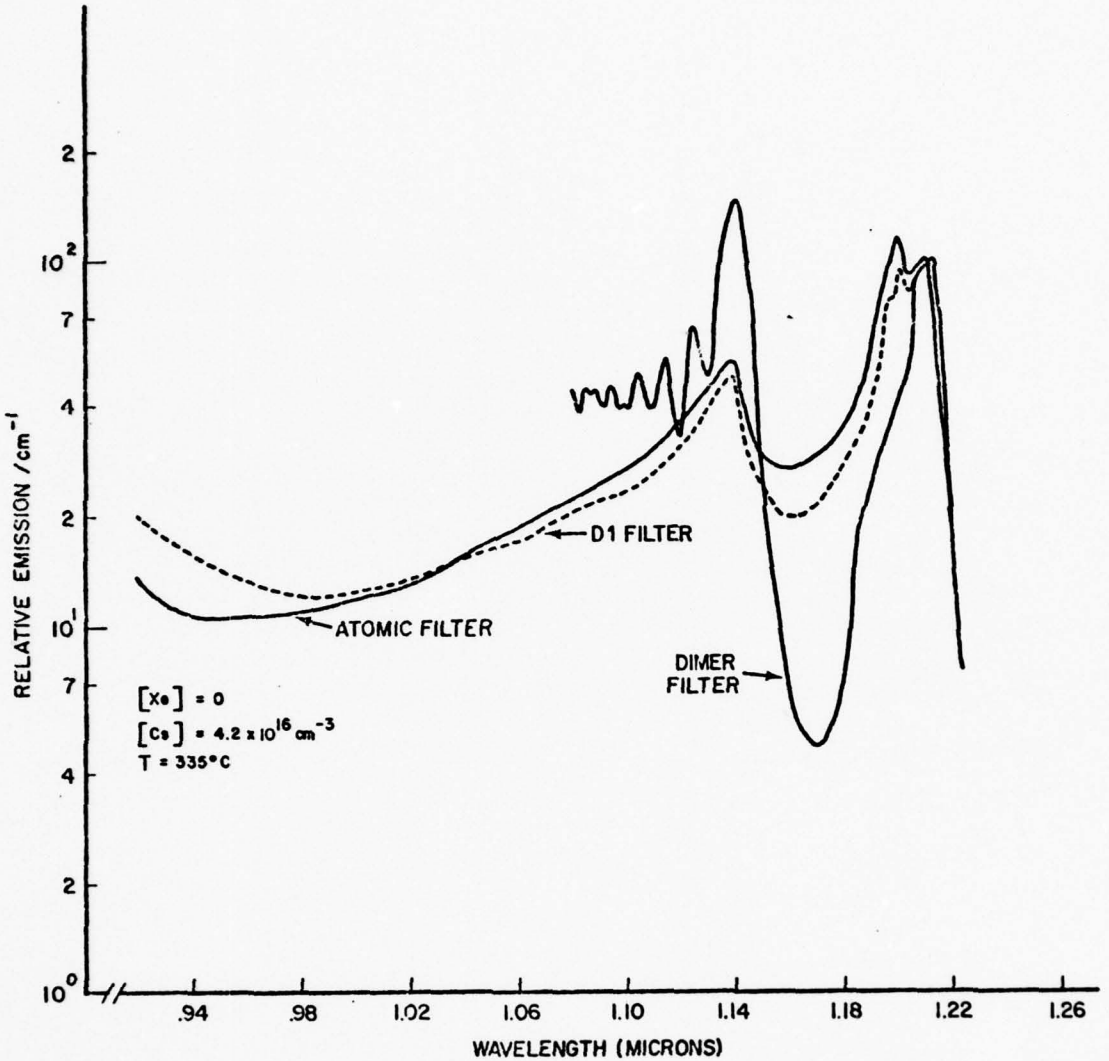

Fig 23 Cs_2 Fluorescence Spectra for [Xe] = 0, Pump Filter Dependence

CsXe wing. The spectra obtained with the Atomic and D1 filters have roughly the same shape, except there is no intensity beyond 1.22 microns and the 1.20 micron peak for the D1 curve is weaker and narrower than before. The changes again are most pronounced for the Dimer filter. Here, relative to the 1.215 micron peak, the 1.14 peak has dramatically increased and the 1.20 peak disappeared. The gap is still significantly deeper for the dimer pumping and more vibrational structure is visible. Clearly, in the case of pumping the dimer directly, the molecule is no longer in vibrational equilibrium.

The conclusion from these spectra appears to be that when a $Cs_2^*(A^1\Sigma)$ molecule is formed by three-body formation with no buffer gas present, there is sufficient time for, at most, a few collisions to begin the equilibration process. If one assumes gas kinetic cross sections, the V - T rates, with no Xe present, are of the order of $5 - 10 \times 10^7$/sec for $[Cs] = 4.5 \times 10^{16}$ cm^{-3}. Since the radiative rate, Γ_2, is about $2 - 4 \times 10^7$/sec, only a very few collisions can occur. When the Xe density has been increased to 5×10^{19} cm^{-3}, there are many collisions that occur in one radiation time. For $[Xe] = 5 \times 10^{19}$ cm^{-3} and, again, assuming a gas kinetic cross section, one would expect over 100 collisions. This is evidently enough to equilibrate the $A^1\Sigma$ molecular population even when pumping the dimer where the initial molecular distribution in the $A^1\Sigma$ potential is roughly that shown in Fig. 23.

The spectra obtained from pumping the dimer directly can be used to infer some more information about the potential curves of Cs_2 as follows. Figure 24 shows the $A^1\Sigma$ potential and the relative pumping intensity within the well, using the Dimer filter. The most intense pumping occurs near 1.01 microns because that is the region of maximum transmission of

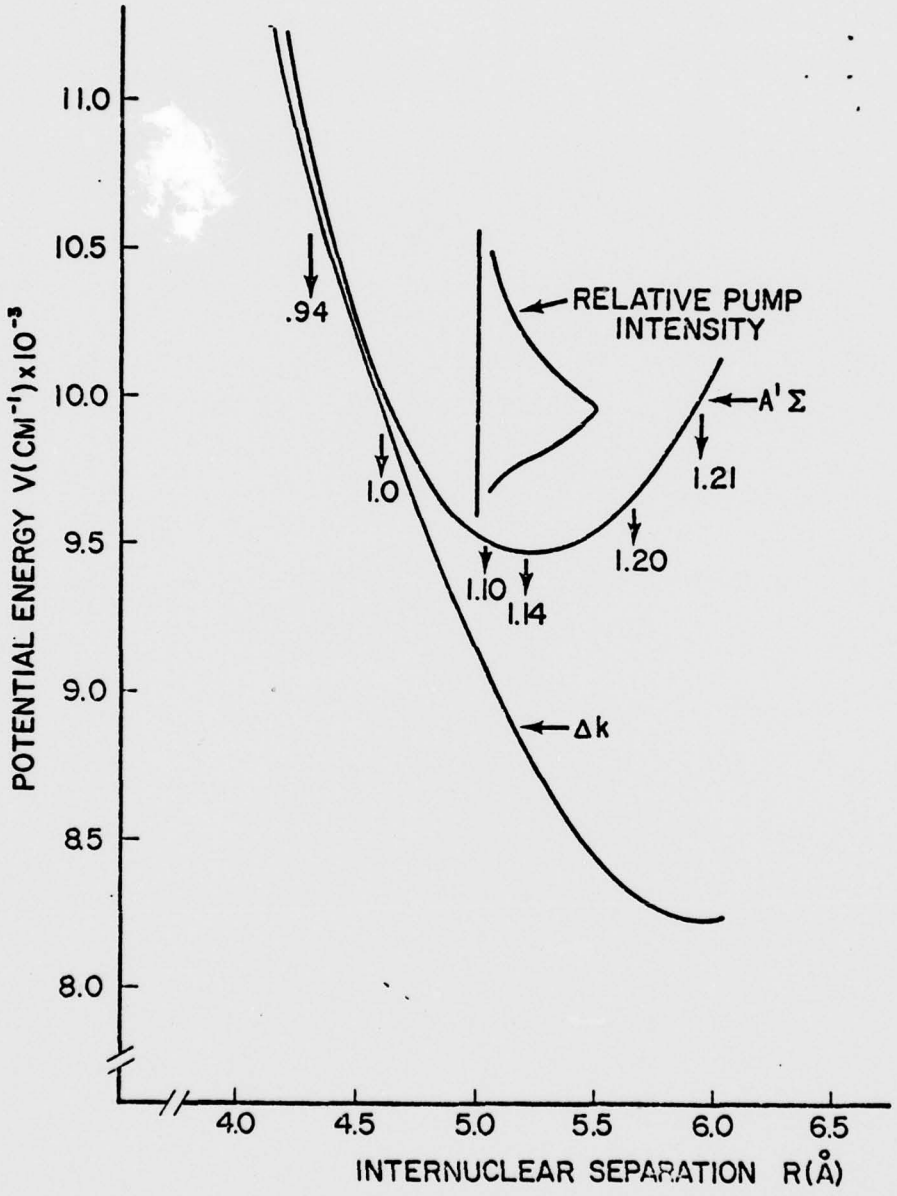

Fig 24 Cs_2 $A^1\Sigma$ Potential Curve Showing Location of Pumping Intensity for Dimer Filter

the filter and maximum absorption of Cs_2. The peak spectral intensity, as seen in Fig. 23 for [Xe] = 0, however, is near 1.14 microns, the bottom of the $A^1\Sigma$ well. So there must be time for a few collisions to occur, but not nearly enough for equilibration. Nor are there sufficient numbers of collisions to transfer many molecules from the $A^1\Sigma$ state to the $a^3\pi$ as evidenced by the fact that no $a^3\pi$ fluorescence is observable. The appearance of both the 1.14 and 1.21 peaks when pumping the dimer directly confirms the earlier statement that both of these peaks belong to the $A^1\Sigma$ state and do not represent separate transitions as suggested by others (Refs 4, 33, 59). These spectra also lead to the conclusion that the parts of the equilibrium spectra that are not observable at zero Xe density are probably associated with the $a^3\pi$. Figure 25 helps to emphasize these areas. Here the relative spectral intensity at 346°C for four different Xe densities obtained when using the Dimer pump filter are plotted.

For the zero Xe density curve A, the 1.20 micron peak is not visible nor is any fluorescence in the region $\lambda > 1.22$ microns. And the fluorescence in the gap is always very weak. To be sure that these phenomena were not just a function of the initial vibrational level to which the molecule was pumped, an experiment was performed wherein the molecule was pumped every 100 Å from 0.93 to 1.14 microns using 100 Å bandwidth filters. This covers the radial range from 4.3 to 5.2 angstroms and vibrational levels probably up to $v \sim 40$ in the $A^1\Sigma$. See Fig. 24 for the $A^1\Sigma$ potential curve and wavelengths. A picture of three of the spectra taken with the 100 Å bandpass pump filters is shown in Fig. 26. These are recorded, not reduced data; however, the spectral response and absorption corrections are not essential to this discussion.

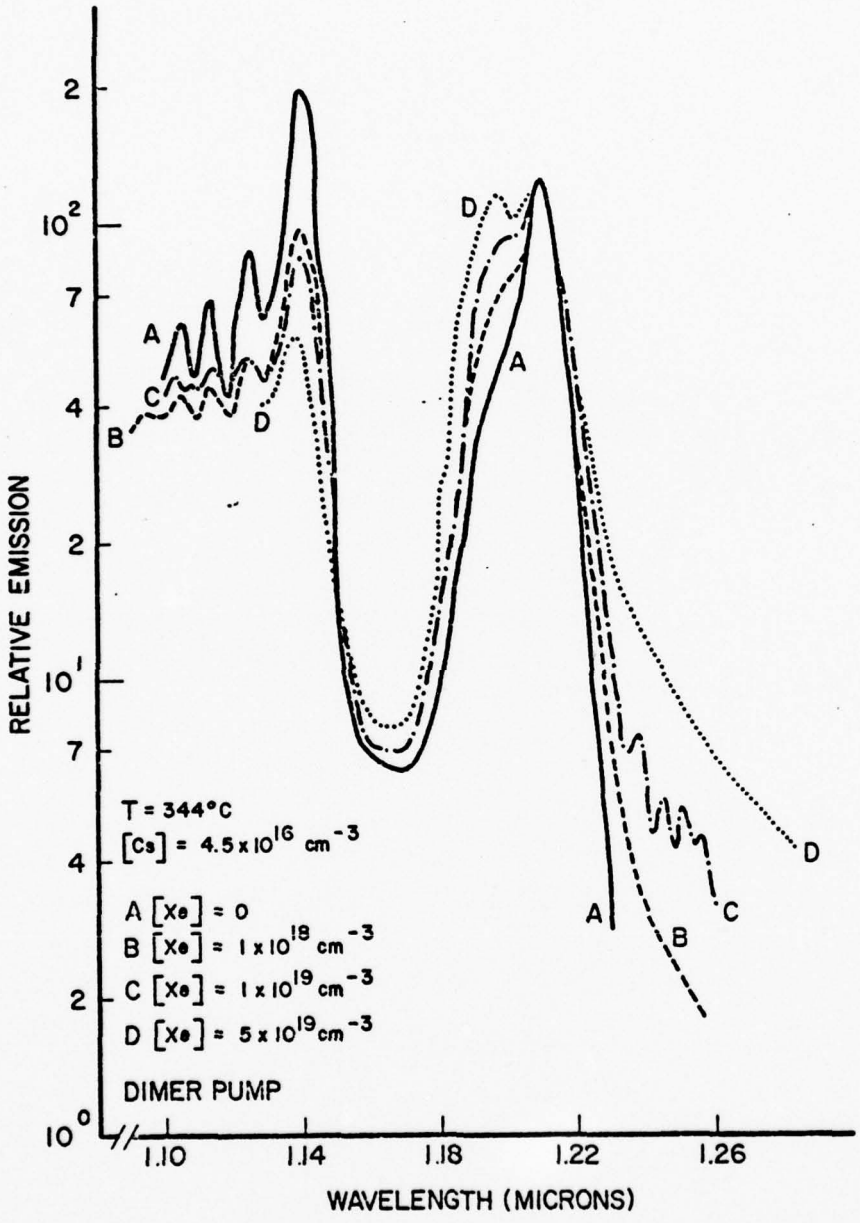

Fig 25 Cs_2 Fluorescence for $\lambda > 1.10$ microns, Xenon Density Variation

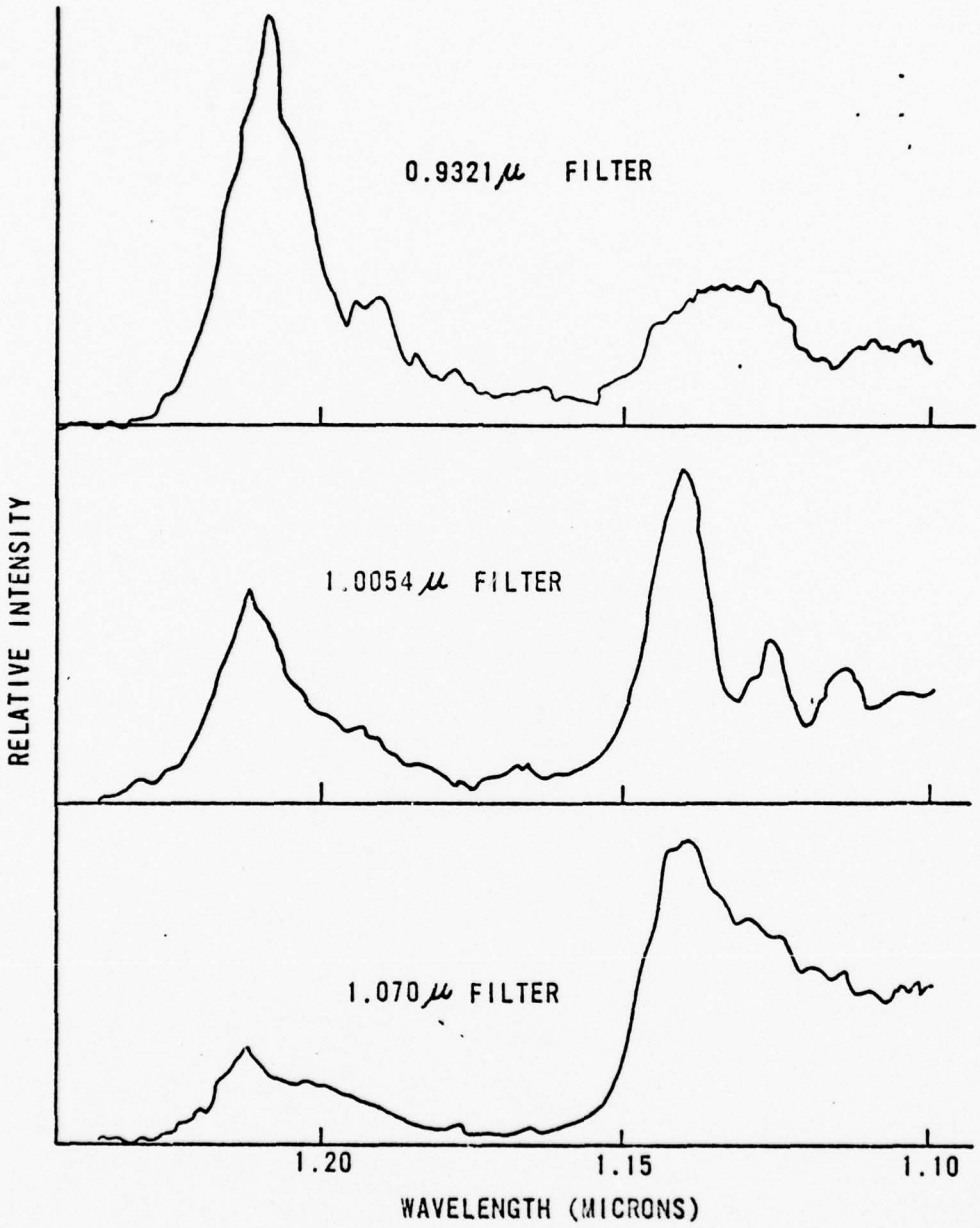

Fig 26 Cs_2 Fluorescence Spectra for [Xe] = 0, using 100 Angstrom Bandpass Pump Filters, Unreduced Data

None of these spectra showed a peak at 1.20 microns nor any observable fluorescence beyond 1.22 microns. Also the fluorescence in the gap, 1.15 - 1.18 micons, was always minimal. The spectra did show the progression expected in terms of the relative sizes of the 1.14 and 1.21 micron peaks. The spectra obtained when pumping the shortest wavelength, such as 0.94 microns (also the shortest radii and the highest in the $A^1\Sigma$ potential), fluoresced most strongly near the 1.21 micron satellite as is seen in the uppermost spectrum in Fig. 26. The intensity peaks there because the turning point for that wavelength is much higher in the $A^1\Sigma$ well than that for 1.14 microns. As the pumping moved down the A-state well, the 1.14 micron peak increased relative to the satellite, just as expected from the potentials. This can be seen from the progression of spectra in Fig. 26. One concludes, then, that the 1.20 micron peak and the fluorescence beyond 1.22 microns are associated with the $a^3\pi$ state. As the Xe density is increased, the fluorescence from these regions becomes more intense at the apparent expense of the 1.14 micron peak, which is close to the crossing of the $A^1\Sigma$ and the $a^3\pi$ potential curves. This transfer is seen very clearly in the spectral progression for increasing Xe density shown in Fig. 25. A detailed discussion of this behavior is contained in the next section.

Cs_2 Gain and Kinetics

The stimulated emission coefficient in Cs_2 has been calculated for the experimental geometry used in the fluorescence experiment. A comparison between the absorption and stimulated emission coefficients is shown in Fig. 27 for a temperature of 346°C, [Cs] = 4.4×10^{16} cm^{-3}, and [Xe] = 5×10^{19} cm^{-3}. The normalized emission intensity for the above

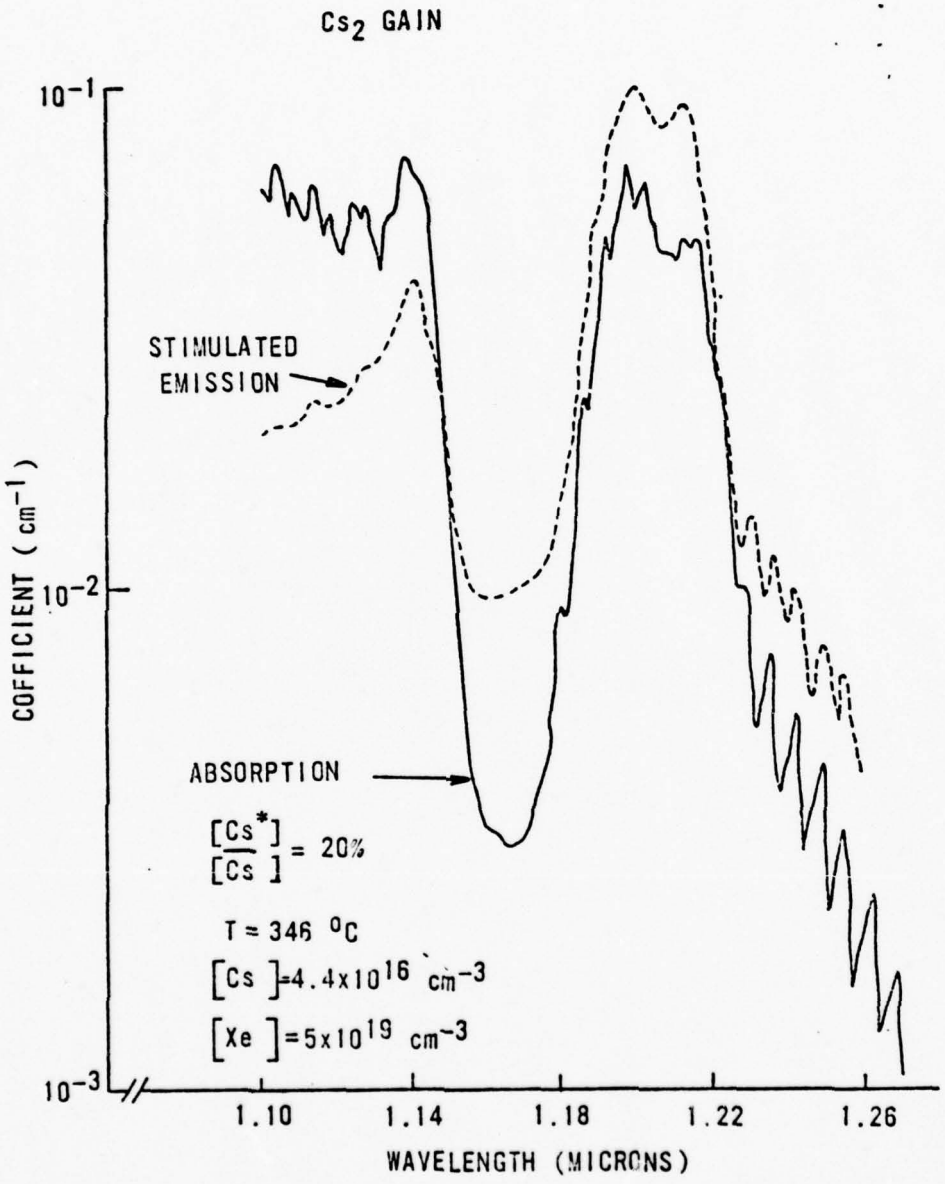

Fig 27 Cs_2 Stimulated Emission and Absorption Coefficients

experimental conditions was used in Eq. 22 along with an assumed atomic inversion of 20%. The net gain at 1.215 microns is about 0.04 cm^{-1}. The minimum atomic inversion criterion for net gain [$g_s(\nu) = \alpha(\nu)$] under these conditions is about 11%. If one calculates the stimulated emission coefficient for all of the emission data at 1.215 microns, one finds that this criterion varies only from about 9% to 15%. This result is about a factor of forty higher than was previously calculated from Eq. 23. That equation assumed equilibrium between the excited atomic and molecular populations. Therefore, there must be some losses in the system or the Xe density was not high enough to achieve equilibrium. To attempt to operate a Cs/Xe discharge at 15-20% fractional inversion would probably be very difficult and inefficient. According to the Boltzmann analysis, the discharge efficiency would drop below 50% under these conditions. Therefore, the first part of the evaluation of Cs_2 seems to imply that the molecule may have some significant loss mechanisms. The remainder of this section will by devoted to estimating the rates for these processes.

The two primary means of determining the processes that are occurring in the molecule are the Xe density dependence of the experimentally determined ratio of $[Cs_2^*]/[Cs^*]$ and of the spectral changes. In Table VI, the experimental ratios are given for several Xe densities. The experimental ratios were determined by integrating the normalized Cs_2 spectra according to Eq. 29. Also shown in Table VI are the ratios calculated from the potential curves using Eqs. 26 and 27 which assume chemical equilibrium between the excited atoms and molecules. The latter are given in the column labeled $K_{eq}[Cs]$. The dimer spectra were integrated from 1.0 to 1.22 microns which includes only the $A^1\Sigma$ state. The dimer fluores-

Table VI

Experimental and Theoretical $[Cs_2^*]/[Cs^*]$ Ratios

$[Xe](cm^{-3})$	$[Cs](cm^{-3})$	T(°C)	$[Cs_2^*]/[Cs^*]$	$K_{eq}[Cs]$	D2/D1
$2.5x10^{18}$	$4.7x10^{16}$	341	0.008	0.30	-
$5.5x10^{18}$	$4.8x10^{16}$	344	0.0095	0.31	2.2
$1x10^{19}$	$5.2x10^{16}$	348	0.013	0.34	2.0
$1x10^{19}$	$4.6x10^{16}$	338	0.013	0.29	~2
$1x10^{19}$	$4.1x10^{16}$	335	0.0125	0.30	~2
$1x10^{19}$	$3.3x10^{16}$	326	0.0105	0.32	~2
$1x10^{19}$	$1.9x10^{16}$	308	0.008	0.26	2.4
$1x10^{19}$	$1.4x10^{16}$	291	0.006	0.35	3.0
$1x10^{19}$	$1.1x10^{16}$	285	0.0045	0.31	-
$5x10^{19}$	$4.4x10^{16}$	344	0.0105	0.29	1.0
$5x10^{19}$	$3.1x10^{16}$	331	0.0085	0.28	1.0
$5x10^{19}$	$1.8x10^{16}$	306	0.0065	0.26	1.1

cence below 1.0 microns was not included because it could not be reliably separated from the CsXe and it would have contributed very little to the integral. In all cases, the experimental values of $[Cs_2^*]/[Cs^*]$ were lower than those predicted in equilibrium by roughly a factor of 30 - 40. This is not surprising considering the previously shown gain calculation.

Equation 25, which is rewritten here for convenience, must now be examined.

$$\frac{[Cs_2^*]}{[Cs^*]} = \frac{k_f[Xe][Cs]}{\Gamma_2 + k_p + [Xe](k_q + k_d)} \qquad (25)$$

Implicit in using this equation is the assumption that steady-state conditions exist. Considering the chopping speed was 70 Hz and the processes have time constants of less than 10 μsec, this assumption appears to be reasonable. The density dependence of $[Cs_2^*]/[Cs^*]$ ratio will be analyzed to determine which processes are important. For example, assume that quenching and predissociation are negligible, i.e. $k_p << \Gamma_2$ and $k_q << k_d$. Then, the size and density dependence of the ratio will depend on the relative magnitude of Γ_2 and $k_d[Xe]$. If the radiative rate is larger than the dissociative rate, the value of $[Cs_2^*]/[Cs^*]$ is equal to $k_f[Cs][Xe]/\Gamma_2$ and should be strongly dependent on [Xe]. However, as can be seen, this is not what happened. The ratio varies by less than a factor of two at 346°C over a Xe density range of 2.5×10^{18} to 5×10^{19} cm^{-3}. This implies that there is a large Xe density dependent term in the denominator of Eq. 25 so that $\Gamma_2 + k_p << [Xe](k_q + k_d)$, at least at high Xe densities. If $k_q << k_d$, then one would have, by definition, the equilibrium ratio for $[Cs_2^*]/[Cs^*]$. However, the experimental ratios are much less than that as shown in Table VI. Therefore, there must be a

quenching process such as k_q occurring in the molecule. Based on this discussion, it was assumed that $k_d << k_q$, and $k_p << \Gamma_2$. Next, both sides of Eq. 25 were divided by [Cs] and the equation inverted giving

$$\frac{[Cs][Cs^*]}{[Cs_2^*]} = \frac{k_q}{k_f} + \frac{\Gamma_2}{k_f}\frac{1}{[Xe]} \qquad (36)$$

According to Eq. 36, the rate constants, k_f and k_q, can be calculated by first plotting the experimental values of $[Cs^*][Cs]/[Cs_2^*]$ vs $1/[Xe]$, and then finding the slope and intercept.

This has been done and is drawn as the solid line in Fig. 28. The error bars around each point represent the uncertainties in both the Xe density and the normalization as described in Chapter III. Using that line, with $\Gamma_2 = 4\times10^7$/sec (Ref 40), one arrives at values for k_f and k_q of 6.5×10^{-30} cm^6/sec and 2.4×10^{-11} cm^3/sec respectively. These appear to be reasonable values. However, the experimental conditions were not exactly the same for each of the cells. The primary differences were the radiation trapping of the atomic lines and the ratio of D2 to D1 atoms. The trapping of the atomic line does not enter into the ratio of $[Cs_2^*]/[Cs^*]$, as can be seen in Eq. 25. It does have an effect on the ratio of D2 to D1 atoms, as do all the molecular formation/dissociation processes, but that effect is accounted for in the experimental D2/D1 determination.

The principle variable that could affect the results was the D2/D1 ratio. All of the dimer fluorescence was normalized to the fluorescence of a single D1 atom. However, in each experiment there were D2 atoms contributing to molecular formation also. This effect can be seen in Fig. 22, for [Xe] = 10^{19} cm^{-3} where the D1 filter produced a lower in-

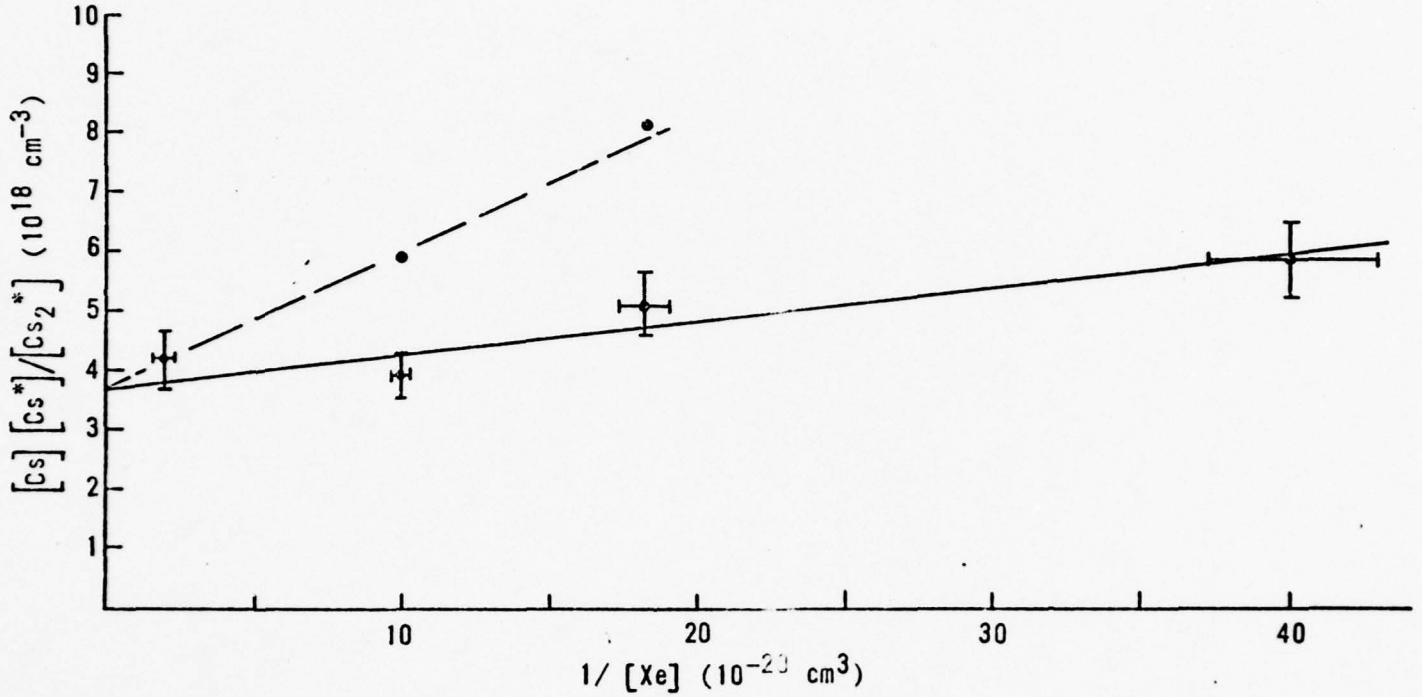

Fig 28 Variation of [Cs][Cs*]/[Cs_2*] with 1/[Xe] for $A^1\Sigma$ State

tensity spectrum than did the atomic filter. The latter filter pumped both D2 and D1 atoms and gave a higher D2/D1 (2 vs 1.5) ratio. In Fig. 20 at a Xe density of $5x10^{19}$ cm^{-3}, the spectra did not show as large a difference, although the normalized intensity for the D1 pumped spectra was still slightly less, and the D2/D1 ratio was 1.0 for each. The exact cause of the intensity difference is not clear. It could be formation into the $B^1\pi$ from the $6^2P_{3/2}$ and transfer to the $A^1\Sigma$ or it could be that the parent state of the $a^3\pi$ is the $6^2P_{3/2}$ atomic level. A higher number of D2 atoms per D1 atom would then increase the number of $a^3\pi$ molecules and possibly transfer to the $A^1\Sigma$ state. The nature of this will be discussed later.

In order to try and compensate for the different D2/D1 ratios, it was decided to "normalize" each spectrum to the same D2/D1 ratio. The word "normalize" will be put in quotes to distinguish it from the normalization of the Cs_2 spectral intensity to the atomic line intensity. Since the spectrum for [Xe] = $5x10^{19}$ cm^{-3} appeared to be closest to vibrational equilibrium, the D2/D1 ratio for that case was used as the standard. For example, the 10^{19} cm^{-3} cell had a ratio of 2/1, so assuming the atoms contribute the same amount to the spectral intensity, the $[Cs_2^*]/[Cs^*]$ ratio for that cell was divided by 1.5. Similarly the data for $5.5x10^{18}$ Xe/cm^3 was divided by 1.6 since D2/D1 = 2.2. The CsXe fluorescence data for the low density cell ($2.5x10^{18}$ cm^{-3}) was too weak to determine the D2/D1 ratio to better than 50% (i.e. 2.5 $\pm$ 25%). After "normalizing" the $[Cs_2^*]/[Cs^*]$ data for the D2/D1 ratio, one gets the dotted line shown in Fig. 28, shown without error bars. The values of k_f and k_q from that line are $1.8x10^{-30}$ cm^6/sec and $6.5x10^{-12}$ cm^3/sec respectively. These are down by a factor of approximately four from the

previous values calculated directly from the data.

To this point the formation and quenching rate constants have been calculated using both the data with different D2/D1 ratios and the data after "normalization" to a D2/D1 ratio of one. It is not possible to decide from the data taken in this project whether one of these approaches is better than the other. Therefore, the difference in the rate constants probably represents an uncertainty in the actual values. Taking average values gives $k_f = 4.2 \times 10^{-30}$ cm^6/sec and $k_q = 1.5 \times 10^{-11}$ cm^3/sec each with an uncertainty of about $\pm$ 50%. The average value of k_f agrees fortuitously well with the preliminary estimate of $4 - 5 \times 10^{-30}$ cm^6/sec. These average values will be used for the kinetic rate constants. The attendant value for k_d is 8.2×10^{-13} cm^3/sec from K_{eq}.

The rate equation (Eq. 24) that was used here had been simplified. One of the simplifications was that the $a^3\pi$ and the $A^1\Sigma$ states were closely coupled. From the behavior of the fluorescence beyond 1.22 microns (comparing spectra in Fig. 17, the two curves in Fig. 18 and all curves in Fig. 25), it appears that the states are not as closely coupled as initially expected. The fluorescence beyond 1.22 microns increased more rapidly with Xe density than did any other region beyond 1.0 microns. Assuming the parent state is the $6^2P_{1/2}$, since that is the normalization state, $[Cs_2^*(a^3\pi)]/[Cs^*]$ can be calculated for $\lambda > 1.22$ microns as a function of Xe density. There are two uncertainties in this determination. First, how much of the fluorescence should be attributed to the $a^3\pi$, and second, the lifetime of this state. Both of these are needed to calculate $[Cs_2^*(a^3\pi)]/[Cs^*]$ from Eq. 29.

The lifetime of the $a^3\pi$ state can be estimated by using the CFCP (Eq. 21) to fit the absorption for $\lambda > 1.22$ microns. The agreement be-

tween the CFCP and the experimental data is not as good as it was for the $A^1\Sigma$ spectrum, but the magnitudes can be approximated using $\tau(a^3\pi) \simeq 4\times10^{-7}$ sec. This scales to $A^a_m(\nu_o) \simeq 8\times10^6$/sec for use in Eq. 29. The superscript "a" refers to the $a^3\pi$ state. With regard to the extent of the $a^3\pi$ emission, the maximum wavelength is known, about 1.30 microns, but not the minimum. In absorption, no blue-shaded peaks were observed below 1.20 microns (see Figs. 12 and 14) and most were above 1.22 microns. In emission, the shading was not discernable and, it will be assumed that all the $a^3\pi$ emission occurs for $\lambda > 1.22$ microns and that all of that emission was $a^3\pi$. The emission below 1.22 microns should mostly be $A^1\Sigma$. Using these assumptions, the molecular/atomic ratios were calculated for the $a^3\pi$ state by integrating the normalized spectral intensity above 1.22 microns in accordance with Eq. 29.

Rewriting Eq. 25 specifically for the $a^3\pi$ state, using the superscript "a" as before, one gets

$$\frac{[Cs_2^*(a^3\pi)]}{[Cs^*]} = \frac{k_f^a[Xe][Cs]}{\Gamma_2^a + k_p^a + k_q^a[Xe]} \tag{37}$$

where k_q^a refers to all Xe density dependent losses such as quenching, dissociation and net transfer (if any) to the $A^1\Sigma$ state. Equation 37 can be inverted and written as

$$\frac{[Cs][Cs^*]}{[Cs_2^*(a^3\pi)]} = \frac{k_q^a}{k_f^a} + \frac{k_p^a + \Gamma_2^a}{k_f^a}\frac{1}{[Xe]} \tag{38}$$

and plotted as was done for the $A^1\Sigma$ state. The results are given in Fig. 29 where the solid line represents the data and the dotted line is for the data "normalized" to the same D2/D1 ratio of one.

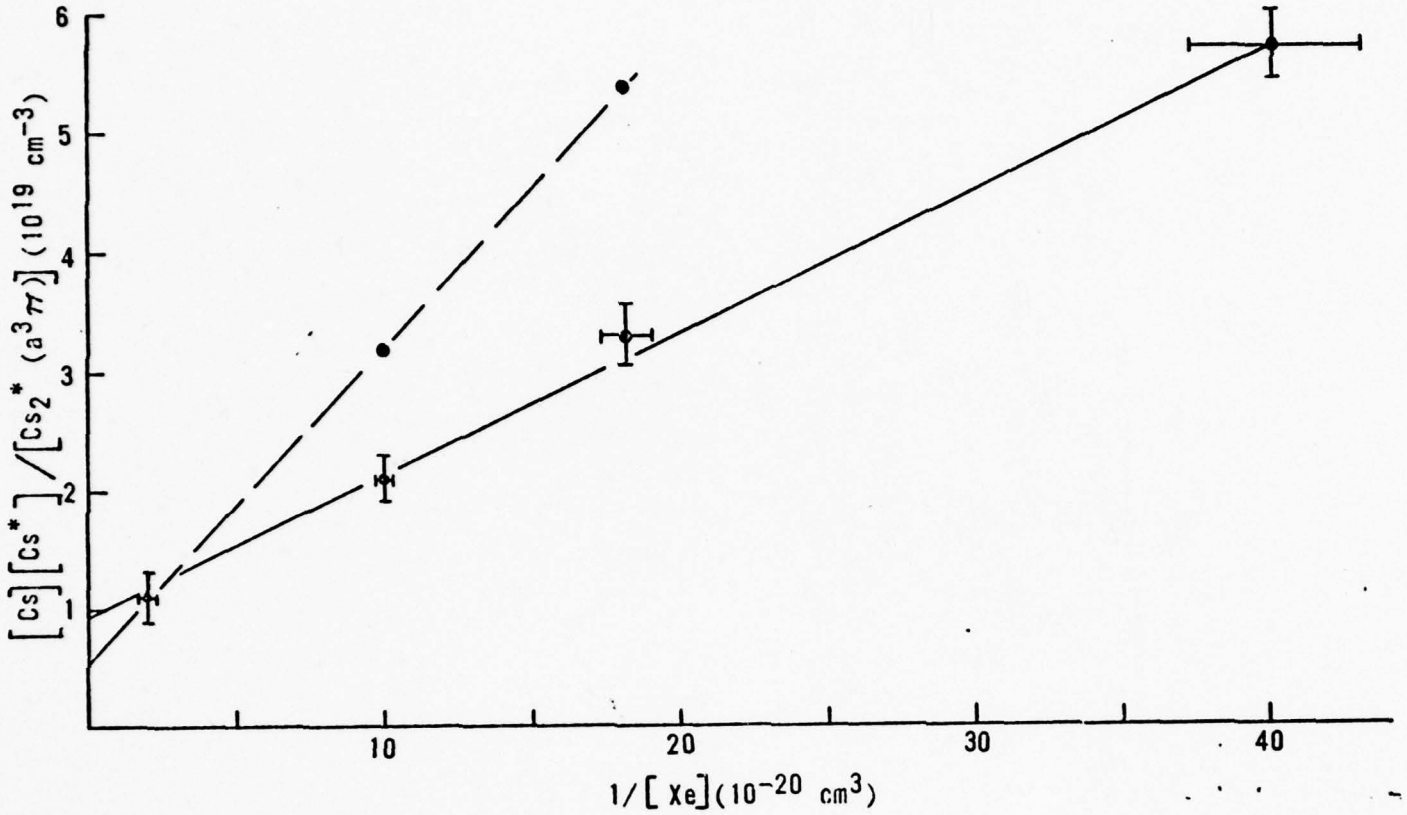

Fig 29 Variation of [Cs][Cs*]/[Cs_2*] with 1/[Xe] for $a^3\pi$ State

The slopes of the lines are given by $(\Gamma_2^a + k_p^a)/k_f^a$ and the intercepts by k_q^a/k_f^a. For the dotted line, the "normalized" plot, the slope is 2.5×10^{38} cm^6 and the intercept is 5×10^{18} cm^3. Unfortunately, there are now two equations and three unknowns, k_f^a, k_p^a and k_q^a. The formation rate constant will be assumed to be about 10^{-29} cm^6/sec based on the fact that the Cs_2 potential is very similar to the Na_2 $A^1\Sigma$. The formation rate for the latter is 10^{-29} cm^6/sec (Ref 23). This gives values of 5×10^{-11} cm^3/sec for k_q^a and $2.5\times10^9/sec$ for $\Gamma_2^a + k_p^a$. Since Γ_2^a is approximately $2.5\times10^6/sec$, k_p^a must be the dominant term and equal to $2.5\times10^9/sec$. For the solid line in Fig. 29 (the one that was not "normalized" for equal D2/D1 ratios), the slope and intercept are 1.2×10^{38} cm^6 and 10^{19} cm^3 respectively. Again assuming $k_f^a = 10^{-29}$ cm^6/sec, $k_q^a = 10^{-10}$ cm^3/sec and $k_p^a = 1.2\times10^9/sec$. Taking the averages as before, the final values for k_q^a and k_p^a are 7.5×10^{-11} cm^3/sec and $2\times10^9/sec$ with a $\pm$ 30% uncertainty.

Next, the various fluorescence spectra together with the potential curves, must be examined to explain more precisely what processes are actually occurring in Cs_2. First, the spectra taken with no Xe in the cell, as shown in Fig. 23, will be analyzed. The parts of the spectrum missing from the dimer pumped spectra have previously been established as not belonging to the $A^1\Sigma$ state. Specifically, the emission in the gap, on the 1.20 micron peak, and beyond 1.22 microns was much weaker when the $A^1\Sigma$ state was pumped directly than when the Atomic pump filter was used. On the other hand, the fluorescence in the gap and on the 1.20 micron peak was significantly increased when the Atomic filter was used. It is proposed that the fluorescence in the gap and the 1.20 micron peak are associated with the $a^3\pi$ state. At low Xe densities, when the $A^1\Sigma$ state is pumped directly, few molecules are collisionally

transferred to the $a^3\pi$ state and, so, the emission is weak. When the atomic lines are pumped, there is formation into both states and, therefore, radiation in these regions.

In the region of 5.4 Å internuclear spacing, the individual electronic states are severely perturbed by the crossing. According to perturbation theory, the energy levels are displaced from their unperturbed locations (Ref 29). This in turn causes an increase in the density of levels on each side of the crossing, i.e. the 1.14 and 1.20 micron humps. The proposed model is that the 1.14 micron peak is associated with the $A^1\Sigma$ and the 1.20 micron peak with the $a^3\pi$. When the $A^1\Sigma$ state is pumped directly at low Xe density, very little emission is observed at 1.20 microns relative to that predicted from the absorption data. Even gas gas kinetic collision rates are slower than the radiative rates so the $A^1\Sigma$ molecules radiate before many collisions can occur. This indicates that that peak does not correspond to nor does it originate from the $A^1\Sigma$ state. When the atomic states are excited, molecules are formed in both states and both peaks are seen in fluorescence. When the Xe density is increased, the spectra obtained from pumping the $A^1\Sigma$ state directly appear more like the spectra obtained by pumping the atoms. This implies that a collisional process is involved. For low Xe density and $A^1\Sigma$ pumping, there is insufficient time for transfer of $A^1\Sigma$ molecules to the $a^3\pi$ state and subsequent fluorescence in that region. The quenching or transfer rate, $R_q = k_q[Xe]$ (or $k_q[Cs]$ for $[Xe] < [Cs]$) is 4×10^6/sec, much less than the radiative rate of 4×10^7/sec. As the Xe density is increased, again for the dimer pumping, there is more collisional mixing between the $A^1\Sigma$ and $a^3\pi$ and all the energy levels become populated thus increasing the fluorescence in the regions associated with the $a^3\pi$,

as seen in Fig. 25. The decrease in the emission at 1.14 microns is probably caused by the transfer of $A^1\Sigma$ molecules at the bottom of the well to the $a^3\pi$ state. The large amplitude of that peak at low Xe density confirms the prescence of a high density of energy levels from which the molecules radiate before they can be collisionally transferred.

The variation of the fluorescence intensity in the gap 1.15 - 1.18 microns cannot be completely explained. Because the fluorescence in that region is weak (relative to that on either side) for [Xe] = 0 and dimer pumping, it cannot be associated with the $A^1\Sigma$ state directly. The intensity does not increase with Xe density either, as seen in Fig. 25. However, when the atomic states are excited, the fluorescence there decreases with increasing Xe density. A collisional loss is implied, but because the nature of the potential curves at the crossing is not known and the fluorescence quite weak (lower S/N), no detailed explanation is available. Further experiments probing this region very carefully will be required to unravel the behavior of the potentials at the crossing.

The previous explanation assumed that $k_q[Xe]$ represents another formation rate into the $a^3\pi$.Therefore, the relative magnitude of $k_q[Xe][Cs_2^*]$ versus $k_f^a[Xe][Cs][Cs^*]$ must be determined. The ratio $k_q[Cs_2^*]/k_f^a[Cs][Cs^*]$ is less than 0.25 using the average value of k_q determined earlier. If this term is included in Eq. 37, the net effect is to increase the values of k_q^a and k_p^a by about 25% or less to 9.4×10^{-11} cm^3/sec and 2.5×10^9/sec respectively. Considering the other uncertainties present in the analysis, this is not a significant change.

The final portion of the spectra to be accounted for in this model is that for $\lambda > 1.22$ microns. Since there appears to be predissociation

from the $a^3\pi$ to the $x^3\Sigma$ state, these two states must cross somewhere on the repulsive side of the $a^3\pi$ potential. If one assumes that the crossing is near the minimum of the $a^3\pi$, the fluorescence would be extremely weak or non-existent because of the rapid predissociation. Also, because the predissociation between the $a^3\pi$ and $x^3\Sigma$ states is allowed (Ref 29), a rate much higher than the measured value of 2.5×10^9/sec would be expected. Therefore, the conclusion is made that the crossing occurs much higher up in the potential, although below the dissociation limit. This means that as long as $k_p^a + k_q^a[Xe]$ is faster than the collisional mixing, there should be few molecules in the bottom of the potential where the 1.22 - 1.30 micron emission originates. Assuming gas kinetic cross section, the V - T collision rate should be about $4\times10^{-10}[Xe]$/sec. Therefore, at Xe densities greater than 6 or 7×10^{18} cm^{-3}, a significant proportion of $a^3\pi$ molecules are in the bottom of the well and their fluorescence can be observed, as it was. The formation rate must also be considered and it appears to be slower than the V - T rate. Therefore the magnitude of the fluorescence is limited by the formation rate and the $[Cs_2^*]/[Cs^*]$ ratio should behave according to Eq. 37.

In Fig. 30, a plot of $[Cs_2^*(a^3\pi)]/[Cs^*]$ vs [Xe] has been made on a log-log scale. According to Eq. 37, the plot should be linear at low Xe density and become less density dependent as [Xe] is increased. This is exactly what is seen in Fig. 30. At low Xe density the curve is almost linear and as [Xe] increases, the curve flattens out. This implies a density independent loss rate at low densities changing to a density dependent loss rate at the high densities. The observed behavior, therefore, agrees with the model of a crossing of the $a^3\pi$ and $x^3\Sigma$ states well above the minimum of the $a^3\pi$ potential and the loss of $a^3\pi$ molecules by

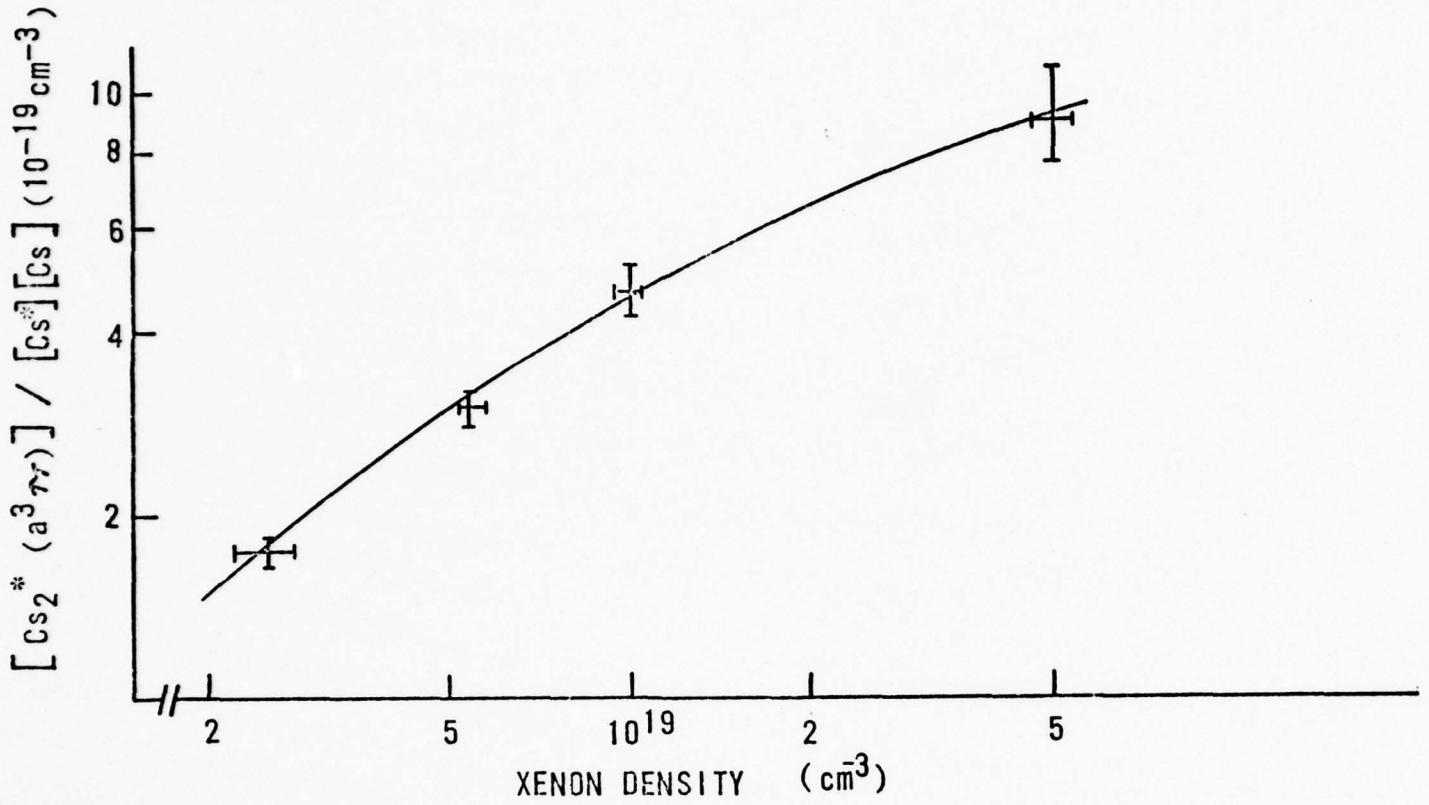

Fig 30 Xenon Density Dependence of $[Cs_2^*]/[Cs^*]$ for $a^3\pi$ State

quenching and predissociation.

There is one more aspect of the fluorescence spectra that deserves comment. That is the possibility that the parent atomic state for the $a^3\pi$ is the $6^2P_{3/2}$ rather than the $6^2P_{1/2}$ that has been assumed all along. Evidence to support this conclusion comes from the spectral differences observed between the D1 and Atomic filter pumping. Specifically, the fluorescence in the gap, the 1.20 peak, and the region beyond 1.22 microns have been associated with the $a^3\pi$ state. For all cells with a Xe density less than or equal to 10^{19} cm^{-3}, the fluorescence in these regions is stronger for the atomic filter than the D1 filter. See Figs. 22 and 23. For the highest density cell, there were essentially no differences in spectral intensity or D2/D1 ratio. Furthermore, for most of the spectra which could be normalized, the D2/D1 ratio was higher for the atomic filter than for the D1 filter. This implies that the D2 ($6^2P_{3/2}$) is the parent atomic state for the $a^3\pi$. There is no way to "prove" this theoretically because both 6P states can form an $a^3\pi$ (Ref 45). The impact of this assumption on the principle conclusions is not serious. All of the theoretical values of I/I_o or $[Cs_2^*(a^3\pi)]/[Cs^*]$ become larger with this assumption because of the factor of $k_o - k$ in the exponent (see Eq. 35). The experimental values of I/I_o do not change and those for $[Cs_2^*(a^3\pi)]/[Cs^*]$ increase by 1.2 [= $(8944/8521)^4$ in Eq. 29]. The plots of the kinetics change only in the intercept, not in slope, and then only by 20%. The net result of assuming that the $6^2P_{3/2}$ state is the origin of the $a^3\pi$ is to cause the theoretical and experimental values to differ by an even greater amount.

A model of the behavior of Cs_2 in the fluorescence experiments has now been developed. The atoms are formed into both the $a^3\pi$ and $A^1\Sigma$ states

with rate constants k_f^a and k_f respectively. There is a net loss of $A^1\Sigma$ molecules through the bottom of the well to the $a^3\pi$ state. The rate constant for this net loss is k_q. These $a^3\pi$ molecules then predissociate or are quenched to the $x^3\Sigma$ state with rate constants k_p^a and k_q^a. All of the rate constants are summarized in Table VII. They are based on the average of the rate constants calculated from spectra that have been "normalized" to allow for the various D2/D1 ratios actually observed and rate constants determined without that "normalization". The result of all these losses is that less than 1% of the excited Cs atoms are formed into Cs_2^* molecules that can radiate. The theoretical estimates for this percentage were greater than 20% depending on the temperature and Cs number density. Therefore, the overall efficiency is quite low because less than one molecule in twenty is available for radiation. The remainder serve only to heat the gas. These losses show that Cs_2 does not appear to have the potential to be a highly efficient laser, at least not under the conditions explored in this project.

Table VII

Kinetic Rate Constants in $Cs/Cs_2/Xe$

Rate Constant	$A^1\Sigma$	$a^3\pi$	Rate
$\Gamma_2(sec^{-1})$	$4x10^7$	$2.5x10^6$	
$k_f(cm^6/sec)$	$4.2x10^{-30}$	$1x10^{-29}$	$k_f[Cs][Xe]$
$k_d(cm^3/sec)$	$8.2x10^{-13}$	$2x10^{-14}$	$k_d[Xe]$
$k_q(cm^3/sec)$	$1.6x10^{-11}$	$9.4x10^{-11}$	$k_q[Xe]$
$k_p(sec^{-1})$		$2.5x10^9$	k_p

Chapter V. Summary and Conclusions

The absorption spectra of Cs_2 has been measured from 0.8 to 1.3 microns over a wide temperature range. The region from 0.9 to 1.22 microns consists mostly of red-shaded bands which are identified with the $X^1\Sigma_g^+ - A^1\Sigma_u^+$ transition. This portion of the spectrum has been analyzed according to the Classical Franck-Condon Principle. Using the $X^1\Sigma$ ground state, determined from vibrational constants by the RKR method, and the CFCP analysis, a potential energy curve was determined for the $A^1\Sigma$ state with R_e = 5.25 Å and ω_e = 34 cm^{-1}. The potential curve for the $B^1\pi$ state was also computed from the vibrational constants of Kusch and Hessel (Ref 37).

Also observed in the absorption spectrum were some blue-shaded bands, mostly for $\lambda > 1.22$ microns. These are attributed to the $X^1\Sigma - a^3\pi$ transition for several reasons: (1) The fact that the bands are blue-shaded indicates that the equilibrium internuclear separation of the upper state is less than the lower state. Thus, the two sets of bands must arise from different upper states. (2) The CFCP analysis would not reproduce the entire spectrum using only one upper state. (3) The minimum energy separation of the X and A states, according to the CFCP analysis, was greater than the energy of the peaks beyond 1.22 microns. (4) The $a^3\pi_u$ state has been postulated for many years as the state near to the $A^1\Sigma_u^+$ in all the alkalis.

The third significant feature of the spectrum is the gap or region of very low absorption, from 1.15 to 1.18 microns. This is attributed to the perturbation of the energy levels caused by the crossing of the $a^3\pi$ and $A^1\Sigma$ states. This crossing occurs about 50 cm^{-1} from the bottom

of the $A^1\Sigma$ potential curve. This crossing point was used together with an $\omega_e = 50\ cm^{-1}$ and a $D_e = 6750\ cm^{-1}$ to construct an approximate potential curve for the $a^3\pi$ state. The resulting equilibrium internuclear radius is about 4.3 Å.

The fluorescence spectrum of Cs_2 was measured as a function of temperature and Xe density using various interference filters to selectively pump atoms or molecules. For the most part, the spectral shape appeared just about as expected. The molecules in the upper state appeared to be in vibrational equilibrium at the highest Xe density of $5x10^{19}\ cm^{-3}$. However, the excited molecular and atomic populations were not in chemical equilibrium. This was seen by the temperature dependence of the emission and the fact that very little atomic fluorescence was observed when the molecular states were pumped directly. The fluorescence spectra were normalized to the atomic emission intensity by means of the CsXe wing. In this way, the dimer intensity per excited D1 atom could be determined. Using this normalized intensity, the stimulated emission coefficient was calculated. The minimum atomic inversion criterion for gain in the Cs_2 vapor was about 13% at 346°C with a Cs density of $4.5x10^{16}\ cm^{-3}$. This result compares with a value of 0.3% predicted from the absorption, assuming equilibrium between the excited atoms and molecules. Such a large discrepancy implies that there are major loss mechanisms in the Cs_2 molecule.

The Xe density dependence of the Cs_2 fluorescence was investigated to determine molecular formation and loss rates in Cs_2^*. Separate rates were established for both the $A^1\Sigma$ and $a^3\pi$ states. There are uncertainties in these values because the experimental conditions were not exactly alike for each cell. The ratio of the number of D2 atoms per

D1 atom was different. Each spectrum was "normalized" to a D2/D1 ratio of one, that for the high Xe density cell. Using these adjusted values, the rate constants were determined by averaging the rates calculated from the "normalized" data and the "unnormalized" data. This averaging gives an uncertainty of $\pm$ 50%. The value of the formation rate constant for the $A^1\Sigma$ state was 4.2×10^{-30} cm^6/sec, assuming an average radiative lifetime of 2.5×10^{-8} sec. The principal loss from this state was collisional transfer to the $a^3\pi$ state with a rate constant of 1.6×10^{-11} cm^3/sec. This represents the net transfer of molecules. For the $a^3\pi$ state, only ratios of the rate constants could be determined from the data. Assuming a formation rate of 10^{-29} cm^6/sec, the corresponding quenching and predissociation rate constants were 9.4×10^{-11} cm^3/sec and $2.5 \times 10^9/sec$. The formation rate assumed appears reasonable because the $a^3\pi$ potential is deeper and about the same volume as the $A^1\Sigma$ so k_f for the $a^3\pi$ state should be larger. The $a^3\pi$ potential is not quite as deep as that of Na_2^* $(A^1\Sigma)$, but has slightly more volume. Therefore, the two rate constants should be approximately the same. That of Na_2^* has been determined as 10^{-29} cm^6/sec (Ref 23), so the same value appears a logical choice for Cs_2^* $(a^3\pi)$. In any case, the resultant loss rates are still large and dominate the molecular performance.

The crossing of the $a^3\pi$ and $x^3\Sigma$ states appears to be below the dissociation limit of the $a^3\pi$ but probably higher than the crossing of the $a^3\pi$ and $A^1\Sigma$ states. For Na_2 this crossing is predicted to be above the dissociation limit (Ref 2). The reason for the difference appears to be mostly that in Cs_2 the $a^3\pi$ potential is shifted to shorter radii relative to the other states than in Na_2. One of the results of that shift is that the $a^3\pi$ - $X^1\Sigma$ transition occurs at wavelengths that are

longer than the $A^1\Sigma$ - $X^1\Sigma$ transition. This does not happen for the other alkalis, i.e. no $a^3\pi$ - $X^1\Sigma$ radiation has been observed (absorption or fluorescence). The overall trend in the alkalis seems to be that the heavier the alkali, the further down in the $a^3\pi$ potential the $a^3\pi$ - $x^3\Sigma$ crossing occurs. The result is that the quenching and predissociation losses are greater for the heavier alkalis such as Rb and Cs. For instance in Cs_2, less than one in every twenty $A^1\Sigma$ molecules that are formed actually radiate. The rest serve only to heat the gas.

One way to indicate the potential of Cs_2 as a laser candidate is to look at the intensity (I_p) necessary to make the stimulated emission rate equal to the predissociation rate, 2.5×10^9/sec. The observed stimulated emission cross section, σ_s, is about 10^{-17} cm^2 as determined by dividing $g_s(\nu)$ by $[Cs^*]$ in Eq. 22. The stimulated emission rate is $R_{se} = I_p\sigma_s/h\nu$. The intensity required is 4×10^7 watts/cm^2. Just to overcome the quenching losses out of the $A^1\Sigma$ requires an I_p of 1.3×10^7 watts/cm^2 for $[Xe] = 5\times10^{19}$ cm^{-3}. These are likely to be difficult to achieve. It appears, then, that based on this reasearch, Cs_2 is not an attractive candidate as a high efficiency laser medium, at least not under the conditions studied here.

Chapter VI. Recommendations

The primary recommendation for further research in Cs_2 is in the area of more extensive investigation of the loss rates that have been identified here. There are pulsed dye lasers available now that operate in the 0.85 - 1.0 micron region for pumping both the atoms and the molecules directly. New intrinsic Ge detectors are coming onto the market with MHz bandwidths so the time dependence of the kinetics can be explored. Use of these tools should permit a better determination of the rate constants and the location of the crossing of the $a^3\pi$ and $x^3\Sigma$ potentials. Finally, the temperature dependence of the rate constants should be examined to establish whether other operating conditions might be more favorable to lasing of Cs_2 than those used in this research.

Bibliography

1. Abramowitz, M. and I.A. Stegun, Ed. Handbook of Mathematical Functions. New York: Dover Publications Inc, (1965).

2. Bardsley, J.N., B.R. Junker and D. W. Norcross. "Pseudo-potential Calculations for Na_2^+, Na_2 and Na_2*." Chemical Physics Letters, 37: 502, (1976).

3. Baumgartner, G., W. Demtroder and M. Stock. "Lifetime- Measurements of Alkali-Molecules Excited by Different Laserlines." Zeitschrift fur Physik, 232:462, (1970).

4 Bayley, D.S., E.C. Eberline and J.H. Simpson. "Absorption Spectrum of Diatomic Cesium Molecules." Journal of Chemical Physics, 49: 2863, (1968).

5. Benedict, R.P., D.L. Drummond and L.A. Schlie. "Absorption Spectra of the Cs_2 Molecule." Journal of Chemical Physics, : , (1977).

6. Callender, R.H., J.I. Gersten, R.W. Leigh and J.L. Yang. "Laser Induced Fluorescence from Na_2." Physical Review A, 14:1672, (1976).

7. Carrington, C.G., D. Drummond, A. Gallagher and A.V. Phelps. "Oscillations in Continuum Molecular Spectra of Alkali-Metal--Noble-Gas Molecules." Chemical Physics Letters, 22:511, (1973).

8. Carrington, C.G. and A. Gallagher. "Teratomic Recombination of Excited RbXe*." Journal of Chemical Physics, 60:3436, (1974).

9. Chen, D.L., and A.V. Phelps. "Absorption Coefficients for the Wings of the First Two Resonance Doublets of Cesium Broadened by Argon." Physical Review A, 7:470, (1973).

10. Chen, S. and M. Takeo. "Broadening and Shift of Spectral Lines Due to Prescence of Foreign Gases," Reviews of Modern Physics, 29:20, (1957).

11. Dalgarno, A. and A.E. Kingston. "The Refractive Indices and Verdet Constants of the Inert Gases." Proceedings of the Royal Society, 259:424, (1960).

12. Dalgarno, A. and M.R.H. Rudge. "Spin-Exchange Cross Sections for Collisions Between Alkali Atoms." Proceedings of the Royal Society, A286:519, (1965).

13. Devyatov, A.M., T.N. Solov'ev and L.M. Volkova. "Study of the Postive Column in the Vapors of the Alkali Metals." High Temperature, 13:245, (1975).

14. Drummond, D.L. Extreme Wing Line Broadening and Rubidium-Inert-Gas Potentials. Unpublished Dissertation. Boulder, Colorado:University of Colorado, (1973).

15. Drummond, D.L. and A. Gallagher. "Potentials and Continuum Spectra of Rb-Noble Gas Molecules." Journal of Chemical Physics, 60:3426, (1974).

16. Drummond, D.L. and L.A. Schlie. "Spectra and Kinetics of the Rb_2 Molecule." Journal of Chemical Physics, 65:2116, (1976).

17. Ducas, T.W., M.G. Littman, M.L. Zimmerman and D. Kleppner. "Radiative Lifetimes of Selected Vibrational Levels in The $A^1\Sigma_u$ State of Na_2*." Journal of Chemical Physics, 65:842, (1976).

18. Fabry, M. "Theoretical and Experimental Determinations of Cesium Oscillator Strengths." Journal of Quantitative Spectroscopy and Radiative Transfer, 16:127, (1976).

19. Feddman, K.T. and G.H. Whiting. "The Heat Pipe." Mechanical Engineering, p.30, (February 1967).

20. Felden, M.M. and M.A. Felden. "Excitation Cross Sections of Alkali-Metal Atoms Colliding With Slow Electrons." Canadian Journal of Physics, 51:1709, (1973).

21. Frost, L.S. and A.V. Phelps. "Rotational Excitation and Momentum-Transfer Cross Sections for Electrons in H_2 and N_2 from Transport Coefficients." Physical Review, 127:1621, (1962).

22. Frost, L.S. and A.V. Phelps. "Momentum-Transfer Cross Sections for Slow Electrons in He, Ar, Kr, and Xe from Transport Coefficients." Physical Review, 136:A1538, (1964).

23. Gallagher, A. Private Communication.

24. Gordon, R.J., Y.T. Lee and D.R. Herschbach. "Supersonic Molecular Beams of Alkali Dimers." Journal of Chemical Physics, 54:2393,(1971).

25. Green, T.J. and W. Williamson Jr. "Calculated Electron Excitation Cross Sections for the Alkalis." Atomic Data and Nuclear Data Tables, 14:161, (1974).

26. Hall, W.D. and J.C. Zorn. "Measurement of Alkali-Metal Polarizabilities by Deflection of a Velocity-Selected Atomic Beam." Physical Review A, 10:1141, (1974).

27. Hedges, R.E.M., D.L. Drummond, and A. Gallagher. "Extreme-Wing Line Broadening and Cs-Inert-Gas Potentials." Physical Review A, 6:1519, (1972).

28. Henesian, M.A., R.L. Herbst and R.L. Byer. "Optically Pumped Super-Fluorescent Na_2 Molecular Laser." Journal of Applied Physics, 47: 1515, (1976).

29. Herzberg, G. Molecular Spectra and Molecular Structure, I. Spectra of Diatomic Molecules. New York: Van Nostrand Rheinhold Co.,(1950).

30. Hessel, M.M., E.W. Smith, and R.E. Drullinger. "Transition Dipole Moment of Na_2 and its Variation With Internuclear Distance." Physical Review Letters, 33:1251, (1974).

31. Holstein, T. "Energy Distribution of Electrons in High Frequency Gas Discharges." Physical Review, 70:367, (1946).

32. Jablonski, A. "General Theory of Pressure Broadening of Spectral Lines." Physical Review, 68:78, (1945).

33. Kostin, N.N. and V.A. Khodovoi. "Excitation Kinetics of Molecular Vapor of Alkali Metals by Intense Optical Radiation." Izvestiya Akademii Nauk SSSR. Seriya Fizicheskaya, 15:2093, (1973).

34. Kostin, N.N., M.P. Sokolova, V.A. Khodovoi and V.V. Khromov. "Nonlinear Absorption of Ruby Laser Emission by Molecular Rubidium Vapor." Soviet Physics JETP, 35:253, (1972).

35. Krause. L. "Collisional Excitation Transfer Between the $^2P_{1/2}$ and $^2P_{3/2}$ Levels in Alkali Atoms." Apllied Optics, 5:1375, (1966).

36. Kusch, P. and M.M. Hessel. "An Analysis of the 6250 Å Band System of Cs_2." Journal of Molecular Spectroscopy, 25:205, (1968).

37. Kusch, P. and M.M. Hessel. "A Study of the 7667 Å Band System of Cs ; the Magnetic Rotation Spectra of the 7667 and 6250-A Systems." Journal of Molecular Spectroscopy, 32:181, (1969).

38. Kusch, P. and M.M. Hessel. "Perturbations in the $A^1\Sigma_u^+$ state of Na_2." Journal of Chemical Physics, 63:4087, (1975).

39. Kutzelnigg, W., V. Staemmler, and M. Gelus. "Potential Curve of the Lowest Triplet State of Li_2." Chemical Physics Letters, 13:496, (1972).

40. Link, J.K. "Measurement of the Radiative Lifetimes of the First Excited States of Na, K, Rb, and Cs by Means of the Phase-Shift Method." Journal of the Optical Society of America, 56:1195, (1966).

41. Loomis, F.W. and P. Kusch. "The Band Spectrum of Caesium." Physical Review, 46:292, (1934).

42. Margenau, H. and W. Watson. "Pressure Effects on Spectral Lines." Reviews of Modern Physics, 8:22, (1936).

43. Merzbacher, E. Quantum Mechanics. New York: John Wiley and Sons Inc., (1961).

44. Mitchell, A.C.G. and M.W. Zemansky. Resonance Radiation and Excited Atoms. Cambridge, England: Cambridge University Press, (1934).

45. Mulliken, R.S. "Correlation of Atomic J Values and Molecular Quantum Numbers, With Applications to Halogen, Alkaline Earth Hydride and Alkali Molecules." Physical Review, 36:1440, (1930).

46. Nighan, W.L. "Electron Energy Distributions and Collision Rates in Electrically Excited N_2, CO and CO_2." Physical Review, A2:1989, (1970).

47. Nighan, W.L. and A.J. Postma. "Electron Momentum-Transfer Cross Sections in Cesium." Physical Review, A6:2109, (1972).

48. Nolan, J.F. and A.V. Phelps. "Measurement of Cesium Excitation Cross Sections Near Threshold by a Swarm Technique." Physical Review, 140:A792, (1965).

49. Nolan, J.F. Electron Collision Cross Sections in Metal Vapors. NASA CR-54670. Pittsburgh, Pennsylvania: Westinghouse Research Laboratories, (1966).

50. Nygaard, K.J. "Electron-Impact Ionization Cross Sections in Cesium." Journal of Chemical Physics, 49:1995, (1968).

51. Palmer, A.J. "Small-Signal Gain Modeling for Optical Pumping on the Alkali-Xenon and Alkali Dimer Laser Transitions." Journal of Applied Physics, 47:3088, (1976).

52. Phelps, A.V. Tunable Gas Lasers Utilizing Ground State Dissociation. JILA Report 110. Boulder, Colorado:University of Colorado, (1972).

53. Rapp, D. and P. Englander-Golden. "Total Cross Sections for Ionization and Attachment in Gases by Impact. I. Positive Ionization." Journal of Chemical Physics, 43:1464, (1965).

54. Rees, A.L.G. "The Calculation of Potential-Energy Curves from Band-Spectroscopic Data." Proceedings of the Physical Society, London, 59:998, (1947).

55. Schaper, M. and H. Scheibner. "Absolute Determination of the Total Excitation Cross Sections of the Noble Gases by Electron Impact." Beit. Plasma Physics, 9:45, (1969).

56. Schlie, L.A. "Electron Velocity Distributions, Fractional Energy Transfer and Collision Rates for Potential Na_2, NaHe, and NaXe Electrically Excited Laser Discharges." Journal of Applied Physics, 47:1397, (1976).

57. Schlie, L.A. Report in preparation.

58. Seaton, M.J. "Impact Parameter Method for Electron Excitation of Optically Allowed Atomic Transitions." Proceedings of the Physical Society, London, 79:1105, (1962).

59. Sorokin, P.P. and J.R. Lankard. "Emission Spectra of Alkali-Metal Molecules Observed with a Heat-Pipe Discharge Tube." Journal of Chemical Physics, 55:3810, (1971).

60. Stone, P.M. "Cesium Oscillator Strengths." Physical Review, 127: 1151, (1962).

61. Taylor, J.B. and I. Langmuir. "Vapor Pressure of Caesium by the Positive Ion Method." Physical Review, 51:753, (1937).

62. Uman, M.A. Introduction to Plasma physics. New York:McGraw-Hill, (1964).

63. Vidal, C.R. and J. Cooper. "Heat-Pipe Oven: A New, Well Defined Metal Vapor Device for Spectroscopic Measurements." Journal of Applied Physics, 40:3370, (1969).

64. Vidal, C.R. and F.B. Haller. "Heat-Pipe Oven Applications. I. Isothermal Heater of Well Defined Temperature. II. Production of Metal Vapor-Gas Mixtures." Review of Scientific Instruments, 42: 1779, (1971).

65. Wechsler, A.E. Characteristics of a Metal Vapor. AD 631469, (January, 1966).

66. York, G. and A. Gallagher. High Power Gas Lasers Based on Alkali-Dimer A-X Band Radiation. JILA Report 114. Boulder, Colorado: University of Colorado, (1974).

67. Zapesochnyi, I.P. and L.L. Shimon. "Effective Excitation Cross Sections of Alkali-Metal Atoms Colliding with Slow Electrons." Optics and Spectroscopy, 21:155, (1966).

68. Zapesochnyi,I.P. "Absolute Cross Sections for the Excitation of the Levels of Alkali Metal Atoms by Low Energy Electrons." High Temperature, 5:6, (1967).

69. Zapesochnyi, I.P. and I.S. Aleksakhin. "Ionization of Alkali Metal Atoms by Slow Electrons." Soviet Physics JETP, 28:41, (1969).

70. Zapesochnyi, I.P. E.N. Postoi and I.S. Aleksakhin. "Excitation of Resonance Levels of Alkali Metal Atoms by Electron Impact." Soviet Physics JETP, 41:865, (1976).

Appendix A. Boltzmann Analysis

The purpose of this appendix is to describe briefly the Boltzmann analysis of the electron kinetics of the Cs/Xe system. Included in this analysis are: (1) The formulation of the Boltzmann transport equation pertinent to electrical discharges in gases that experience both elastic and inelastic processes; and, (2) A careful review of the cross sections of essential electron kinetic mechanisms in the Cs/Xe vapor system. The particular form of the Boltzmann equation used in this analysis is not unique nor original. Only the results that pertain to the Cs/Xe system are new. For more detail on the Boltzmann equation and its solution see Refs 21,22, 31, 46, and 56.

Boltzmann Transport Equation

The Boltzmann transport equation for any charged or neutral particle is given by (Ref 62)

$$\frac{\partial f}{\partial t} + \bar{v}\cdot\nabla_r f + \frac{\bar{F}}{m}\cdot\nabla_v f = \left(\frac{\delta f}{\delta t}\right)_{coll} \qquad (A1)$$

For the case of an electron gas, $f = f(\bar{r},\bar{v},t)$ is the phase-space electron velocity distribution function, $\bar{v}$ is the velocity of the electron, $\bar{r}$ is the electron position, and $\bar{F}$ is any external force acting on the electron. $(\delta f/\delta t)_{coll}$ describes the time rate of change of f due to collisions with neutral and ionized particles and other electrons. The electron has a mass m and a charge e. For the analysis presented in this appendix, several simplifying assumptions have been made: (1) The discharge is steady-state, i.e. $\partial f/\partial t = 0$; (2) The medium is homogeneous so $\nabla_r f = 0$;

and (3) The only external force acting on the electrons is that due to a longitudinal electric field, $\bar{F} = -e\bar{E}$. The final assumption is that f is nearly spherically symmetric and, therefore, can be expanded in the first two spherical harmonics, $f \simeq f_0 + f_1\cos\theta$. The angle theta is the electron scattering angle with respect to the incident particle direction, and $f_1 << f_0$. Using this assumption, one can solve for f_0, as was first done rigorously by Holstein (Ref 31). This approximation of f by the first two terms has been found to be valid when the integral of the momentum-transfer cross section is much greater than the integral of all the inelastic cross sections (Ref 31). For Cs this assumption holds fairly well for low energies (see Fig. A1). With these approximations, the Boltzmann transport equation for a homogeneous cloud of electrons drifting through a gas of neutral density N is given by (Ref 55)

$$\frac{d}{du}\left(\left[\frac{1}{3}\left(\frac{E}{N}\right)^2 u\left(\sum_s Q_s\right)^{-1} + \left(\frac{KT}{e}\right)u^2\sum_s Q_s\,\frac{2m}{M_s} + 2\Gamma_{ee}\left(\frac{N_e}{N}\right)g(u)\right]\frac{df}{du}\right.$$

$$\left. + \sum_s Q_s\,\frac{2m}{M_s}\,u^2 f(u) + 3\Gamma_{ee}\left(\frac{N_e}{N}\right)h(u)f(u)\right)$$

$$+ \sum_{sj} p_{sNj}[(u+u_{sj})Q_{sj}(u+u_{sj})f(u+u_{sj}) - uQ_{sj}(u)f(u)]$$

$$+ \sum_{sj} p_{sNj}p^s_{sj}[(u-u_{sj})Q_{-sj}(u-u_{sj})f(u-u_{sj}) - uQ_{-sj}(u)f(u)]$$

$$+ \sum_{sl} p_{sNl}[(u+u_{sl})Q_{sl}(u+u_{sl})f(u-u_{sl}) - uQ_{sl}(u)f(u)]$$

$$+ \sum_{sl} p_{sNl}\delta(u=0)\int_{u_{sl}}^{\infty} xQ_{sl}(x)dx = 0 \qquad \text{(A2)}$$

Equation A2 has been written in terms of u, the energy variable; p_{sNj}, the fractional concentration of the s^{th} neutral gas for the j^{th} inelastic process (or p_{sNl} for the l^{th} ionization process); $Q_{sj}(u)$, the cross section for the s^{th} gas and j^{th}(or l^{th}) process; and M_s, the mass of the s^{th} neutral particle. The u_{sj}, or u_{sl}, refer to the threshold energy of the j^{th}, or l^{th}, process in the s^{th} gas. Q_{-sj} is the cross section for superelastic collisions wherein the electron gains energy. The coulomb integrals g(u) and h(u) are given by (Ref 56)

$$g(u) = \int_0^u x^{3/2} f(x)dx + u^{3/2}\int_u^\infty f(x)dx \tag{A3}$$

and

$$h(u) = \int_0^u x^{1/2} f(x)dx \tag{A4}$$

Furthermore we have (Ref 56)

$$\Gamma_{ee} = \frac{e^2}{24\pi\varepsilon_o{}^2} \ln \Gamma_e \tag{A5}$$

$$\Gamma_e = 12\pi(2\varepsilon_o u_m e/3)^{3/2}/N_e{}^{1/2} \tag{A6}$$

$$Q_s(u) = [(p_{sN} - p_{sI})Q_{el,s}(u) + p_{sI}Q_{eI}(u)] \tag{A7}$$

and

$$Q_{eI}(u) = 3\,\Gamma_{ee}/2u^2 \tag{A8}$$

In these equations p_{sI} is the fractional concentration of ions, $Q_{el,s}$ the momentum-transfer cross section for the s^{th} gas and u_m, the mean electron energy given by

$$u_m = \int_0^\infty u^{3/2} f(u) du \tag{A9}$$

The normalization condition for f(u) is

$$1 = \int_0^\infty u^{1/2} f(u) du \tag{A10}$$

In Eq. A2, the first term describes the energy input to the electrons by the electric field and the second accounts for the heating of the electron gas by thermal motion. The third and fifth terms describe the electron-electron interaction. The fourth, sixth, seventh and eighth terms account for elastic, inelastic, superelastic, and ionization collision processes. The fourth term includes electron energy losses to both ions and neutrals by elastic collisions. And the ninth term is the ionization rate, multiplied by $\delta(u=0)$ to force all secondary electrons to have zero energy. An important point to note in this equation is that f(u) depends not on specific number densities, but rather on fractional densities and on E/N. This integral-differential-difference equation has been solved and coded on the AFWL CDC 6600 Computer(Ref 57).

The basic solution technique was to break the energy axis into n cells of size $\Delta u = u_{max}/(n-1)$, where u_{max} is the maximum energy for which f(u) is determined. Equation A2 was rearranged into a finite difference equation and a recursion relation found for $f(u_{j-1})$, $f(u_j)$, and $f(u_{j+1})$. An initial value of $f(u_{max})$ was chosen at a u_{max} large enough so the f is far out on the tail of the distribution. The recursion relation was then used to calculate the value of f at lower values of u. The final distribution function was normalized according to Eq. A10. As a test of the self-consistency of the result, an energy

conservation balance of Eq. A2 was made. The electron energy balance equation was obtained by multiplying Eq. A2 by $e(2e/m)^{1/2}udu$ and integrating. The result can be written in terms of the drift velocity, v_d where

$$v_d = -(2e/m)^{1/2}(1/3)(E/N)\int_o^\infty u(\frac{df}{du})\, du/\sum_s Q_s \tag{A11}$$

and the normalized rate constants (ν/N) are

$$(\nu/N)_{el,sN} = \left(\frac{2e}{m}\right)^{1/2}\int_o^\infty u^2 Q_{el}[f(u) + \frac{KT}{e}\left(\frac{df}{du}\right)]du \tag{A12}$$

$$(\nu/N)_{s,Nj} = \left(\frac{2e}{m}\right)^{1/2}\int_o^\infty uQ_{sj}(u)f(u)du \tag{A13}$$

The rate constant for ionization and superelastics can be written in an analogous manner. The final energy balance equation was then (Ref 56)

$$\begin{aligned} ev_d(E/N) = {} & e\sum\frac{2m}{M_s}[(p_{sN} - p_{sI})(\nu/N)_{el,sN} + p_{sI}(\nu/N)_{el,sI}] \\ & + e\sum_{sj} p_{sNj}u_{sj}(\nu/N)_{s,NJ} - e\sum_{sj} p_{sNj}p^s_{sj}u_{sj}(\nu/N)^s_{s,Nj} \\ & + e\sum_{sl} p_{sNl}u_{sl}(\nu/N)_{s,Nl} \end{aligned} \tag{A14}$$

The term on the left is the power input by the electric field per electron per neutral particle and the terms on the right are the power losses to the gas constituents. They are, respectively, the elastic losses, the net (inelastic minus superelastic) inelastic losses and the ionization loss. The electron-electron terms do not appear because they only redistribute the electron energy rather than act as a source or sink.

After the distribution function has been calculated, the code checks the energy balance according to Eq. A14. The code results are acceptable only if the balance is within 0.1%.

Further tests have been made on the code. The code results have been checked against analytic solutions for certain special cases and against other codes which had been verified experimentally. In all cases the agreement was excellent. Therefore, it is believed that the results of the Boltzmann analysis are valid and are limited only by the input processes and their cross sections. These are discussed in the next section.

Cesium Electron Cross Sections

In general, the electron impact cross sections for Cs appear to be fairly well known. There has been considerable effort during the past several years to determine the magnitude of the cross sections because of the use of Cs as an electron seed material in MHD plasmas. This section will summarize briefly the cross sections that were used in this thesis rather than review all the available data. The one exception will be the Cs electron excitation cross sections because of their importance in determining the electronic pumping efficiency.

Many experiments have been performed to infer the electron momentum-transfer cross sections in Cs. Most have used the swarm technique developed by Frost and Phelps (Ref 21,22). In this method, first the electron drift velocity is measured. Then a Boltzmann analysis is conducted with different momentum-transfer trial cross sections until the variation of v_d with E/N or other variables can be matched. A summary of the significant research in Cs for these cross sections is given in

Ref 46. In that reference, Nighan and Postma critically examined the available data and determined a representative momentum-transfer cross section that gave the best agreement with all the experimental data that they considered to be valid. That cross section is shown in Fig. A1. Their results have been extended to higher energies by straight line extrapolation as shown by the dotted line. However, for most of the analyses, the cross sections beyond 5 eV were unimportant. For example, see Fig. 2 in Chapter II where the electron velocity distribution is falling quite rapidly above this energy. The cross section minimum near 0.1 eV is similar to the Ramsauer minimum seen in the noble gases. The accuracy of these cross sections was quoted as 25-50% (Ref 47).

The excitation cross section for the resonance transition (6S-6P) in Cs has been calculated and measured many times over the past few years. The two primary experimental techniques have been optical excitation (Ref 66) and electron swarm experiments (Refs 48,49). The results of these experiments are shown in Fig. A2 with the curves labeled ZAPESOCHNYI and NOLAN for the two principle investigators. The agreement in peak magnitude between these curves is within 25%. Several theoretical calculations of the 6S-6P cross sections have also been made using the Born approximation (Ref 25), a modified Born approximation (Ref 20), and the Seaton Impact Parameter (IP) technique (Ref 58). These are also shown in Fig. A2. As can be seen, the only theoretical calculation that gave even fair agreement with the experimentally determined cross section was the IP method. Because there were several different cross sections, a method had to be found for choosing one or the other. The only data available for checking the cross sections were the electon drift velocity measurements of Nolan and Phelps (Ref 48).

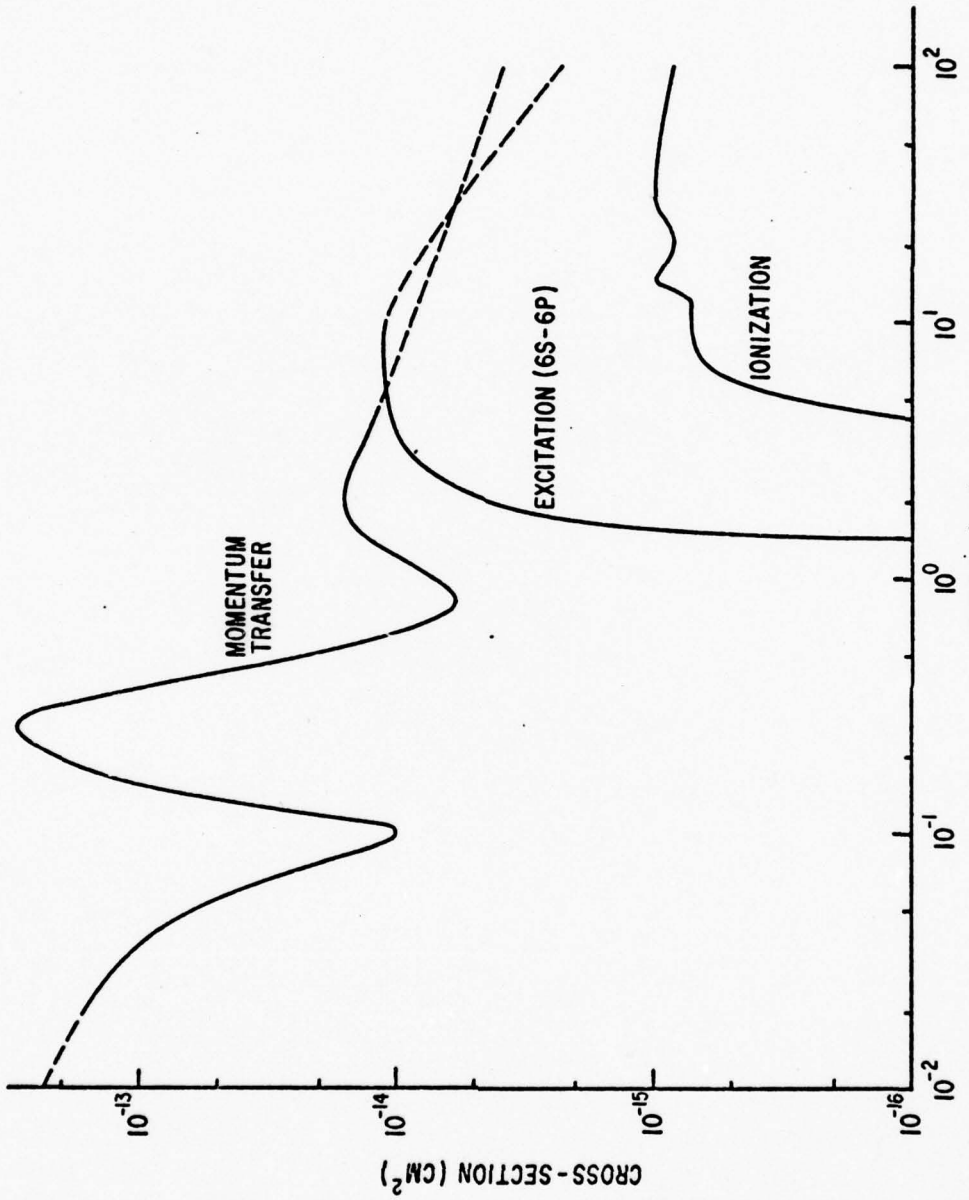

Fig A1 Cesium Electron Cross Sections

The Nolan and Phelps experiments were performed with one part Cs in about 10^5 parts of Argon. They measured the electron drift velocity over a range of E/N from $3x10^{-19}$ to $3x10^{-18}$ volt-cm^2. Then they used a Boltzmann analysis with the then available momentum-transfer cross sections in Cs and Ar. As in the previously described electron swarm experiments, they tried several excitation cross sections to match the data. The same thing was done for each of the cross sections shown in Fig. A2 using the Boltzmann transport code and the more recent momentum-transfer cross sections of Nighan and Postma (Ref 47). The results are plotted in Fig. A3. The experimental drift velocity data are represented by the solid dots. Clearly, the NOLAN cross sections give the best agreement. The ZAPESOCHNYI and IP curves are within 10% of each other. As a result of this brief study, the NOLAN cross sections were used in all of the calculations. As a check on the sensitivity of the Boltzmann analysis results to the particular excitation cross section, all of the functions in Fig. A2 were used. The results for all but the Born and Felden cross sections were negligibly different. It is the NOLAN cross section for the Cs 6S-6P transition that is shown in Fig. A1.

Other transitions in Cs had to be considered also, including excitation to levels above the 6P state from either the ground state or the 6P state. The latter could be especially important for large fractional inversions in the 6P state as might occur in the postulated Cs_2 laser. Sources of cross section data for direct excitation from the 6S to higher levels were both theoretical (Ref 20) and experimental (Refs 13,68). Typically, the largest cross section was for the 6S-5D transition, and its value was about $4x10^{-16}$ cm^2 either by theory or experiment. For two-step excitation, the "effective" cross section, as determined by Devyatov

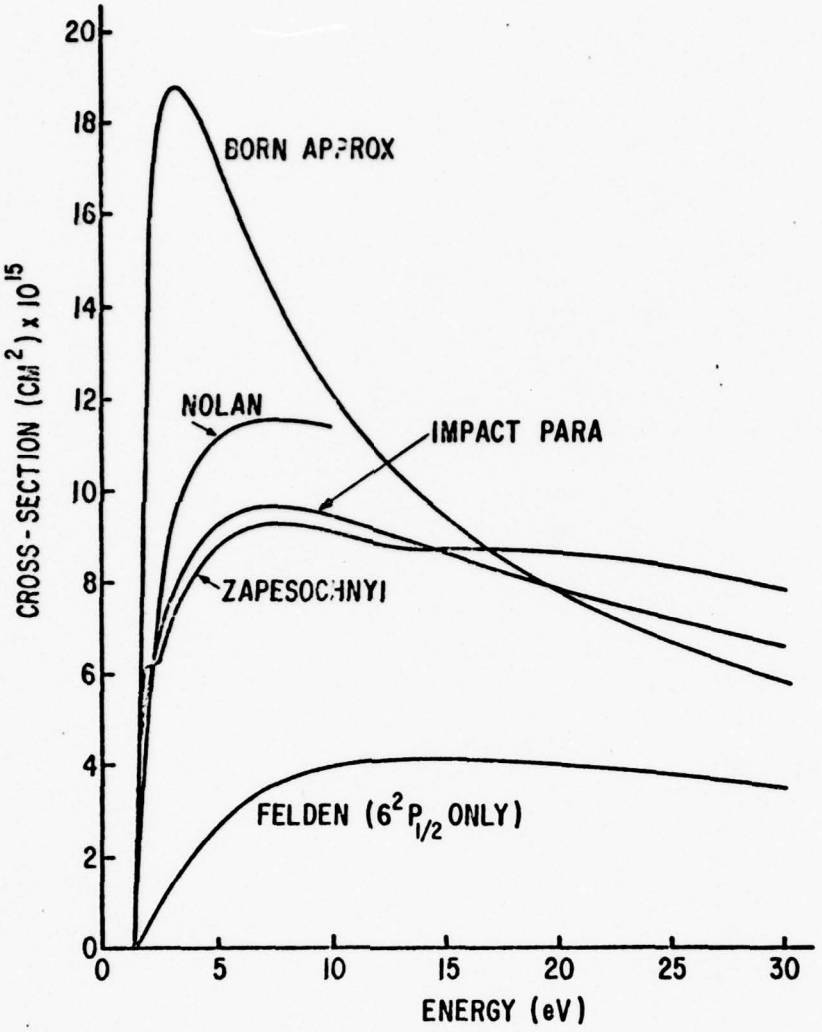

Fig A2 Cesium Electron Excitation
(6S - 6P) Cross Sections

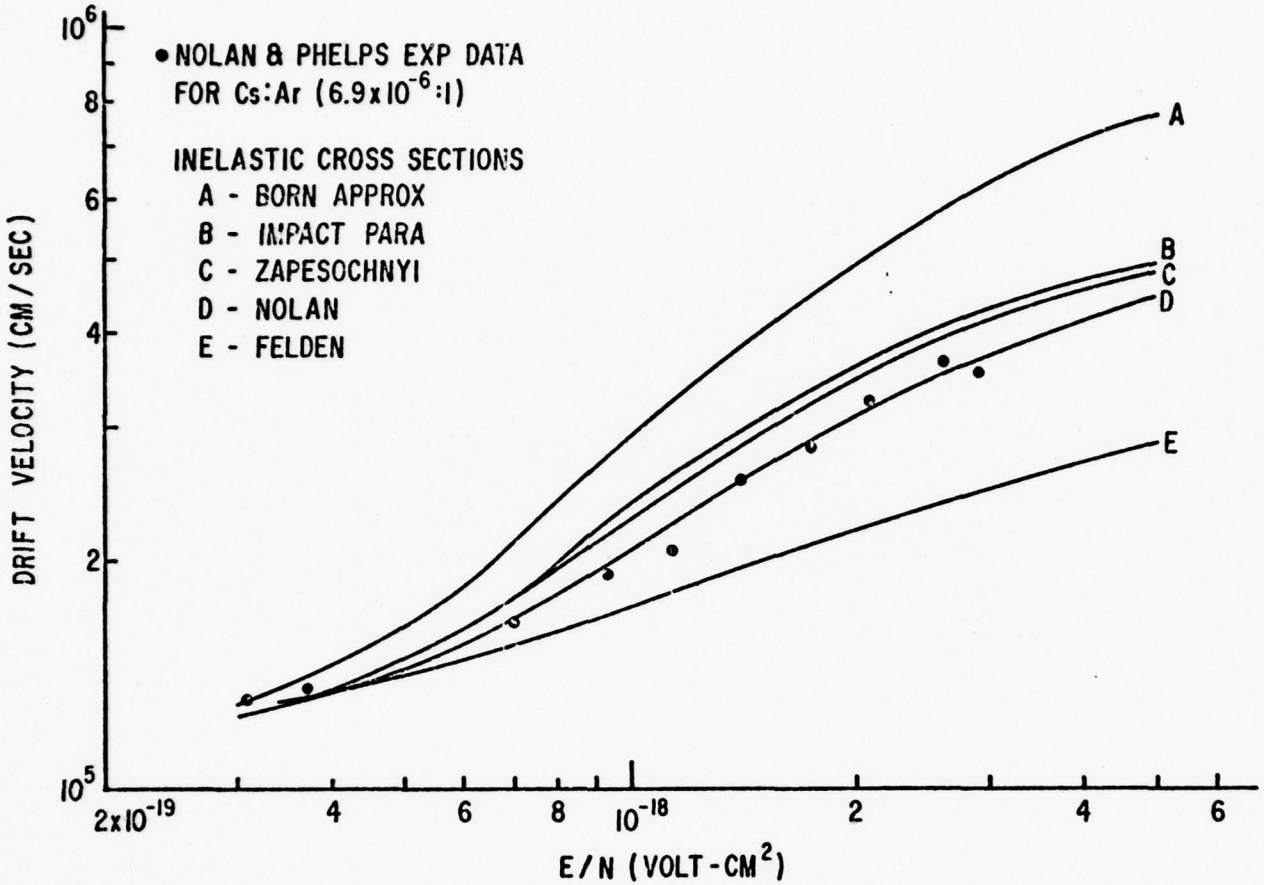

Fig A3 Electron Drift Velocity inCs:Ar for Several Different Excitation Cross Sections

et al, was about 3×10^{-14} cm^2 for the 6P-5D transition, the largest of those he measured (Ref 13). These values were determined from a combination of optical and electronic measurements in a low pressure gas discharge. Because there were several processes occurring in that experiment and the cross section values depended on knowing atomic densities of each state, they are subject to considerable uncertainty. Therefore, it was decided to make an independent estimate of those cross sections using Seaton's classical Impact Parameter method. This technique is described next.

One of the most common methods that has been used to estimate an unknown cross section has been the Born approximation. The problem has been that the cross section at low energies, near threshold, is usually overestimated quite significantly (e.g. see Cs 6S-6P Born cross section in Fig. A2). Seaton (Ref 58) has modified this approach for the case of optically allowed transitions. For these transitions, large impact parameters contribute significantly to the cross section. His technique was to incorporate conservation of probability ($P_{ji}<1$) into the Born approximation. The P_{ji} is the probability of a transition from state i to state j. When the coupling between the two states is strong, the cross section $Q(i \rightarrow j)$ for this transition is given by (Ref 58)

$$Q(i \rightarrow j) = \frac{1}{2} R_1^2 + \int_0^\infty P_{ji}(R_i) 2\pi R_i dR_i \qquad (A15)$$

where R_i is the impact parameter and R_1 is the value of R_i where $P_{ji}=1/2$. The value of P_{ji} was calculated from time dependent perturbation theory and was expressed in terms of the oscillator strength, f_{ji}. The final approximation that Seaton made was conservation of relative angular mo-

mentum. With this, the final expression for Q(i j) is (Ref 58)

$$Q(i \rightarrow j) = \frac{8(I_H)^2}{\Delta E W_i} f_{ji}[1/2\ \xi(\beta_1) + \phi(\beta_1)]\pi a_o^2 \qquad \text{(A16)}$$

where W_i = initial kinetic energy of the electron

ΔE = energy separation of the two states

I_H = 13.6 eV

$\beta_1 = [2\Delta E f_{ji} I_H \xi(\beta_1)]^{\frac{1}{2}} / W$

W = average kinetic energy

a_o = 0.529 Å

and $\xi(\beta_1)$and $\phi(\beta_1)$are functions tabulated in Seaton's paper. They are also expressable in terms of modified Bessel functions (Bassett functions), see for example Ref 1:374. To calculate Q(i→j), one first chooses β_1, calculates W, then W_i, and finally the cross section. The values for the oscillator strengths are taken from Stone (Ref 60) and Fabry (Ref 18). Since all of these values were for specific transitions, one atomic J value to another, they had to be averaged according to the expected population of the $6^2P_{1/2}$ and $6^2P_{3/2}$ states, a ratio of 1:2. The resulting transitions, ΔE, and weighted f_{ji} are given in Table A1.

Table A1 Cs Oscillator Strengths

Transition	ΔE(eV)	f_{ji}
6P-5D	0.36	0.325
6P-7S	0.87	0.294
6P-6D	1.36	0.45

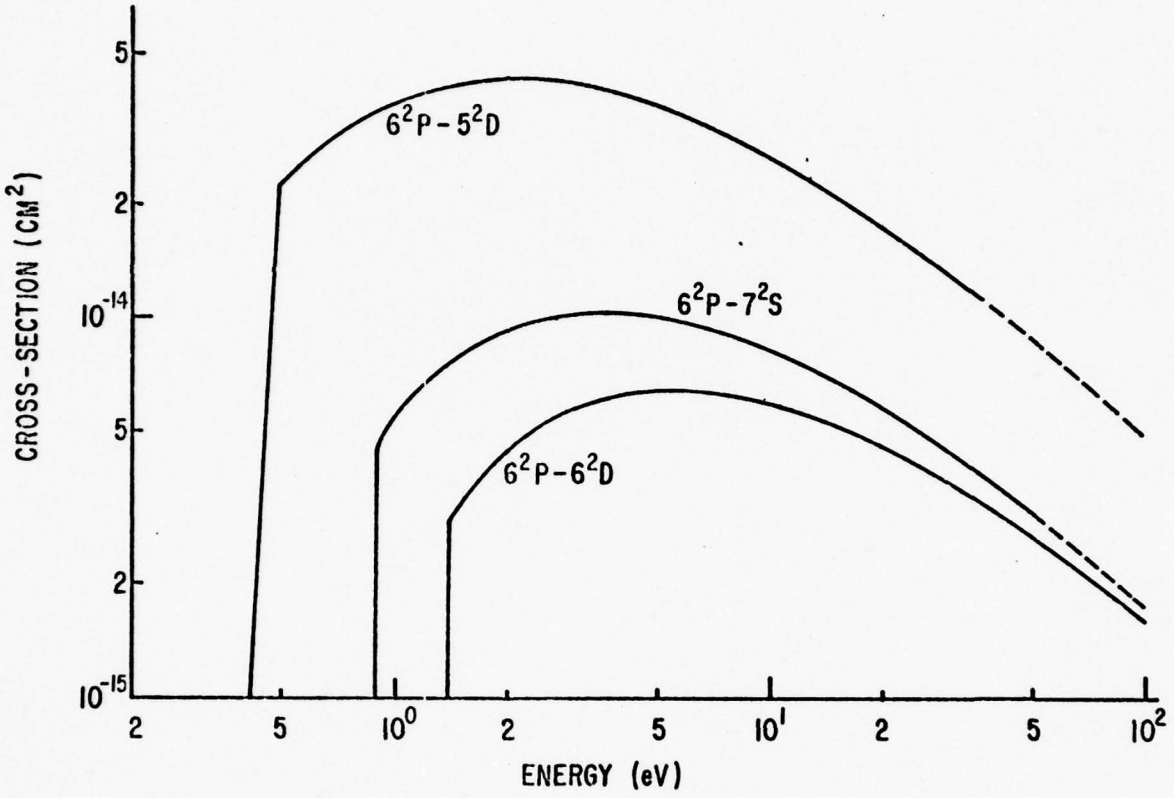

Fig A4 Cesium Electron Excitation Cross Sections from 6P State to Higher Levels, Impact Parameter Theory

The cross sections calculated from Eq. A16, based on the above values, are shown in Fig. A4. All the curves were cutoff just above threshold energy. As expected, the largest cross sections are for the 6P-5D transition. The maximum value was about $4x10^{-14}$ cm^2 compared with $3x10^{-14}$ cm^2 in Ref 13. This was fairly good agreement considering the uncertainties involved in both the theory and experiment. The other comparisons are 1.0 vs $0.65x10^{-14}$ cm^2 for the 6P-7S and 0.65 vs $0.20x10^{-14}$ cm^2 for the 6P-6D transitions. In all cases, the IP method gave larger cross sections; even so, the effect of these two-step processes on the discharge efficiency was not large. The discharge efficiencies shown earlier, Fig. 3, had assumed a fractional inversion ([6P]/[6S]) of 0.01%. Calculations were also made for a 1% inversion. As can be seen in Fig. A5, the discharge efficiency was still quite high. However, as the fractional inversion was increased further, the discharge efficiency started to drop off rapidly. For the large inversions that appeared to be necessary for gain in the Cs_2 system, the efficiencies fall below 50%.

The ionization cross sections in Cs have been measured using the crossed atomic and electron beam technique. The results of the two principle experimenters agree quite well (Refs 50,69) in the threshold region and up to 30 eV, the limit of one of the experiments. The cross sections obtained from those references are shown in Fig. A1. The structure in the curve is attributed to ionization not only of the 6S electron, but also to ionization of some of the inner shell electrons such as the 5P and 5S. Although important in some applications, this structure was not evident in the results of these studies, probably because Cs ionization was generally very small (see for example Figs. 3 and 4).

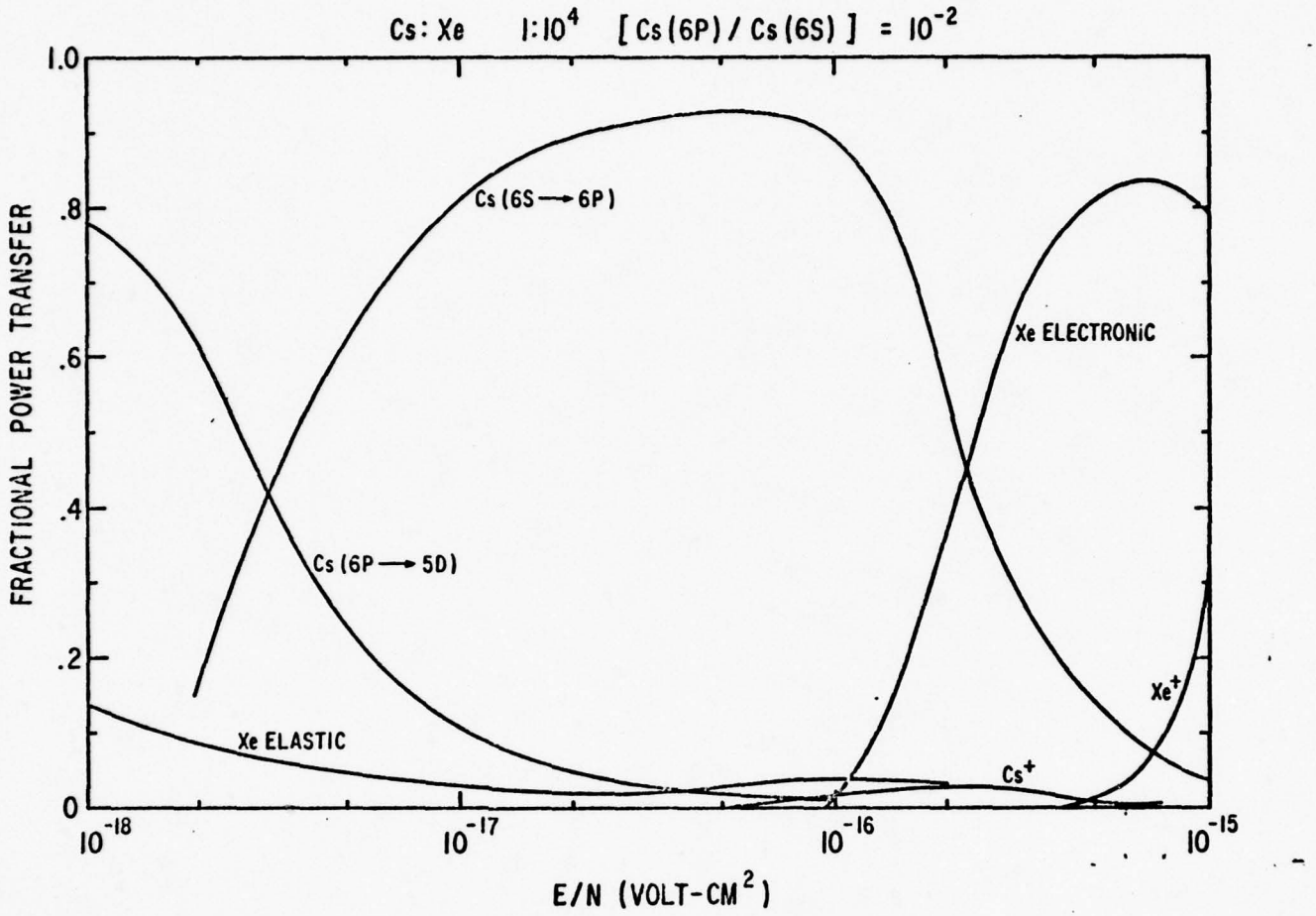

Fig A5 Discharge Efficiency in Cs/Xe for 1% Atomic Inversion

Xenon Electron Cross Sections

All of the Xe cross sections used in this study are shown in Fig. A6. The momentum-transfer cross sections for Xe are quite well known. The swarm technique was used by Frost and Phelps to determine the cross section, and these results are believed to be good to ~10% (Ref 22). The Xe data show the typical Ramsauer minimum near 1.0 eV as was seen in Cs.

The electronic excitation cross sections were taken from Schaper and Schriebner (Ref 55), and the ionization cross sections from Rapp and Englander-Golden (Ref 53). The accuracy of these cross sections was not considered to be as good as for the momentum-transfer cross sections. However, because of their relative size and the threshold energies, they do not seriously affect the discharge efficiency in the range of E/N of 10^{-17} to 10^{-16} volt-cm^2. At higher E/N values, these processes start to take up energy from the Cs electronic states and are responsible for limiting the upper end of the attractive operating region (see Fig. A5). If one lowers the Xe density relative to that of Cs, say to 10^3 from 10^4, these ionization and electronic processes in Xe have very little significance (see Fig. A7 which is a plot of the power transfer for the 10^3 ratio). As a result, the analysis was not seriously affected by a large uncertainty in the Xe excitation and ionization cross sections.

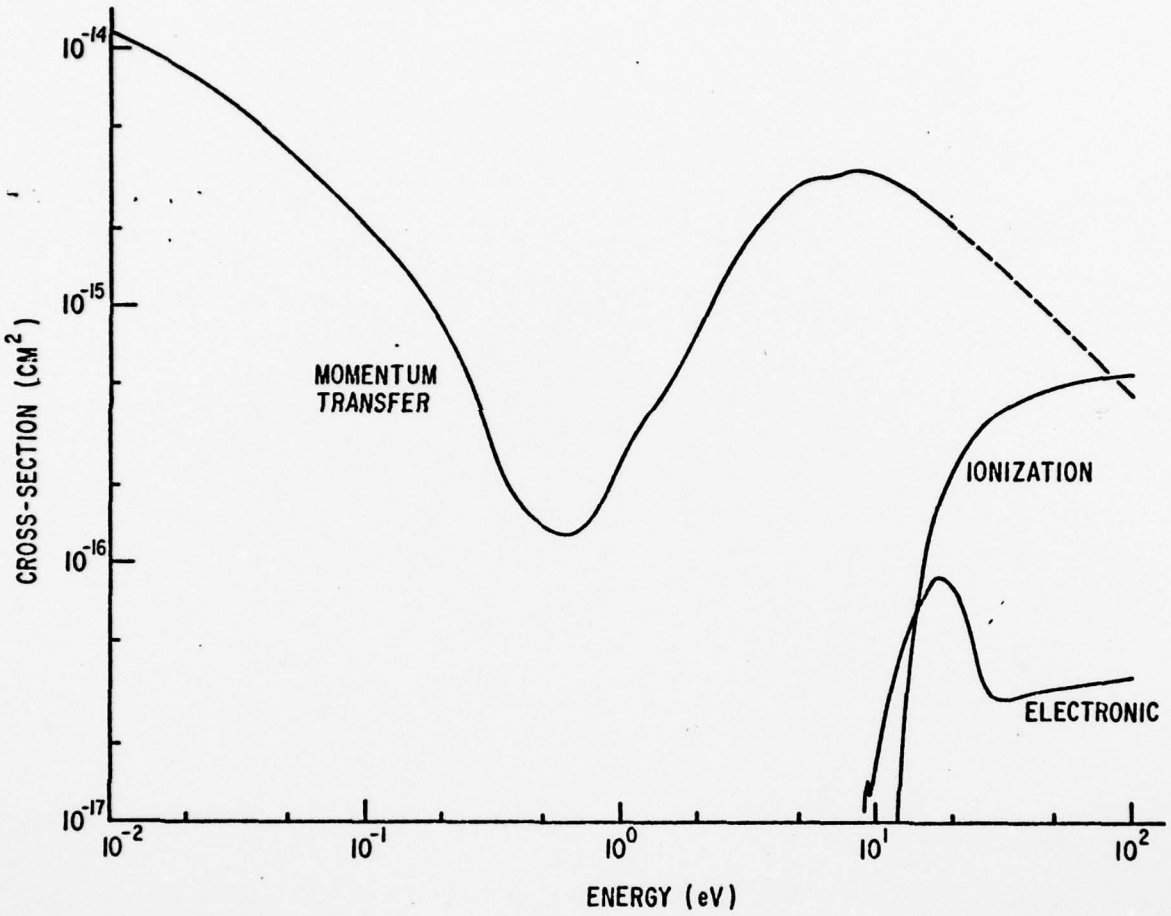

Fig A6 Xenon Electron Cross Sections

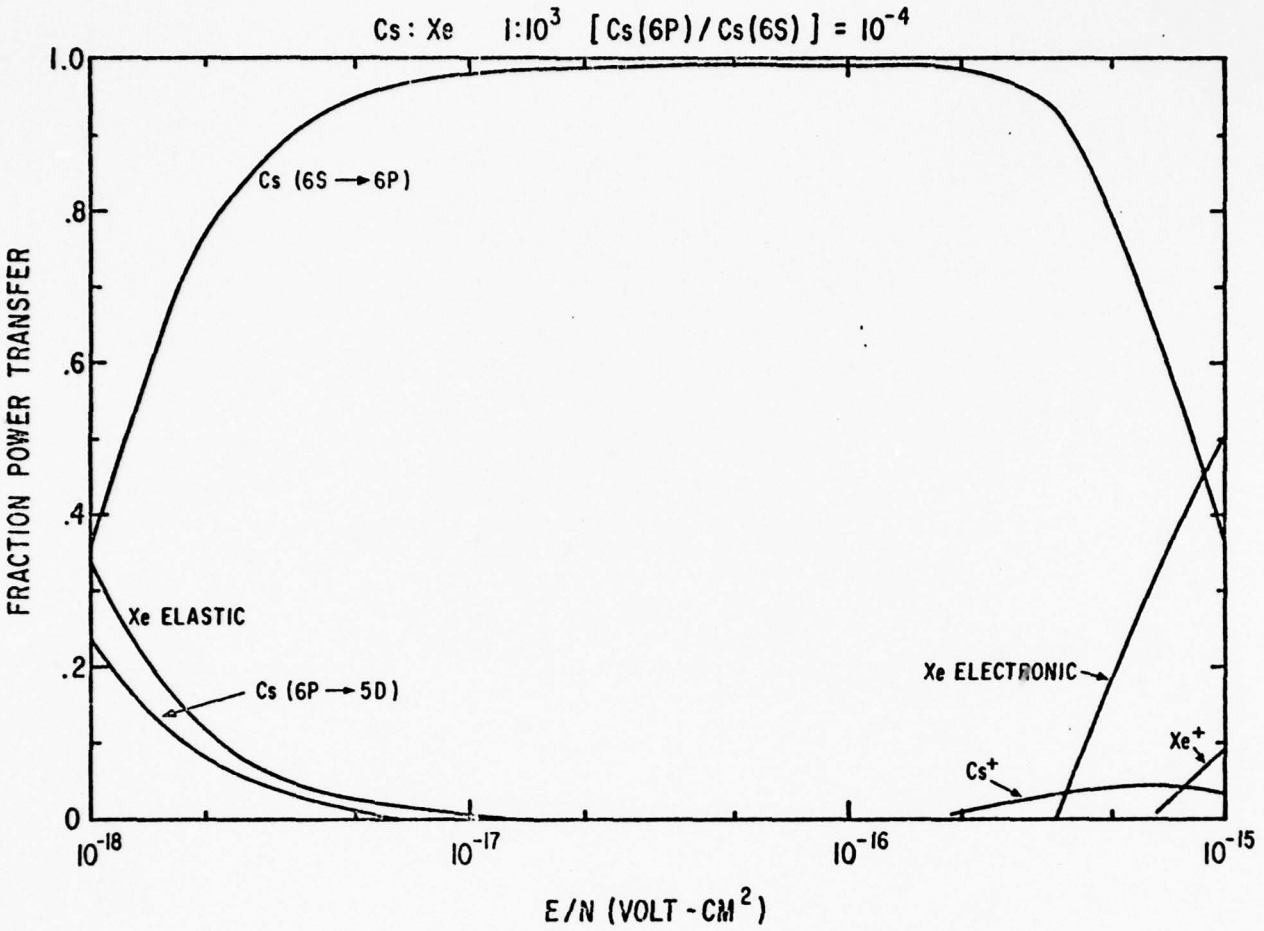

Fig A7 Discharge Efficiency in Cs/Xe for Density Ratio of $1/10^3$

Appendix B. Potential Curve Calculation

Over the years many different techniques have been used to derive potential energy curves from spectroscopic constants. Some of the more common methods are a quadratic approximation near the bottom of the potential well and the Morse potential. These forms are fairly limited and do not make full use of all the information that might be available. For instance, they use only D_e, R_e, and ω_e. The most general approach is the Rydberg-Klein-Rees (RKR) method (Ref 54). Originally it was a graphical technique, but it has been extended to analytical solutions for some limited cases and to computerized solution in the most general case.

The basic approach of the RKR method is to determine the classical turning points, R_+ and R_- for a particular vibrational energy U by means of (Ref 54)

$$R_{\pm} = (f/g + f^2)^{\frac{1}{2}} \pm f \tag{B1}$$

where f and g are given by

$$f(U) = \frac{1}{2\pi(2\mu)^{\frac{1}{2}}} \int_0^{I'} [U - E(I,K)]^{-\frac{1}{2}} \, dI \tag{B2}$$

$$g(U) = \frac{1}{2\pi(2\mu)^{\frac{1}{2}}} \int_0^{I'} \frac{\partial E}{\partial K} [U - E(I,K)]^{-\frac{1}{2}} \, dI \tag{B3}$$

In these expressions, E(I,K) is the sum of the vibrational and rotational energies for any level up to U expressed in terms of the radial momentum, $I = h(v + 1/2)$ and angular momentum, $K = J(J + 1)h^2/8\pi^2$ variables. The upper level of integration, I', is reached when E = U. Rees solved the integral analytically for J = 0 and E cubic in v, that is for the case

where ω_e, $\omega_e x_e$, and $\omega_e y_e$ are known (see Eq. 32, Chapter IV). The result is presented in terms of Jacobian Elliptic Functions (Ref 1:567) and the Weierstrassian Zeta Function (Ref 1:635). Rees' final equations are not reproduced here because several pages are required to fully define all the terms and would contribute very little to the discussion. The Rees analytic solution for the cubic case was programmed on the AFWL CDC 6600 computer and used to develop the initial Cs_2 potential curves. To check the validity of the program, the results were compared with a Br_2 test case in Rees' paper and all turning points agreed to within $\pm$ 0.15%. This was an error of less than 0.01 Å at the very high vibrational levels.

Just prior to the submittal of the absorption paper (Ref 5) for publication, a copy of a computer program developed by D. Albritton of NOAA in Boulder, Colo. was obtained. His program solved the RKR integrals (Eq. B2 and B3) using Gaussian integration. That program could make use of up to nineteen vibrational coefficients so it was used to calculate the final potential curves. The differences between using a cubic or quartic expansion were negligible except for large ($\sim$60) values of v. In any case the final potentials were calculated using the NOAA computer program with all the vibrational and rotational constants available from Table III.

Appendix C. Heat Pipe Discharge Experiment

The purpose of the heat pipe discharge experiment was to observe the Cs_2 emission from a discharge. It was not to be one of the principle sources of data for this research, but rather was to be an educational tool and to give some insight as to the effects of electrons on the Cs_2 dimer. The information to be obtained was qualitative in nature because there was not enough inert gas in the discharge region for the normalization that had been done in the fluorescence experiment. The primary source of information on the kinetics in the discharge was the shape of the emission spectrum. In particular, the relative strengths of the $a^3\pi$ and $A^1\Sigma$ emission were of interest. As will be shown, the spectrum was similar to that seen in fluorescence with some minor changes that did contribute to the overall understanding of the Cs_2 molecule.

Heat pipe ovens have been used for several years to achieve very uniform temperature metal vapors (Refs 63,64). In 1971, a heat pipe oven was modified for the first time for glow discharge operation, specifically for the study of the emission spectra of the alkali dimers (Ref 59). That experiment was also the first time that the Cs_2 emission peaks at 1.14 and 1.20 microns had been observed in a discharge, and reported. The experiment described in this appendix was similar in design, although much better resolution was available (Sorokin and Lankard in Ref 59 used a prism monochromator).

The experimental setup is shown in Fig. C1. The basic heat pipe was a ceramic tube surrounded by a temperature controlled oven. Inside each end of the tube was a roll of stainless steel mesh. These rolls were in physical contact with the aluminum housings at the tube ends

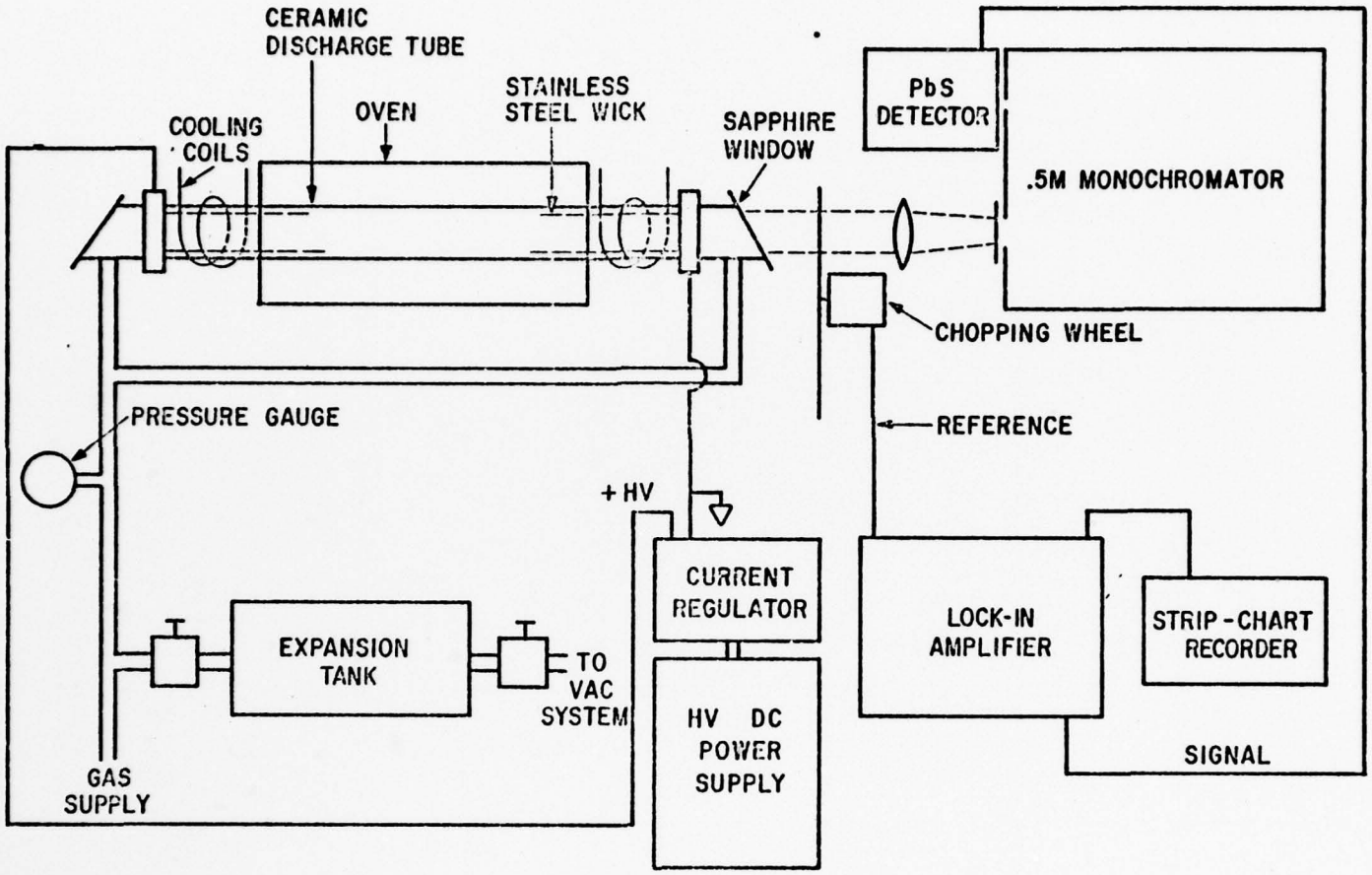

Fig C1 Schematic Diagram of the
Heat Pipe Discharge Experiment

and served as the electrodes for the discharge. The sapphire windows were held on by atmospheric pressure. Cooling coils containing water were used to keep the ends of the tube cold. The gas pressure was held constant when the pipe was heated through the use of a large volume expansion tank. A current-regulated power supply was used to control the discharge operation. Current control was available over the range of 5 - 40 ma. The voltages were measured from cathode to anode by a Hewlett-Packard Model 2401C Integrating Digital Voltmeter. The emission signal was observed at the cathode end and was detected in much the same way as for the other experiments.

The heat pipe was filled by placing two grams of Cs in the anode end under positive Argon flow. Then the windows were put in place, and the system was evacuated to eliminate gaseous contaminants, especially oxygen. For normal operation, the inert gas pressure was increased to the Cs vapor pressure expected at the desired temperature. Then the oven was turned on. According to the theory of the heat pipe oven, the Cs vapor in the hot region diffuses outward toward the cold region (Ref 19). As shown in Fig. C1, all along the inside of the ends of the ceramic pipe is a roll of stainless steel mesh on which the Cs condenses. If sufficient Cs is present to wet the mesh, the mesh will act as a wick and the liquid Cs moves back into the hot zone by capillary action (Ref 19). The inert gas is outside the oven and discharge region and serves to keep the Cs from diffusing too far from the hot zone. Several papers have been written in the past explaining the operation in more detail, and they show that the temperature in the oven is maintained very uniformly, within a few degrees Kelvin, along the entire hot zone (Refs 19, 63, and 64). For this experiment, there were only two thermocouples, one

in the center and one on the cathode end. They were usually within 10°C. Not as good as one would like, but then the oven did not work perfectly, as will be explained.

In the discharge experiment, the wicks also served as the electrodes, and the glow discharge took place only in the hot region between the wicks where, theoretically, there was only metal vapor. The emission from the discharge was focused on the entrance slit of a 0.5 m Czerny-Turner monochromator and detected by the same PbS detector used in the absorption experiments. Lock-in techniques and a strip-chart recorder were also used to record the data. A typical scan, using Helium as the buffer gas, is shown in Fig. C2. There was 3.3 torr of He and T = 324°C. This scan has not been corrected for absorption or spectral response. The length of the absorption path was very uncertain due to the extensive discharge region. The spectral response was measured and varied less than 10% between 1.0 and 1.3 microns.

Perhaps the best way to explain the spectrum in Fig. C2 is in comparison with Fig. 17, which shows the optical fluorescence of Cs_2 with no buffer gas at a similar temperature. Because of the way the heat pipe works, there was little He in the discharge region. Looking first at the shorter wavelengths, we see there is only a very small amount of B-state emission in the discharge. This contrasts sharply with that seen in the optical pumping spectra and implies that there may be transfer from the $B^1\pi$ to the $A^1\Sigma$ via electron collisions. The resonance lines are much stronger in the discharge. The small peaks at 0.876, 0.917, 1.0024, and 1.0123 microns represent the $6^2D_{3/2} - 6^2P_{1/2}$, $6^2D_{5/2} - 6^2P_{3/2}$, $4^2F_{3/2} - 5^2D_{5/2}$, and $4^2F_{7/5} - 5^2D_{5/2}$ transitions in Cs. Some of these should be two lines, but the resolution was not sufficient to show the separa-

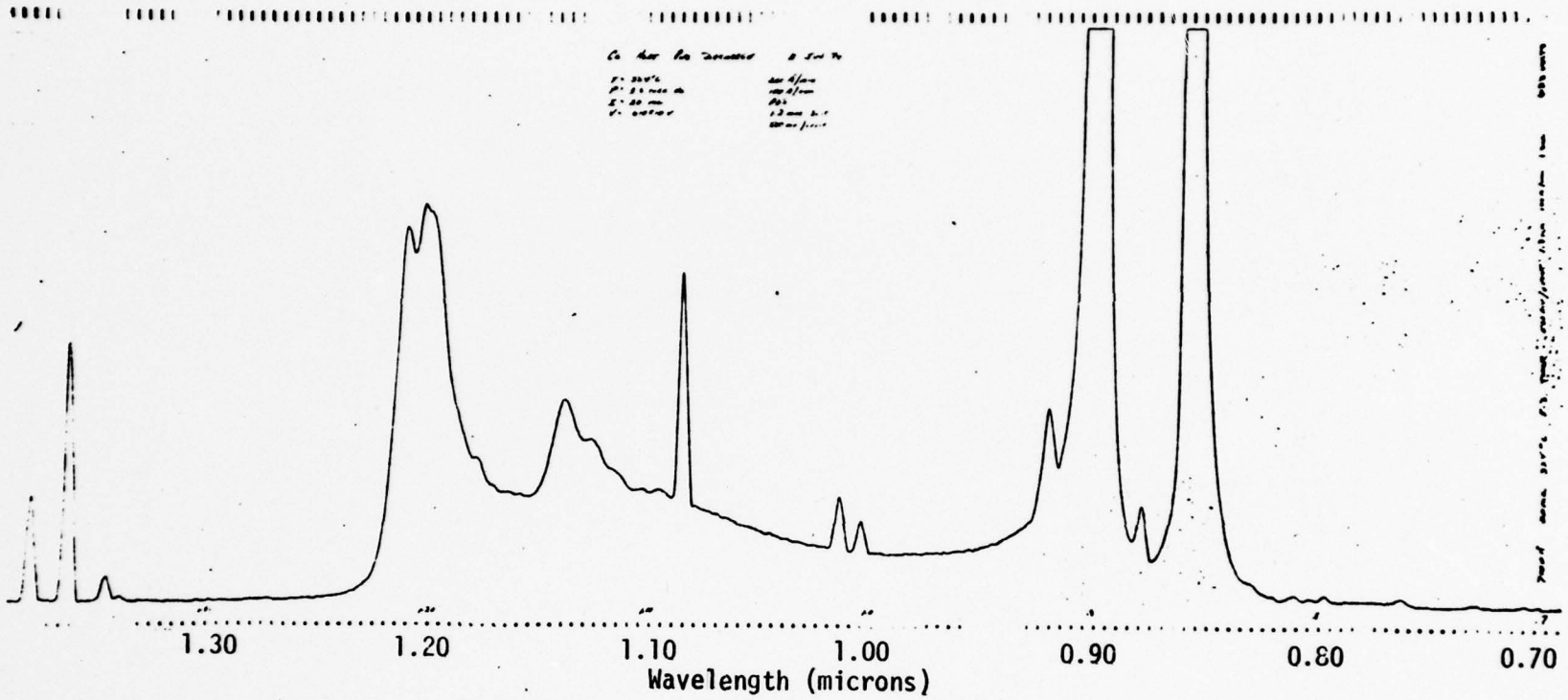

Fig C2 Cs_2 Emission from Heat Pipe Discharge

tion. The strongest one of the pair is the one cited. The 1.08 micron line is a He transition, $2^3P - 2^3S$. The presence of this line indicates that there was some He in the discharge, but not very much. This is a very strong transition in He and would be much more intense if the He pressure were close to 3.3 torr, the Cs vapor pressure at that temperature.

The rest of the spectra to 1.30 microns originates from the Cs_2 $A^1\Sigma$ and $a^3\pi$ (very little) states. No detailed vibrational structure is visible because the resolution was 40 Å. The shape of the discharge spectra is very similar to the equilibrium spectra shown in Fig. 22, except for $\lambda > 1.22$ microns. In contrast, in an optical pumping experiment at a similar temperature, and, also, with no buffer gas present (Fig. 17), the molecules are clearly not in equilibrium. Evidently, the electrons are more effective at thermalizing the molecules than the Xe. Since the molecules appear to be in thermal equilibrium, some emission should be expected in the region 1.22 microns, as there was for the high Xe densities. Because there was very little emission in that region, the electrons may also be more efficient for quenching. The remainder of the observed spectrum consists of lines at 1.342, 1.359 and 1.376 microns. These are the $7^2P_{3/2} - 5^2D_{3/2}$, $7^2S_{1/2} - 6^2P_{1/2}$, and $7^2P_{1/2} - 5^2D_{3/2}$ transitions respectively.

The current dependence of the emission was measured from 5 - 40 ma. The molecular emission was constant from 10 - 30 ma, decreased rapidly for currents below 10 ma, and decreased slowly as the current was increased above 30 ma. The weaker emission at low currents was most likely due to the fact that there was less pumping. At the higher currents, the cause of the intensity decrease was probably electronic dissociation of the $A^1\Sigma$ molecules.

A final observation points out some of the difficulties associated with this particular experiment. As already mentioned, at 1.083 microns there was a He line, indicating that there was some He in the discharge region. If the heat pipe were working properly, this would not have occurred. The problem most likely arose because Cs was loaded into only one end of the tube and did not diffuse to the other end. Also, more than two grams were probably required to wet both wicks. Therefore, the Cs diffused out of the center section and never came back. The experiment was not repeated to correct these deficiencies for primarily one reason. The original purpose had been satisfied. Some of the most important molecular behavior had be seen. Those effects could not be quantified further for two reasons. The first was the inability to accurately correct for the absorption. The second was that without sufficient inert gas present in the discharge region, the spectrum could not be normalized as had been done in the fluorescence experiments. Therefore, the conclusions were qualitative, but they confirm that the electrons are more efficient for thermalizing and quenching the molecules than the inert gas atoms--as one would expect. This also implied that the gain in a discharge might even be lower than was determined in the fluorescence experiment. Therefore, on the basis of this preliminary discharge experiment, Cs_2 appeared to be even more unacceptable for high power laser applications.

Appendix D. List of Symbols

Symbol	Page first used	Meaning
A_a, $A_a(\nu)$	8	Atomic radiation transition rate
A_m, $A_m(\nu)$	8	Molecular radiation transition rate
$A_{v'v''}$	12	Franck-Condon factor
$B(\nu)$	22	Einstein stimulated emission coefficient
B_e	68	Equilibrium rotational constant
B_v	68	Rotational constant for vibrational level v
c	8	Speed of light
$D_{v'v''}$	11	Dipole transition moment between vibrational levels v' and v"
D_e	73	Dissociation energy
E	14	Kinetic energy
E_v	12	Energy of vibrational state v
E/N	25	Electric field/neutral particle density
f(v)	25	Electron velocity distribution function
g_a	8	Atomic statistical weight
g_m	8	Molecular statistical weight
$g_s(\nu)$	23	Stimulated emission coefficient
g*	23	Excited state statistical weight
G(v)	79	Vibrational term value
h	12	Planck's constant
$\hbar$	12	Planck's constant divided by 2π
$I(\nu)$	12	Emission intensity per cm^{-1} at frequency ν

Symbol	Page first used	Meaning
I_a	49	Transmission intensity at 300°K in absorption experiment
I_b	49	Transmission intensity at high temperature in absorption experiment
I_o	8	Atomic emission intensity
I_p	129	Light intensity for stimulated emission
I_{total}	10	Total molecular emission intensity
J	38	Total angular momentum
J^a	70	Total atomic angular momentum
k,k(R)	12	Wavenumber corresponding to an internuclear separation R
k_d	35	Dissociation rate constant for $A^1\Sigma$
k_d^a	117	Dissociation rate constant for $a^3\pi$
k_f	35	Formation rate constant for $A^1\Sigma$
k_f^a	117	Formation rate constant for $a^3\pi$
k_o	61	Wavenumber for atomic line center
k_p	40	Predissociation rate constant for $A^1\Sigma$
k_p^a	117	Predissociation rate constant for $a^3\pi$
k_q	40	Quenching rate constant for $A^1\Sigma$
k_q^a	117	Quenching rate constant for $a^3\pi$
K	8	Boltzmann's constant
K_{eq}	40	Equilibrium constant
ℓ	12	Rotational angular momentum quantum number
M	11	Dipole moment
M_J	70	Component of angular momentum along internuclear axis
M_o	12	Average electric dipole moment

Symbol	Page first used	Meaning
N	8	Particle number density
N^*	17	Particle number density for excited species
N_e	29	Electron number density
$p(r)$	13	Radial componemt of momentum
P	49	Pressure
P'	3	Electron pumping rate from ground to first excited atomic state
P_F	19	Canonical distribution function
$Q(\ell)$	14	Partition function for ℓ
Q'	3	Superelastic rate constant
r	11	radius
r_c	15	Radius where $p'(r_c) = p''(r_c)$
r_n	11	Radius in nuclear coordinates
r_{el}	11	Radius in electronic coordinates
r_t	13	Classical turning point
R, $R(\nu)$	10	Internuclear separation corresponding to a transition of frequency ν
R_d	3	Dissociation rate
R_e	84	Equilibrium separation
R_f	3	Molecular formation rate
R_o	11	Radius inside which $\psi_{v\ell}$ is normalized
R_p	3	Predissociation rate
R_q	3	Quenching rate
R_s	72	Satellite radius
R_{se}	129	Stimulated emission rate
S/N	88	Signal-to-noise ratio

Symbol	Page first used	Meaning
T	8	Temperature in degrees Kelvin
T_c	54	Temperature of fluorescence cell
T_e	86	Energy of potential minimum relative to minimum of ground state potential
v	12	Vibrational quantum number
$V_1(R)$	10	Potential energy of lower state at R
$V_u(R)$	8	Potential energy of upper state at R
$W(\nu)$	11	Transition probability
$\alpha, \alpha(\nu)$	22	Absorption coefficient at frequency ν
α'	16	Phase factor
α_e	68	Rotational-vibrational constant
β	16	$1/KT$
β'	85	Constant for Morse potential
Γ_1	3	Radiative rate for atomic state
Γ_2	3	Radiative rate for $A^1\Sigma$ state
Γ_2^a	117	Radiative rate for $a^3\pi$ state
δ	13	Phase factor
$\delta\alpha$	50	Variation in α
δI	50	Variation in I_a or I_b
Δk	61	$k - k_o$
$\Delta V(R)$	41	$V_u(R) - V_1(R)$
Δx	22	Distance in medium for absorption
$\Delta\omega$	9	Angular frequency shift from ω_o
η_{quant}	3	Quantum efficiency
η_{pump}	3	Pumping efficiency into upper atomic state
λ	13	Wavelength

Symbol	Page first used	Meaning
λ_o	23	Atomic line center wavelength
Λ	70	Component of orbital angular momentum along internuclear axis
μ	12	Reduced mass
$\nu, \nu(R)$	8	Frequency corresponding to an internuclear separation R
ν_o	8	Frequency of atomic line center
ν/N	29	Electronic rate constant
σ_s	129	Stimulated emission cross section
Σ	70	Component of spin along internuclear axis
τ	9	Collision duration
τ_m^o	22	Lifetime of molecule at ν_o
$\phi(\tau)$	9	Phase change due collision of length τ
$\psi_T(r_n, r_{el})$	11	Total wavefunction
$\psi_{el}(r_{el})$	11	Electronic wavefunction
$\psi_v(r_n)$	11	Vibrational wavefunction
ω_e	68	First vibrational constant
$\omega_e x_e$	79	Second vibrational constant
$\omega_e y_e$	79	Third vibrational constant
$\omega_e z_e$	79	Fourth vibrational constant
ω_o	9	Angular frequency = $2\pi\nu_o$
Ω	70	Component of total angular momentum along internuclear axis
[A]	22	Number density of species A

Vita

Rettig Palmer Benedict Jr was born on 18 June 1942 in Louisville, Kentucky. He graduated from High School in Wellesley, Massachusetts, in 1960 and, then, attended Union College in Schenectady, New York, where he received the degree of Bachelor of Science in Physics and a reserve commission in the USAF in 1964. In August 1964, he reported to active duty at Headquarters Ballistic Systems Division, Norton AFB, California, as a project officer in the Engineering Technology Directorate. In September, 1968, he entered the Air Force Institute of Technology at Wright-Patterson AFB, Ohio. While there, he received a regular commission in the USAF. He graduated in June, 1970 with a master's degree in Space Physics and was assigned to the Nuclear Criteria Group Secretariat at the Air Force Weapons Laboratory, Kirtland AFB, New Mexico. After entering the Air Force Institute of Technology again in July, 1973, he completed the course work for the Doctor of Philosphy degree in Aerospace Engineering. Then he was reassigned to the Advanced Laser Technology Division at the Air Force Weapons Laboratory in February, 1975, to complete his dissertation.

Permanent Address: 10 Radcliffe Road
Wellesley, Mass 02181

UNCLASSIFIED
SECURITY CLASSIFICATION OF THIS PAGE (When Data Entered)

REPORT DOCUMENTATION PAGE

READ INSTRUCTIONS BEFORE COMPLETING FORM

1. REPORT NUMBER: AFIT/DS/PH/77-3	2. GOVT ACCESSION NO.
3. RECIPIENT'S CATALOG NUMBER: Doctoral Thesis	
4. TITLE (and Subtitle): INVESTIGATION OF DIATOMIC CESIUM AS A LASER MEDIUM BY ABSORPTION AND FLUORESCENCE SPECTROSCOPY,	5. TYPE OF REPORT & PERIOD COVERED: PhD Dissertation
	6. PERFORMING ORG. REPORT NUMBER
7. AUTHOR(s): Rettig P. Benedict Jr, Major, USAF	8. CONTRACT OR GRANT NUMBER(s)
9. PERFORMING ORGANIZATION NAME AND ADDRESS: Air Force Institute of Technology (AFIT-EN) Wright-Patterson AFB, Ohio, 45433	10. PROGRAM ELEMENT, PROJECT, TASK AREA & WORK UNIT NUMBERS: 626120F 33260598
11. CONTROLLING OFFICE NAME AND ADDRESS: Air Force Weapons Laboratory (AFWL-ALE) Kirtland AFB, New Mexico 87117	12. REPORT DATE: June 1977
	13. NUMBER OF PAGES: 169
14. MONITORING AGENCY NAME & ADDRESS (if different from Controlling Office): 182p.	15. SECURITY CLASS. (of this report): Unclassified
	15a. DECLASSIFICATION/DOWNGRADING SCHEDULE

16. DISTRIBUTION STATEMENT (of this Report)

Approved for public release; distribution unlimited

17. DISTRIBUTION STATEMENT (of the abstract entered in Block 20, if different from Report)

Approved for public release; distribution unlimited

18. SUPPLEMENTARY NOTES

APPROVED FOR PUBLIC RELEASE AFR 190-17.

JERRAL F. GUESS, CAPT, USAF
Director of Information

19. KEY WORDS (Continue on reverse side if necessary and identify by block number)

Cesium
Absorption Spectroscopy
Fluorescence Spectroscopy
Metal Vapor Laser
Alkali Dimer

20. ABSTRACT (Continue on reverse side if necessary and identify by block number)

The potential of Cs_2 as a candidate for a high efficiency laser has been examined using absorption and fluorescence spectroscopy. The absorption spectra of the Cs_2 molecule has been measured over the wavelength range of 0.8 - 1.3 microns. The observed spectra, taken from 182°C to 325°C, were interpreted as both the allowed $X^1\Sigma_g^+ - A^1\Sigma_u^+$ and the normally forbidden $X^1\Sigma_g^+ - a^3\pi_u$ transitions. Based on the

DD FORM 1 JAN 73 1473 EDITION OF 1 NOV 65 IS OBSOLETE

UNCLASSIFIED
SECURITY CLASSIFICATION OF THIS PAGE (When Data Entered)

Ø12 225

Classical Franck-Condon Principle, the temperature dependence of the absorption of the $X^1\Sigma_g^+ - A^1\Sigma_u^+$ transition for the wavelength range 0.9 - 1.21 microns was used to determine the potential energy curve for the $A^1\Sigma_u^+$ state. Also, the potential curve for the $a^3\pi_u$ state was estimated.

The fluorescence of Cs_2 was observed for temperatures between 225°C and 360°C with a xenon buffer gas density ranging from zero to 5×10^{19} cm^{-3}. The spectra were normalized to the atomic line emission via the CsXe red wing of the 0.894 micron line of Cs. The normalized emission was used to calculate the stimulated emission coefficient per excited Cs atom. On the basis of these experiments, gain could possibly be achieved for a 15% atomic inversion. The variations of the integrated normalized emission spectra with xenon density were used to quantify the important kinetic rate constants. There definitely appears to be quenching and predissociation from the $a^3\pi$ to the $x^3\Sigma$ state. As a result, most of the molecules formed into either the $A^1\Sigma$ or $a^3\pi$ are lost through the $x^3\Sigma$. Thus, Cs_2 appears to be a less viable laser candidate than the other alkali dimers such as Na_2.

A (1) sigma.

a (3) pi

A (1) sigma

* allowed transition
** allowed transition state
*** forbidden transition state

5 x 10 to the 19th power /cm.

a (3) pi to the x (3) sigma

AD-A046 354 AIR FORCE INST OF TECH WRIGHT-PATTERSON AFB OHIO SCH--ETC F/G 20/5
INVESTIGATION OF DIATOMIC CESIUM AS A LASER MEDIUM BY ABSORPTIO--ETC(U)
JUN 77 R P BENEDICT

UNCLASSIFIED AFIT/DS/PH/77-3 NL

1 OF 2
ADA
046354

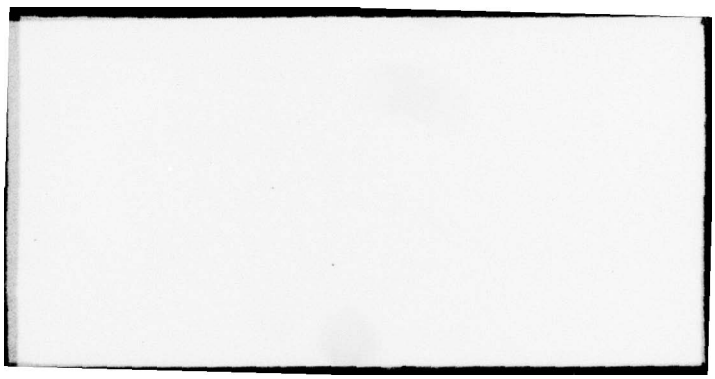

INVESTIGATION OF DIATOMIC CESIUM AS A LASER MEDIUM BY ABSORPTION AND FLUORESCENCE SPECTROSCOPY

DISSERTATION

AFIT/DS/PH/77-3 Rettig P. Benedict Jr.
Major USAF

INVESTIGATION OF DIATOMIC CESIUM AS A LASER MEDIUM BY ABSORPTION AND FLUORESCENCE SPECTROSCOPY

DISSERTATION

Presented to the Faculty of the School of Engineering
of the Air Force Institute of Technology
Air University
in Partial Fulfillment of the
Requirements for the Degree of
Doctor of Philosophy

by

Rettig P. Benedict Jr., B.S., M.S.

Major USAF

June 1977

INVESTIGATION OF DIATOMIC CESIUM

AS A LASER MEDIUM BY ABSORPTION

AND FLUORESCENCE SPECTROSCOPY

by

Rettig P. Benedict Jr., B.S., M.S.

Major USAF

Approved:

Kenneth C. Jungling Chairman	10 June 1977
LaVerne A. Schlie	9 June 1977
Robert L. Hengehold	22 Aug 1977
Donn G. Shankland	29 Aug 1977
Allen Transtrum	6th Sept. 1977
Ernest C. Harko	7 Sept. 1977

Accepted:

B Przemieniecki 14 Sep 77

Dean, School of Engineering

Preface

This report summarizes twenty months of experimental effort devoted to the evaluation of the potential of Cs_2 as a high power laser by absorption and optical fluorescence spectroscopy. This study was an integral part of the visible laser program at the Air Force Weapons Laboratory, Kirtland AFB, New Mexico. The Air Force Weapons Laboratory has been interested in the alkali dimers such as Na_2 and this reasearch was a continuation of that effort to the heaviest alkali molecule, Cs_2. It was performed under the auspices of the Electrical Laser Branch of the Advanced Laser Technology Division at the Air Force Weapons Laboratory.

Two different types of experimental measurements were made in the course of this work, absorption and fluorescence spectroscopy. These are very powerful tools for determining molecular potential energy curves and the rate constants for important kinetics processes. Through the use of these tools and the associated theory, I have been able to increase my understanding and appreciation of physics research.

I would like to extend my sincere thanks to my advisor, Dr. L. A. Schlie of the Air Force Weapons Laboratory for his patience and guidance throughout the course of this project. I would also like to express my great appreciation to Dr. D. L. Drummond, also of the Air Force Weapons Laboratory, for his invaluable advice on both the experimental and theoretical aspects of this work. Finally, I wish to thank the Chairman of my committee, Major K. L. Jungling, for the interest and time that he took in this project.

Rettig P. Benedict. Jr.

Table of Contents

	Page
Preface	iii
List of Figures	vi
List of Tables	viii
Abstract	ix
I. Introduction	1
II. Theory	7
Introduction	7
CFCP Theory of Spectral Intensity	8
Limitations of CFCP Theory	18
Absorption and Stimulated Emission Coefficients	21
Laser Kinetics	24
Electron Kinetics	25
Gas Kinetics (Atomic and Molecular)	33
III. Experimental Description	43
Introduction	43
Absorption Experiment Description	43
Absorption Experiment Error Summary	50
Fluorescence Experiment Description	51
Fluorescence Experiment Data Reduction	59
Fluorescence Experiment Error Summary	64
IV. Results and Analysis	65
Absorption Results	65
Cs_2 Potential Curves	79
Fluorescence Results	87
Cs_2 Gain and Kinetics	108
V. Summary and Conclusions	126
VI. Recommendations	130
Bibliography	131
Appendix A: Boltzmann Analysis	136
Boltzmann Transport Equation	136
Cesium Electron Cross Sections	141
Xenon Electron Cross Sections	152

Appendix B: Potential Curve Calculation 155
Appendix C: Heat Pipe Discharge Experiment 157
Appendix D: List of Symbols 164
Vita 169

List of Figures

Figure		Page
1	Cs_2 Laser Schematic	3
2	Electron Velocity Distribution Function In Cs/Xe	28
3	Pumping Efficiency in a Cs/Xe Discharge	30
4	Electron Rate Constants in a Cs/Xe Discharge	31
5	Schematic Diagram of the Absorption Experiment	44
6	Thermocouple Arrangement in Absorption Experiment	47
7	Sample Absorption Data Scan	48
8	Schematic Diagram of the Fluorescence Experiment	52
9	Spectral Response for the Fluorescence Experiment	56
10	Pump Filter Transmission Curves	57
11	CsXe Potential Energy Curves (Ref 27)	63
12	Experimental Absorption Coefficient in Cs/Cs_2	66
13	Temperature Dependence of Cs_2 Absorption	74
14	Comparison of Experimental Absorption Coefficient and Coefficient Predicted from Cs_2 Potential Curves at 271°C	76
15	Cs_2 Ground State Potential Showing Location of Several Absorption Wavelengths (in microns)	77
16	Cs_2 Potential Energy Curves	80
17	Cs_2 Fluorescence, Broad-band Pumping, Unreduced Data, [Xe] = 0 and [Xe] = 5×10^{19} cm^{-3}	89
18	Normalized Cs_2 Fluorescence, Xenon Density Dependence . .	91
19	Normalized Cs_2 Fluorescence Spectra at [Xe] = 10^{19} cm^{-3}, Temperature Dependence	95
20	Normalized Cs_2 Fluorescence Spectra at [Xe] = $5\times10^{19}cm^{-3}$, Pump Filter Dependence	97

21	Normalized Cs_2 Fluorescence Spectra Compared with Equilibrium Spectra Calculated from Absorption	99
22	Normalized Cs_2 Fluorescence Spectra for [Xe] = 10^{19} cm^{-3}, Pump Filter Dependence	101
23	Cs_2 Fluorescence Spectra for [Xe] = 0, Pump Filter Dependence	102
24	Cs_2 $A^1\Sigma$ Potential Curve Showing Location of Pumping Intensity for Dimer Filter	104
25	Cs_2 Fluorescence for $\lambda > 1.10$ microns, Xenon Density Variation	106
26	Cs_2 Fluorescence Spectra for [Xe] = 0, Using 100 Angstrom Band-Pass Pump Filters, Unreduced Data	107
27	Cs_2 Stimulated Emission and Absorption Coefficients . . .	109
28	Variation of $[Cs][Cs^*]/[Cs_2^*]$ with 1/[Xe] for $A^1\Sigma$ State .	114
29	Variation of $[Cs][Cs^*]/[Cs_2^*]$ with 1/[Xe] for $a^3\pi$ State .	118
30	Xenon Density Dependence of $[Cs_2^*]/[Cs^*]$ for $a^3\pi$	123
	Cesium Electron Cross Sections	143
A2	Cesium Electron Excitation (6S - 6P) Cross Sections . . .	145
A3	Electron Drift Velocity in Cs:Ar for Several Different Excitation Cross Sections	146
A4	Cesium Electron Excitation Cross Sections from 6P State to Higher Levels, Impact Parameter Theory .	149
A5	Discharge Efficiency in Cs/Xe for 1% Atomic Inversion . .	151
A6	Xenon Electron Cross Sections	153
A7	Discharge Efficiency in Cs/Xe for Density Ratio $1/10^3$ . .	154
C1	Schematic Diagram of the Heat Pipe Discharge Experiment .	158
C2	Cs_2 Emission from Heat Pipe Discharge	161

List of Tables

Table		Page
1	Inelastic Electron Processes in $Cs/Cs_2/Xe$	26
2	Atomic and Molecular Processes in $Cs/Cs_2/Xe$	35
3	Spectroscopic Constants for Cs_2 ($X^1\Sigma_g^+$ and $B^1\pi_u$ State) .	81
4	Spectroscopic Constants for Cs_2 ($A^1\Sigma_u^+$ and $a^3\pi_u$ States) .	83
5	Equilibrium Molecular Fractions $[Cs_2^*]/[Cs^*]$	85
6	Experimental and Theoretical $[Cs_2^*][Cs^*]$ Ratios	111
7	Kinetic Rate Constants in $Cs/Cs_2/Xe$	125
A1	Cs Oscillator Strengths	148

Abstract

The potential of Cs_2 as a candidate for a high efficiency laser has been examined using absorption and fluorescence spectroscopy. The absorption spectra of the Cs_2 molecule has been measured over the wavelength range of 0.8 - 1.3 microns. The observed spectra, taken from 182°C to 325°C, were interpreted as both the allowed $X^1\Sigma_g^+ - A^1\Sigma_u^+$ and the normally forbidden $X^1\Sigma_g^+ - a^3\pi_u$ transitions. Based on the Classical Franck-Condon Principle, the temperature dependence of the absorption of the $X^1\Sigma_g^+ - A^1\Sigma_u^+$ transition for the wavelength range 0.9 - 1.21 microns was used to determine the potential energy curve for the $A^1\Sigma_u^+$ state. Also, the potential curve for the $a^3\pi_u$ state was estimated.

The fluorescence of Cs_2 was observed for temperatures between 225°C and 360°C with a xenon buffer gas density ranging from zero to $5x10^{19}$ cm^{-3}. The spectra were normalized to the atomic line emission via the CsXe red wing of the 0.894 micron line of Cs. The normalized emission was used to calculate the stimulated emission coefficient per excited Cs atom. On the basis of these experiments, gain could possibly be achieved for a 15% atomic inversion. The variations of the integrated normalized emission spectra with xenon density were used to quantify the important kinetic rate constants. There definitely appears to be quenching and predissociation from the $a^3\pi$ to the $x^3\Sigma$ state. As a result, most of the molecules formed into either the $A^1\Sigma$ or $a^3\pi$ are lost through the $x^3\Sigma$. Thus, Cs_2 appears to be a less viable laser candidate than the other alkali dimers such as Na_2.

Chapter I. Introduction

During the past several years, there has been considerable interest on the part of the Air Force Weapons Laboratory and others in the metal vapors, and specifically in the alkali dimers, as electronic transition lasers (Refs 16, 28, 51, 52, 66). Their attractiveness stems from their potential for very high efficiency in the visible to near infrared. As a group, the alkali dimers have quantum efficiencies of about 70% and discharge efficiencies greater than 90%. For example, Na_2 and K_2 have been studied by York and Gallagher (Ref 66) with the initial conclusion that both molecules appear to be good electric discharge laser candidates. Lasing has been observed in Na_2 by Henesian, Herbst and Byer (Ref 28) via optical pumping with a doubled Nd:YAG laser. Lasing action was obtained from two different excited molecular states, the $B^1\pi_u$ and $A^1\Sigma_u^+$ states, to the ground state, $X^1\Sigma_g^+$. The spectra and kinetics of Rb_2 have been examined also and, although Rb_2 has potential for lasing, the prospects are not as favorable as for Na_2 (Ref 16). It was a natural extension to consider the heaviest alkali dimer, Cs_2.

The basic premise for this research was that Cs_2 might be a good candidate for a high-efficiency, high power gas laser on the $A^1\Sigma$ - $X^1\Sigma$ transition. The purpose of this project was to explore that premise and to determine whether there were some detrimental factors that had to be considered. Specifically, the objective was to derive the Cs_2 potential curves, estimate the likelihood of gain, and quantify any significant losses in the system. The concept for the proposed Cs_2 system was that of a high temperature ($\sim$300°C) gas electric discharge laser (EDL). One of the noble gases would be used as a diluent and third body. A schematic

diagram of the proposed Cs_2 electric discharge laser is presented in Fig. 1. The diagram has been simplified by showing only the most important atomic levels and by representing the molecular potentials as single energy levels. This is sufficient for the purposes of the introductory discussion.

The proposed Cs_2 laser can be represented as a four-level system. Electrons in the discharge excite ground state (6S) Cs atoms to the 6P level. Then three-body collisions, using a noble gas atom as the third body, form excited Cs_2 molecules in the $A^1\Sigma$ and $a^3\pi$ states. For this project, Xe was chosen as the buffer gas, because it is the most polarizable noble gas. The interaction strength is proportional to the polarizability. Lasing might occur from near the minimum of the $Cs_2^*(A^1\Sigma)$ potential to high vibrational levels in the Cs_2 ground state $X^1\Sigma$. The lower laser level would be depopulated by either electronic dissociation of the molecules or by relaxation to the bottom of the Cs_2 ground state via vibrational-translational (V-T) collisions. The overall efficiency of this laser was expected to be high. The quantum efficiency is near 75% for a lasing wavelength of about 1.2 microns and a pump transition of 1.4 eV (0.89 microns). The pumping or discharge efficiency should be high also because the Cs (6S-6P) cross sections are larger, >100 $\mathring{A}^2$, than those of any of the competing processes such as Cs ionization or Xe electronic excitation or ionization. As will be shown by a Boltzmann analysis, the theoretical discharge efficiencies are better than 80%. The pertinent results of this analysis are discussed in Chapter II along with a detailed discussion of all the important kinetic processes.

In order to examine the potential of Cs_2 as a laser, three things must be known. These are the molecular potential energy curves, the

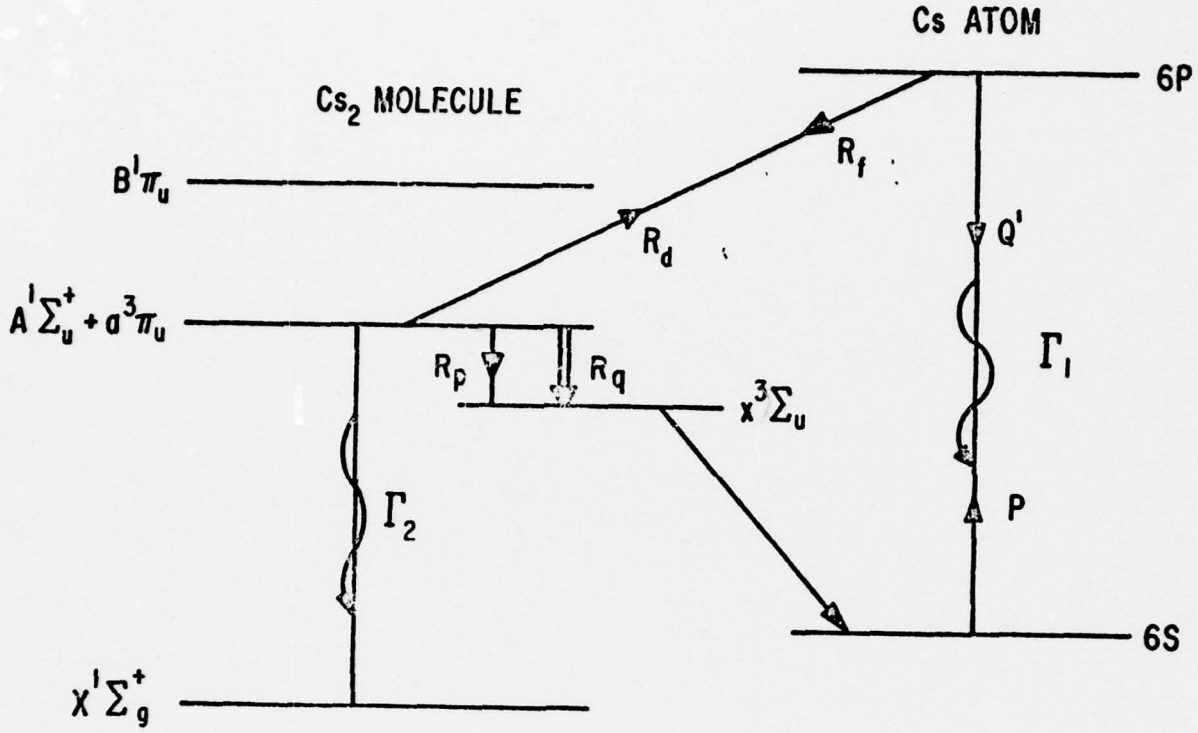

$\eta_{QUANT} \sim 75\%$

η_{PUMP} (6S-6P) $\sim 80\text{-}90\%$

Fig 1 Cs_2 Laser Schematic

possibility of a population inversion (gain) and the critical kinetics parameters. The potential energy curves for the three molecular states of interest, the $X^1\Sigma$, $A^1\Sigma$ and $a^3\pi$, were unknown prior to this research. The vibrational constants for the ground state were known (Ref 37), so they could be used to calculate the $X^1\Sigma$ potential. The excited molecular potentials could be determined by means of absorption spectroscopy. Absorption spectra of Cs_2 were initially observed by Loomis and Kusch (Ref 41), but did not include the entire X - A band because of photographic limitations. Absorption spectra have also been observed by Bayley et. al. (Ref 4) and by Kostin and Khodovoi (Ref 33); however, no detailed analysis was performed. Absorption experiments were carried out as part of this research. The absorption spectra were analyzed according to the Classical Franck-Condon Principle as detailed in Chapter II. The experiment is described in Chapter III and the results, including the Cs_2 potential curves, are given in Chapter IV.

Once the potential curves are available, the stimulated emission coefficient of the molecule can be calculated for an assumed excited Cs atomic state density. In the lighter alkalis, such as Na_2, the $A^1\Sigma$ potential is displaced to longer radii than the ground state (Ref 66). This causes a broad fluorescence spectrum on the red side of the parent atomic line and the possibility of obtaining gain at the longer wavelengths without requiring large fractional population inversions. For example, in Na_2, where the potentials were known, preliminary estimates were that a fractional molecular population inversion of 5% was sufficient to obtain gain (Ref 66). It was expected that the potential curves of Cs_2 were similar to those of Na_2 and that gain might be achievable.

The stimulated emission coefficient can also be determined experimentally, i.e. from fluorescence spectroscopy. Prior to this research, the only Cs_2 emission spectra reported in the literature were the heat pipe discharge experiments of Sorokin and Lankard (Ref 59). Fluorescence spectra were taken as part of this project. As with the absorption, the experimental description is in Chapter III and the results are in Chapter IV. The comparison of the theoretical and experimental determinations of the stimulated emission are also given in Chapter IV.

The final data required for this evaluation of Cs_2 were the kinetic rates as shown in Fig. 1. The rates that are probably the most critical to the ultimate efficiency of this system are the formation rate R_f, into the excited molecular state, and any loss rates out of that state such as R_q or R_p, the quenching and predissociation rates. For most of the analyses, the $a^3\pi$ and $A^1\Sigma$ states were considered as one. In an electrical discharge with sufficiently high electron number density, this should be a good approximation. The two states will be closely coupled by electron spin-exchange collisions (Ref 66). Therefore, in this context, the formation rate would be for the combination $A^1\Sigma + a^3\pi$.

In addition to the formation rate, the most important processes are the losses: dissociation (R_d), quenching (R_q), and predissociation (R_p). The dissociation and quenching are caused by the buffer gas. The dissociation rates should be small because the potentials were expected to be very deep (>6000 cm^{-1}). The quenching and predissociation rates are entirely dependent on the relative location of the $x^3\Sigma_u^+$ and $a^3\pi_u$ potentials. If they do not cross, but rather, are close together deep in the attractive region of the $a^3\pi$, then quenching should be important. If on the other hand, the potentials cross, both

quenching and predissociation should be important. In either of these cases, the losses could be significant.

The fluorescence experiments were performed at several different Xe densities. Using the kinetic theory outlined in Chapter II and the Xe density dependence of the fluorescence spectra, estimates of R_f, R_q, and R_p for the Cs_2 excited states were made. The analysis and results are given in the latter part of Chapter IV.

Finally, all of these data are put together to assess the potential of Cs_2 as a high efficiency laser medium. This assessment is presented in Chapter V along with a brief comparison with the other alkali dimers.

Chapter II. Theory

Introduction

In this chapter, the theoretical analyses used to evaluate the potential of the Cs_2 molecule as a laser will be presented in four sections. First, the Classical Franck-Condon Principle (CFCP) of spectral intensity will be described. This theory is fundamental to all of the subsequent work because it forms the basis for the interpretation of the absorption and fluorescence data. Using this theory, expressions can be written for the normalized fluorescence intensity and absorption coefficient in terms of atomic, rather than molecular densities. This is very useful because the atomic densities are much easier to determine experimentally. These equations do not require a-priori knowledge of the molecular potentials and, in fact, it will be through the use of these equations that the potentials will be determined. As a follow-up to this theory, the subsequent section contains a detailed discussion of the limitations of the CFCP approach and its applicability to this study.

In the third section, the method by which these equations will be used to interpret the absorption data, to determine the potential curves and to predict the gain in Cs_2 from the fluorescence data are discussed. Then, in the last section, the electron, atomic and molecular kinetics processes relevant to the postulated Cs/Cs_2 electronic transition laser are described. The first part of this section describes the electron kinetics which have been analyzed via the Boltzmann transport equation. This analysis demonstrates that the electronic pumping of Cs should be highly efficient. The second part describes

both the atomic and the molecular kinetics processes in $Cs/Cs_2/Xe$. Emphasis is placed on the dominant processes such as molecular formation, quenching and predissociation. The rates of these processes are crucial since they affect the ultimate efficiency of the proposed Cs_2 laser. The last part of that section will describe how the fluorescence data can be interpreted to obtain the magnitudes of these critical kinetic rates.

CFCP Theory of Spectral Intensity

This section contains a review of the basis for the CFCP theory of spectral intensity as it was formulated by Jablonski (Ref 32) and Hedges, Drummond and Gallagher (Ref 27), hereafter abbreviated HDG. The basic approach used in this analysis is to consider a single radiating atom and a perturbing atom that causes the first atom to change state and radiate. The final result of this approach is an equation that describes the molecular fluorescence intensity per wavenumber, between frequency ν and $\nu+d\nu$, $I(\nu)d\nu$, normalized to the total atomic fluorescence intensity, I_o. The equation is (Ref 27)

$$\frac{I(\nu)d\nu}{I_o} = \frac{g_m}{g_a} N\, 4\pi c R^2 \left|\frac{d\nu}{dR}\right|^{-1} \frac{A_m}{A_a} \left(\frac{\nu}{\nu_o}\right)^4 \exp\{-[V_u(R)-V_u(\infty)]/KT\}\, d\nu \quad (1)$$

where g_m and g_a are the statistical weights of the molecule and parent atomic state. N is the perturber density and c is the speed of light. $R = R(\nu)$ is the internuclear radius at which an electronic transition at frequency ν occurs. A_m and A_a are the molecular and atomic radiative transition rates, respectively, and ν_o is the frequency of the atomic transition, atomic line center. The quantity $V_u(R)$ is the potential

energy of the upper state at radius R, K is Boltzmann's constant and T is the temperature in degrees Kelvin. The physical meaning of these terms can be described as follows. The $N\ 4\pi cR^2 \left|\frac{d\nu}{dR}\right|^{-1}$ is the number of perturbers per wavenumber. A_m/A_a is the ratio of the radiative rates. The $(\nu/\nu_o)^4$ term is made up of two factors. The first is the ratio of the photon frequencies (ν/ν_o). The second describes the frequency scaling of the radiative rate $A_m(\nu) = A_m(\nu_o)(\nu/\nu_o)^3$ (Ref 27). The exponential term is the Boltzmann factor for the initial state (the upper state for emission). The usefulness of this equation can be summarized by noting that only atomic densities are involved and that the molecular emission intensity is related to the atomic emission. The advantages will be discussed in more detail later. The rest of this section will be devoted to the development of Eq. 1.

Historically, there have been several ways to determine the spectral intensity from a pair of atoms (for a review see Margenau and Watson, Ref 42, and Chen and Takeo, Ref 10). One of the first theories developed was the Lorentz collisional damping theory. In that approach, the atom radiating at frequency ω_o was regarded as a classical oscillator. There has also been a theory which considers a radiating atom in a static ensemble of perturbers. Since the intensity predicted by this approach is proportional to the probability of the ensemble being in the particular configuration, it is called the statistical, or the quasi-static theory. Both of the above theories can be seen to be limiting cases of the more general Fourier Integral Theory (Ref 10). Starting again with a classical oscillator at ω_o, one looks at the spectral changes due to a collision of duration τ. The oscillator undergoes a rapid phase change $\phi(\tau) = \int \Delta\omega(t)dt$ where $\Delta\omega$ is the frequency shift from ω_o that occurs during the collision.

One can consider two limiting cases, $\Delta\omega\tau<<1$, and $\Delta\omega\tau>>1$. The first corresponds to the Lorenztian or instantaneous collision case and predicts the intensity near ω_o (Ref 10). The resultant intensity distribution has the Lorenztian lineshape. The second limit considers a slow collision or equivalently, large $\Delta\omega$. Therefore, the intensity far from ω_o will arise from a situation where the atoms and perturbers are, to a first approximation, static (Ref 10). For this case, the intensity distribution of the radiation between ν and $\nu+d\nu$ is proportional to the number of perturbers between R and R+dR and is given by (Ref 14)

$$\frac{I(\nu)d\nu}{I_{total}} = N\, 4\pi c R^2 dR. \qquad (2)$$

where I_{total} is the total intensity. This quasi-static theory bears a close analogy to the theory based on the Classical Franck-Condon Principle (CFCP) (Ref 10). In fact, the frequency of the radiation is related to the potentials as $\nu(R)=[V_u(R)-V_l(R)]/h$ where V_u and V_l are the potentials of the upper and lower states and h is Planck's constant. Jablonski (Ref 32) gave the quasi-static theory of line broadening a quantum-mechanical foundation, and it is his development that will be presented first. HDG (Ref 27) extended this to include the temperature dependence and an additional frequency dependence. Theirs is the final result required to complete the derivation of Eq. 1 for the normalized emission intensity. The corresponding absorption coefficient will be determined from their results in a subsequent section.

Next, a review of Jablonski's formulation of the General Theory of Pressure Broadening (Ref 32) will be presented. The initial step is to use statistical theories to determine the probability of an interaction

between the radiating and perturbing atoms, including the possibility of multiple interactions. To isolate the problem to that of only two atoms, one assumes a perturber density low enough so that only binary interactions, or equivalently diatomic molecules, occur and that the nuclear motions are independent. This first assumption is generally met if the perturber density is less than 10^{21} cm^{-3}. The resulting intensity distribution, I/I_{total}, is $nW(\nu)c$ where n is the total number of perturbers equal to $N(4\pi R_o{}^3/3)$ and R_o is the radius of the container. $W(\nu)$ is the probability that a single perturber and radiator interact and cause the emission of a photon of frequency ν. The factor of c, the speed of light, is included to convert to wavenumbers. But before determining $W(\nu)$, a discussion of the basic quantum-mechanical formulation of the problem is given.

The basic calculation of interest is that of determining the probability of a transition between two separate states of the diatomic molecule. This probability is proportional to D^2 where D is the matrix element of the electric dipole moment and is given by (Ref 29,32)

$$D = \iint \psi_T'^{*}(r_n,r_{el})\, M\, \psi_T''(r_n,r_{el})\, d^3r_n\, d^3r_{el} \qquad (3)$$

where ψ_T', ψ_T'' are the total (electronic and nuclear) wavefunctions of the initial and final states respectively, M is the electric dipole moment and d^3r is a volume element for the nuclear and electronic coordinates. According to the Born-Oppenheimer approximation (Ref 32), ψ_T can be separated into a nuclear and electronic part as follows

$$\psi_T(r_n,r_{el}) = \psi_v(r_n)\psi_{el}(r_{el}) \qquad (4)$$

where ψ_{el} is the electronic wavefunction and ψ_v the vibrational wavefunction. Next, using Condon's approximation that M is not a strong function of the nuclear coordinates (Ref 29), D becomes

$$D_{v'v''} = M_o \int \psi^{i*}_{v'} \psi^{f}_{v''} \, d^3r_n = M_o A_{v'v''}. \tag{5}$$

M_o is the average dipole moment, the superscripts refer to the initial and final electronic states, and $A_{v'v''}$ is sometimes called the Franck-Condon factor. This approximation is known as the quantum-mechanical form of the Franck-Condon Principle (Ref 32).

Each of the vibrational wavefunctions will depend on the relative energy of nuclear motion, $E_{v\ell}$, the potential energy, of the particular electronic state, V(r), and the rotational angular momentum. Since only the radial part of ψ_v (or now $\psi_{v\ell}$) is important, $\psi_{v\ell}$ must satisfy the radial part of Schroedinger's equation

$$\frac{d^2\psi_{v\ell}}{dr^2} + \frac{2\mu}{\hbar^2}\left[E_{v\ell} - V(r) - \frac{\hbar^2}{2\mu r^2}\ell(\ell+1)\right]\psi_{v\ell} = 0 \tag{6}$$

where v and ℓ are the vibrational and rotational quantum numbers of the nuclear states, μ is the reduced mass of the couple, and $\hbar$ is $h/2\pi$. There is a separate equation like Eq. 6 for each electronic state. The rotational wavefunctions have not been considered here specifically; however, if they were, they would introduce the transition criterion $\ell'=\ell''$ (Ref 32) arising from the orthogonality of the wavefunctions.

Equation 6 has been solved for the case of a slowly varying potential, V(r). The solution takes the form of $[k(r)]^{-\frac{1}{2}}\cos[\int k(r)dr]$

where $k(r)$ is related to the particle momentum, $p(r)$ by $p(r) = \hbar k(r)$ (Ref 44). This is known as the Wentzel-Kramers-Brillouin(WKB) approximation. One of the requirements for the validity of this solution is that $\left|\frac{dk(r)}{dr}\right| << |k(r)|^2$ (Ref 44). Stated simply, this means that the particle momentum must be reasonably constant over several wavelengths, ($\lambda(r) = 2\pi/k(r)$). The place where this approximation breaks down is the region of the classical turning point (r_t) where $p(r_t) = 0$. The impact of this limitation is discussed in the next section.

Applying the WKB approximation to Eq. 6, one gets (Ref 32)

$$\psi_{v\ell}(r) = \left[\frac{2}{R_o}\,\frac{p(\infty)}{p(r)}\right]^{\frac{1}{2}} \cos\left[\frac{1}{\hbar}\int_{r_o}^{r} p(r)dr + \delta\right] \qquad (7)$$

In this equation $[2p(\infty)/R_o]$ is a normalization constant found from the condition $\int_o^{R_o} |\psi_{v\ell}|^2 dr = 1$, R_o is the radius of the volume inside which $\psi_{v\ell}(r)$ must be normalized and $p(r)$ is the radial component of momentum given by

$$p(r) = 2\mu\left[E_{v\ell} - V(r) - \frac{\hbar^2\ell(\ell+1)}{\mu r^2}\right]^{\frac{1}{2}} \qquad (8)$$

One can identify $\int p(r)dr$ as a phase integral analogous to $\phi(t)$ in the Fourier integral theory (Ref 14). The quantity δ is a phase factor used to match up the solution for $r < r_t$.

One can now proceed to calculate the transition probability $W(\nu)$ of a transition from v' in the initial electronic state to v" in the final state. To get the relative intensity distribution in energy, $D^2_{v'v"\ell}$ must be multiplied by the density of final vibrational states, $\frac{dv'}{dE_{v'}}$. Here the assumption has been made that the vibrational states

are close enough together to assume that v is a continuous function of E_v. The value of $\frac{dv}{dE_v}$ is computed from the boundary condition $\psi_{v\ell}(R) = 0$ and one obtains (Ref 32)

$$\frac{dv}{dE_v} = \frac{\mu R}{\pi \hbar p(\infty)} \tag{9}$$

Finally, $D_{v'v''\ell}$ must be averaged over the angular momentum quantum number ℓ which is distributed according to a partition law, $Q(\ell)$. So the expression for $W(v)$ becomes for a single perturber (Ref 32)

$$W(v) = \int_0^{\ell_{max}} Q(\ell) \frac{D^2_{v'v''\ell}}{\sum_{v''} D^2_{v'v''\ell}} \frac{dv'}{dE_{v'}} \, d\ell \tag{10}$$

Actually it should be a sum over ℓ but for large ℓ_{max}, the sum can be approximated with an integral (Ref 32). Since $D_{v'v''\ell} = M_o A_{v'v''\ell}$ and $\sum_{v''} A_{v'v''\ell} = 1$

$$W(v) = \int_0^{\ell_{max}} Q(\ell) \, A_{v'v''\ell} \frac{dv'}{dE_{v''}} \, d\ell \tag{11}$$

The partition function $Q(\ell)$ can be determined from the partition function for the classical impact parameter ρ and the statistical weight of the state ℓ, $2\ell+1$. The impact parameter is given by

$$\rho = \hbar[\ell(\ell + 1)/2\mu E]^{\frac{1}{2}} \tag{12}$$

where E is the relative kinetic energy of the radiation and perturbing atoms. For large ℓ, one can write $Q(\ell)$ as (Ref 32)

$$Q(\ell) = 3\hbar^2(2\ell + 1)/4R^2\mu E \tag{13}$$

Next the integral $A_{v'v''\ell} = \int \psi^*_{v'\ell} \psi_{v''\ell} dr$ is calculated using Eq. 7

$$A_{v'v''\ell} = \frac{1}{R} \int_{r_t}^{R_o} \left[\frac{p'(\infty)\, p''(\infty)}{p'(r)\, p''(r)}\right]^{\frac{1}{2}} \left[\cos\left(\int_{r_t}^{r} \frac{p'(r) - p''(r)}{h} dr + \delta' - \delta''\right)\right.$$

$$\left. + \cos\left(\int_{r_t}^{r} \frac{p'(r) + p''(r)}{h} dr + \delta' + \delta''\right)\right] dr \qquad (14)$$

The primary contribution to this integral comes from the region of $r = r_c$ defined by $p'(r_c) = p''(r_c)$ because the first cosine term oscillates slowly here. The second cosine term oscillates very rapidly and will be neglected. The significance of $p'(r_c) = p''(r_c)$ becomes clear upon writing out the terms, remembering $\ell' = \ell''$ and switching terms

$$E_{v'} - E_{v''} = V'(r_c) - V''(r_c) = h\nu \qquad (15)$$

This is the CFCP, which states that a transition between electronic states occurs with no change in momentum or position. Since $A_{v'v''\ell}$ is essentially the transition probability and the major contribution to the value of $A_{v'v''\ell}$ comes from the region $r \simeq r_c$, one can see the correspondence between the classical and the quantum forms of the Franck-Condon Principle. Using this approximation, the integral in Eq. 14 is expanded around r_c to compute $A_{v'v''\ell}$. This is sometimes called the "stationary phase" approximation from the analogy with $\phi(t)$ and in essence neglects the nuclear motion.

Substituting Eqs 9,13, and 14 into Eq. 11, one gets for the transition probability

$$W(\nu) = \int \frac{(4\pi R_o^3/3)^{-1}[\pi\hbar^2(2\ell + 1)/2E][2\cos^2(\alpha' \pm \pi/4)]}{[1 - V(r_c)/E - \hbar^2\ell(\ell + 1)/2\mu E r_c^2]^{1/2}|d\nu/dR|} d\ell \qquad (16)$$

where $\alpha' = \frac{1}{\hbar}\int [p'(r)-p''(r)]dr + \delta'-\delta''$ is a quantum-mechanical interference term that is an oscillatory function of the energy of the lower state. Inclusion of this term creates an oscillation of the spectrum as a function of frequency. Assuming that cos α' oscillates rapidly with ℓ, it can be replaced with its average value of 1/2. This is called the "random phase" approximation and smoothes out the vibrational structure. It will be discussed further in the next section of this chapter.

Performing the integration of Eq. 16, multiplying by the number of perturbers $n=N(4\pi R_o^3/3)$, and identifying r_c as $R(\nu)$, one has

$$\frac{I(\nu)d\nu}{I_{total}} = N\ 4\pi c R^2(\nu)[1 - V(R)/E]^{1/2}dR \qquad (17)$$

which in the limit of large kinetic energies, goes to Eq. 2, the classical distribution of intensities for the quasi-static model. This completes Jablonski's treatment of the problem.

The quasi-static theory was extended by Hedges, Drummond and Gallagher (Ref 27) to include temperature dependence by multiplying Eq. 17 by the Boltzmann distribution of kinetic energies to give

$$\frac{dI}{I_{total}} = N\ 4\pi c R^2(\nu)dR[4\beta(E - V(R))/\pi]^{1/2}\exp[-\beta(E - V(\infty))]d\beta E \qquad (18)$$

where $\beta = 1/KT$. This is the distribution of perturbers at $R(\nu)$ to $R(\nu)$ + dR with energy E to E + dE. It can be written $N\ 4\pi c R^2 dP_F dR$ where dP_F is $[4\beta(E-V(R))/\pi]^{1/2}\exp[-\beta(E-V(\infty)]d\beta E$. The expression $4\pi R^2 dR dP_F$ is the

canonical distribution $d^3pd^3Re^{-\beta E}$ which, when integrated over momentum space, gives the particle distribution in configuration space. See Appendix A in Ref 27 for a much more complete description of this distribution and its uses. The integral of dP_F over energy ranges for both free and bound perturbers leads to the expression $\exp[-\beta(V(R)-V(\infty))]$ which is the equilibrium distribution of all perturbers. Clearly then, this approach is valid only when equilibrium conditions exist.

To obtain the final expression for the total emission intensity between ν and $\nu+ d\nu$, Eq. 18 is multiplied by $I_{total} = N^* A_m(\nu)h\nu$ where N^* is the number density of excited atoms (radiators); $h\nu$, the photon energy and $A_m(\nu)$, the molecular electronic transition rate. One gets, after the energy integration

$$I(\nu)d\nu = \frac{N^*N\ h\nu A_m(\nu)4\pi c[R(\nu)]^2 d\nu}{|d\nu/dR|} \exp[-\beta(V(R) - V(\infty))] \qquad (19)$$

In the fluorescence experiments that are discussed later, the value of N^* will not be known so it is convenient to normalize Eq. 19 to the total emission intensity per excited state atom. This total atomic emission is given by $I_o = N^* h\nu_o A_a(\nu_o)$ the emission at line center, where ν_o is the line center frequency and A_a is the atomic transition rate. This approximation of the total emission by that at line center will be shown to be valid in Chapter IV. Using the fact that $A(\nu) \propto \nu^3$ from the Einstein relations, and including the appropriate molecular and atomic statistical weights g_m and g_a, Eq. 1 is obtained for the normalized emission intensity per wavenumber. This equation has been used successfully in the examination of alkali-inert gas fluorescence and proved a valuable tool for developing potential curves (Refs 14, 15, 27). In this work, the

normalized emission intensity, I/I_0, will be measured under a variety of conditions, as will the absorption coefficient. The equation for the absorption coefficient, along with an expression for the stimulated emission coefficient in terms of I/I_0, will be derived. But, first, a brief discussion of the limitations of the CFCP theory will be presented.

Limitations of the CFCP Theory

The CFCP theory, as developed in the previous section, has several approximations that could limit its use. The first approximation is the use of the WKB wavefunctions in the solution of Schroedinger's radial equation. The restriction here is that the momentum must be reasonably constant over several wavelengths. This approximation should hold for heavy perturbers like Xe or Cs, but will not be valid for light atoms like He (Ref 10). Experimental evidence supporting the validity for heavy atoms will be discussed shortly.

The others were the stationary-phase and random-phase approximations. The stationary-phase approximation neglects the nuclear motion. The primary effect of this is in the far red wings of the spectrum. The random-phase approximation smooths out any vibrational structure. This is certainly valid for the free-free transitions that were initially considered by Jablonski. However, the approach should also be valid for bound-free and bound-bound transitions where the vibrational structure does not dominate the spectrum.

Work on the alkali-noble gas molecules (Ref 7, 15, 27) shows that the CFCP does give a good prediction of the observed spectra for most bound-free transitions. For example, using the emission spectra and the CFCP theory, i.e. Eq. 1, potential energy curves have been developed for

Cs-noble gas molecules (Ref 27), and Rb-noble gas molecules (Ref 15). These potentials were then used in a fully quantum-mechanical calculation of the spectra and the agreement was very good for Ar and Xe (Ref 7). The only major discrepancy was for the alkali-Helium molecules (Ref 15). But that is to be expected because the WKB approximation does not hold for light perturbers. Because in this Cs_2 research the perturber was a heavy atom, Cs, the WKB approximation should be valid.

The other discrepancies noted in the CsXe (Ref 7) and RbXe (Ref 15) emission experiments were small oscillations about the continuum spectrum and failure of the red wing to drop off as fast as it should according to the CFCP. The quantum oscillations result from the fact that there really are discrete vibrational levels in the upper state, so the random phase approximation breaks down slightly; the oscillations were less than 15% on top of a smooth continuum spectrum. For bound-bound transitions, such as in Cs_2, the oscillation could be greater. The vibrational spacing in Cs_2 is only about 42 cm^{-1}, so even at room temperature, several vibrational levels will be populated at the same time. The rotational spacing is quite small so even weak pressure broadening will cause the rotational lines to overlap. Therefore, it is expected that the vibrational structure in Cs_2 will not be strong enough to invalidate the CFCP approach for calculating the average spectrum.

The second failure of the CFCP theory in the alkali-inert gas molecules was the failure of the intensity far out on the red wings to drop off as rapidly as the CFCP theory predicts. This is attributed to a breakdown in the stationary phase approximation. In any region of the spectrum where the intensity is changing rapidly with frequency, the nuclear motions cannot be neglected. The motion spreads the emission

into regions not predicted by Eq. 1. This motional broadening effect is expected in Cs_2 also. By analogy with the other alkalis, the upper state of Cs_2 could be shifted to longer radii than the ground state (Ref 66). This produces a broad red wing and the point of closest approach of the two potentials should denote the long wavelength cutoff in the spectrum. In fact, Eq. 1 predicts a singularity in the spectral intensity at that point because the potentials are parallel and $\left|\frac{d\nu}{dR}\right| \rightarrow 0$. Furthermore, the equation predicts no intensity at longer wavelengths. What is observed in Na_2 (Ref 66) and is expected to occur in Cs_2, is that the nuclear motion will spread out the intensity into a broad peak known as the quasi-static satellite. The intensity beyond that point will fall off exponentially. This is the only breakdown of the stationary phase approximation that is expected and it does not invalidate the use of the CFCP theory.

In summary, then, for these two sections, the equation for the normalized emission intensity has been developed based on the quasi-static theory of line broadening. This theory has been shown to be equivalent to the CFCP applied to molecular theory. This equation has been given a firm quantum-mechanical foundation by Jablonski (Ref 32) and has been verified experimentally by HDG (Ref 27) for most regions of the alkali-inert gas spectra. It is expected that it can also be used for Cs_2 spectra, if one averages through the vibrational structure. The next section will describe how to obtain expressions for absorption and stimulated emission coefficients and, then, how to interpret the data to determine the molecular potentials.

Absorption and Stimulated Emission Coefficients

The first step in the determination of whether Cs_2 has potential as a high power laser was to assess the possibility of gain in the medium. The information available prior to this research consisted of some preliminary absorption and discharge spectroscopy (Refs 4, 58) and some detailed studies of other alkalis, primarily Na_2 (Ref 65) and Rb_2 (Ref 16). None of this information was sufficient to specify the gain quantitatively in Cs_2. The $A^1\Sigma$ potential curve of the other alkali dimers, such as Na_2 was shifted to longer radii than the $X^1\Sigma$. In theory, this meant that gain could be achieved with fractional molecular inversions of about 5% in the Na_2 system for example (Ref 66). This same shift was expected in Cs_2 thus indicating that the molecule might exhibit gain for a reasonable inversion.

There were two methods of determining the gain. They were to perform either a direct gain measurement at 1.2 microns or to do both absorption and fluorescence spectroscopy and calculate the expected gain from those measurements. The former approach probably would have demonstrated only that gain could or could not be achieved under some particular operating conditions. As will be seen, the spectroscopy would allow determination of the pctential energy curves so that gain could be calculated under any set of conditions. Furthermore, some of the most important kinetic processes might be quantified, such as the formation and quenching rates described in the Introduction. The latter approach appeared to be more reasonable and to give much more of the needed information, so it was pursued. The next step, then, is to derive expressions for both the absorption and stimulated emission coefficients from the CFCP theory.

The expression for the absorption coefficient $\alpha(\nu)$, is obtained by performing the energy integration on Eq. 18 as before and multiplying by I_{total}. In absorption, $I_{total} = I(x=0)\Delta x N B(\nu) h\nu$. In this expression N is the atomic ground state density, $B(\nu)$ is the Einstein absorption probability coefficient and Δx is the distance in the medium. $B(\nu)$ is related to $A(\nu)$ by (Ref 29)

$$B(\nu) = \frac{c^2}{8\pi h\nu^3} A(\nu) \tag{20}$$

After including the statistical weights for the states and using $A(\nu) = (\nu/\nu_o)^3 A(\nu_o)$ as before, the absorption coefficient is given by

$$\alpha(\nu) = \frac{g_m}{g_a} \frac{\lambda^2}{2} \left(\frac{\nu}{\nu_o}\right)^3 A_m(\nu_o)\, N^2 R^2 \left|\frac{d\nu}{dR}\right|^{-1} \exp[-\beta(V_1(R) - V_1(\infty))] \tag{21}$$

The $V_1(R)$ is the lower state potential. The molecular electronic transition rate $A_m(\nu_o) = 1/\tau_m^o$ is the molecular lifetime at frequency ν_o. The relationship of τ_m^o to τ_a(the atomic lifetime) will be discussed in the Chapter IV. For absorption experiments in Cs_2, N will be the ground atomic state Cs density, [Cs], which can be determined from the gas temperature.

Equation 21 is the basis for the analysis of the absorption data. For several wavelengths, a plot is made of $\ln[\alpha(\nu)/N^2]$ versus 1/T and the slope is $V_1(\infty) - V_1(R)$. The ground state of Cs_2 is determined by the Rydberg-Klein-Rees method (Ref 54) using the vibrational constants obtained by Kusch and Hessel (Ref 37). From $V_1(\infty) - V_1(R)$, the radial position of each absorption wavelength (or frequency) can be determined. Next the several $\nu(R)$'s are plotted and a smooth curve drawn through

them. This curve will have a minimum at the quasi-static satellite. Since $d\nu/dR$ can be determined at any point on the $\nu(R)$ curve, all the parameters in Eq. 21 are known and the absorption spectrum can be calculated. Because there is some error associated with $\nu(R)$, from the error in $V_1(\infty) - V_1(R)$, several iterations of the $\nu(R)$ curve may be required to obtain the best fit to $\alpha(\nu)$. Once $\nu(R)$ has been finalized, $V_u(R)$ is calculated by adding $\nu(R)$ and $V_1(R)$. Once $V_u(R)$ is determined, other parameters such as the normalized emission or the stimulated emission coefficient can be calculated and compared with that measured experimentally.

The stimulated emission coefficient is written $g_s(\nu) = \lambda^2 I(\nu)/8\pi h\nu$ (Ref 44). If this is multiplied by $N^* h\nu A_a(\nu_o)/I_o = 1$, $g_s(\nu)$ can be written as

$$g_s(\nu) = \frac{\lambda_o^2}{8\pi c} \frac{N^*}{\tau_a} \left(\frac{\lambda}{\lambda_o}\right)^3 \left[\frac{I(\nu)}{I_o}\right] \tag{22}$$

The quantity in brackets is that which will be measured in the fluorescence experiments. So one can compare the experimental gain with that determined from using the potentials to calculate $I(\nu)/I_o$ via Eq. 1. This comparison should be indicative of whether the molecule is behaving as expected or are there some loss mechanisms that must be understood.

Although it was not possible to predict the molecular inversion required for net gain, it is possible to estimate the atomic inversion criterion. Using the equations for stimulated emission and absorption and solving for $\alpha(\nu)/g_s(\nu) = 1$, the atomic inversion criterion becomes

$$\frac{[Cs^*]}{[Cs]} = \frac{g^*}{g} \exp[\, h(\nu - \nu_o)] \tag{23}$$

where $\nu_o = [V_u(\infty) - V_l(\infty)]/h$ and $\nu(R) = [V_u(R) - V_l(R)]/h$. For the 6S and 6P states in Cs, the ratio of the atomic statistical weights is $g^*/g = 3$ and ν_o is the frequency corresponding to 0.8944 microns. At 346°C, net gain should be achievable at a fractional atomic inversion of 0.0025. This looks very attractive; however, it applies only when the excited atoms and molecules are in equilibrium and there are no significant losses. It does provide a starting point, and the absorption/emission spectroscopy will be used to obtain a better value.

Laser Kinetics

In the next two sections, discussions of the kinetics processes that may be important in the Cs_2 system will be presented. This will include electron, atomic, and molecular kinetics processes. The mechanisms that were expected to be the most important are discussed in detail. The others are briefly mentioned along with the reasons they were considered less significant. The electron kinetics will be discussed first because it was the highly efficient electronic pumping of the atomic Cs that helped make Cs_2 appear to be a good candidate for an electric discharge laser. They will be analyzed using Boltzmann transport theory. These electron processes would be important in an actual Cs/Xe discharge, but not in the fluorescence experiment. Therefore, there was no experimental verification of these rates and efficiencies in this research. (See Appendix A for comparison with other experiments). The second set of processes to be considered in these sections are the gas kinetics (atomic and molecular). These mechanisms would occur in a discharge as well as in the fluorescence experiments. In fact, the rates for the important atomic and molecular processes were obtained from the analyses of the

fluorescence data. First, most of these processes are discussed and estimates made for the expected rates of the most important ones. Secondly, the derivation of the actual rates from the fluorescence experiments will be described. Summary charts for both the electron and gas kinetics are included.

Electron Kinetics

The electronic processes that are of interest in a high pressure Cs/inert gas discharge are momentum-transfer, excitation, ionization, and quenching. A list of all the pertinent inelastic processes is presented in Table I. Of the processes mentioned in Table I, the excitation to the 6P level and the quenching of the $A^1\Sigma + a^3\pi$ molecular states are probably the most important. No data on electron quenching of Cs_2^* was available and therefore, this process was not included in the basic analysis. Later, quenching by inert gas atoms is discussed and will be seen to be quite significant, but this was not known apriori. The target particle in these processes can be either an atom or a molecule. The analysis of the electron kinetics, however, will consider only atomic processes because the molecular densities are less than 1% of the atomic densities at the temperatures of interest.

The method of analysis was to solve the Boltzmann transport equation for a steady-state, homogeneous, isotropic gas of total density N, and obtain the electron velocity distribution, f(v). E/N is the electric field divided by the total density. From this, one calculates all of the important rate constants and the power transfer into each of the processes. The method of doing this and the pertinent equations, are described in Appendix A. A Maxwellian distribution for f(v) could have

Table I

Inelastic Electron Processes in $Cs/Cs_2/Xe$

Excitation

$Cs(6S) + e^- \rightarrow Cs^*(6P) + e^-$	Pumping of 6P state
$Cs(6S) + e^- \rightarrow Cs^{**} + e^-$	Excitation of other levels
$Cs^*(6P) + e^- \rightarrow Cs^{**} + e^-$	Excitation loss from 6P
$Cs_2(X^1\Sigma) + e^- \rightarrow Cs_2^*(A^1\Sigma + a^3\pi) + e^-$	Molecular Excitation
$Xe + e^- \rightarrow Xe^* + e^-$	

Ionization

$$Cs(6S) + e^- \rightarrow Cs^+ + 2e^-$$

$$Xe + e^- \rightarrow Xe^+ + 2e^-$$

Quenching

$Cs^*(6P) + e^- \rightarrow Cs(6S) + e^-$ ($\Delta KE > 0$)	Superelastic
$Cs_2^*(A^1\Sigma + a^3\pi) + e^- \rightarrow Cs_2(x^3\Sigma) + e^-$	Molecular Quenching

Note: Cs^{**} is any excited level that lies above the 6P state

been assumed; however, as can be seen from Fig. 2, the distribution actually obtained from the analysis was quite different. The additional electrons at low energies in a Maxwellian distribution relative to the actual distribution could have given very different answers. Furthermore, the computer method of solving the Boltzmann equation had been well validated (Ref 57).

In order to explore the electron discharge kinetics, one must first define the gas mixture. The basic mixture used in this analysis consisted of ground state Cs and Xe atoms in a ratio of 1 to 10^4 at a temperature of 550°K. Xenon was chosen because it is the most polarizable of the inert gases. These conditions are representative of the approximate range where such a discharge laser might be operated and so are used as an illustrative example. In an equilibrium vapor at this temperature, Cs has a vapor pressure of 1.0 torr so the corresponding Xe pressure is 13 atmospheres. The basic mixture in the analysis contained no Cs_2 molecules for the reason already stated. Furthermore, the primary effect would probably be the pumping of ground state molecules to the excited state. The net result would be to increase the number of Cs_2^* molecules and, therefore, the overall efficiency. Even without their inclusion, the electronic pumping efficiency will be seen to be quite high. Therefore, all the electron-molecule processes have been excluded.

Next, one must decide which inelastic processes should be included in the analysis. Ionization of both atomic species and electronic excitation of the Xe will, of course, be included. The excitation (pumping) of Cs 6S atoms to the 6P state (rate P' in Fig. 1) and the reverse process (the superelastic rate Q') must also be considered. They are

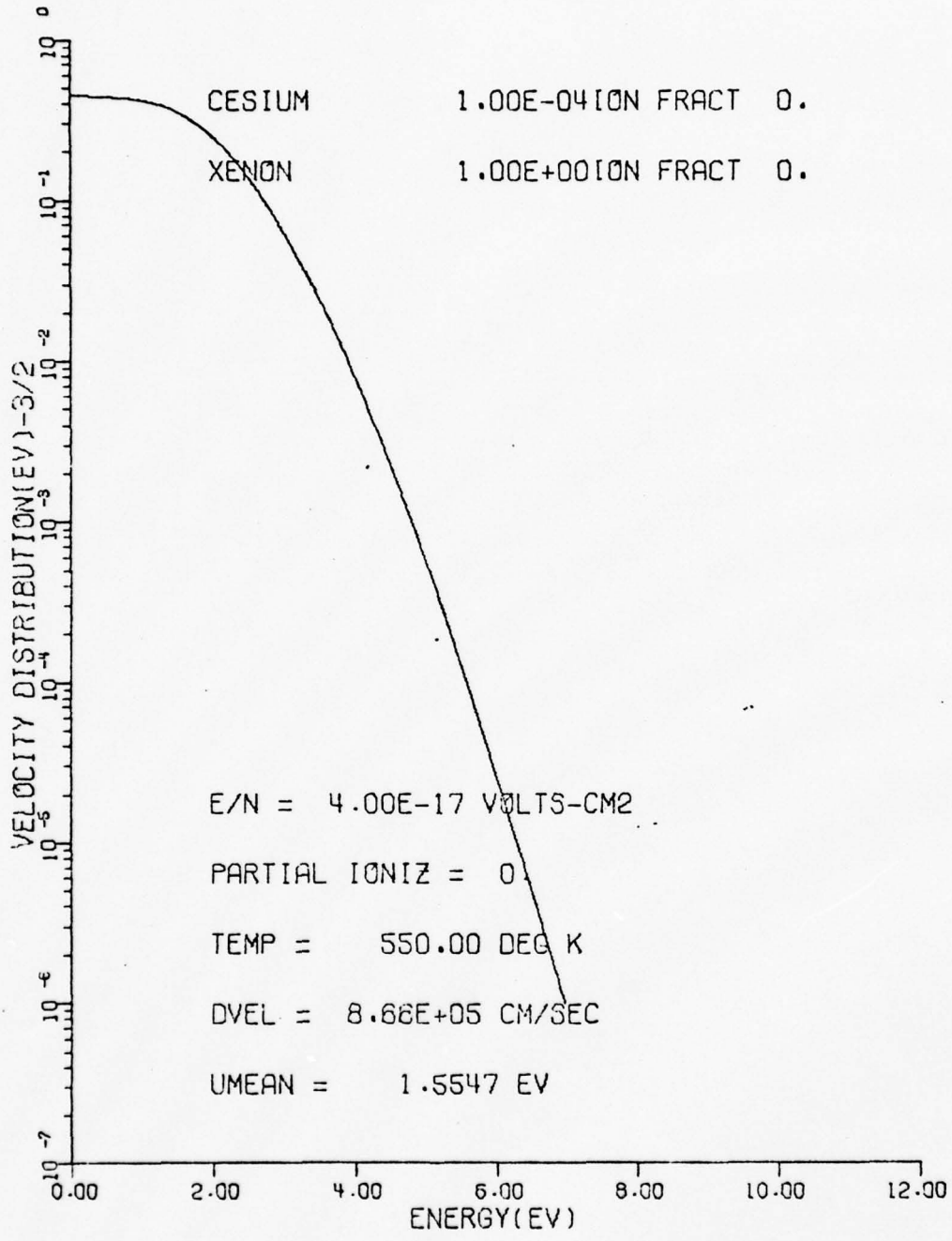

Fig 2 Electron Velocity Distribution Function in Cs/Xe

included in the basic analysis. Additional processes that could be important are excitation of 6S and/or 6P atoms to higher lying levels in Cs. These will be additions to the basic analysis. Cross sections for all these processes are given in Appendix A.

First the efficiency of the 6S-6P pumping will be examined. Fig. 3 shows that it could be about 95%. The gas mixture was as described above with a fractional ionization of 10^{-6}. The important result is that the efficiency of energy transfer to the 6P state is greater than 90% over a wide range of E/N. This was expected because of the large Cs resonance cross sections (see Fig. A1 in Appendix A for specific cross sections used). The high efficiency does not change significantly as one varies the ratio between Cs and Xe. In fact, as the ratio of Cs to Xe increases, the range of E/N where high efficiencies are obtained, increases (see Fig. A7 in Appendix A).

The second product of the Boltzmann analysis (Appendix A) was the determination of the rate constants (ν/N), for each of the elastic, excitation and ionization processes. These constants are shown in Fig. 4 for the same mixture of Cs and Xe. The superelastic rate constant is not shown; however, it is approximately constant over the range of E/N of 10^{-17} to 10^{-16} at a value of 1.1×10^{-6} cm^3/sec. The rate constants also are not very sensitive to the Cs/Xe ratio or the temperature. From the rate constants, one can determine all the rates of interest. For example, with an electron density $N_e = 10^{14}$ cm^{-3}, the pumping rate, $P' = N_e(\nu/N)_{excit}$, is about 6×10^7/sec at $E/N = 10^{-16}$ volt-cm^2.

As already mentioned, the initial Boltzmann analysis described above left out several processes that must be considered. First is the electron pumping of ground state Cs atoms to atomic levels higher

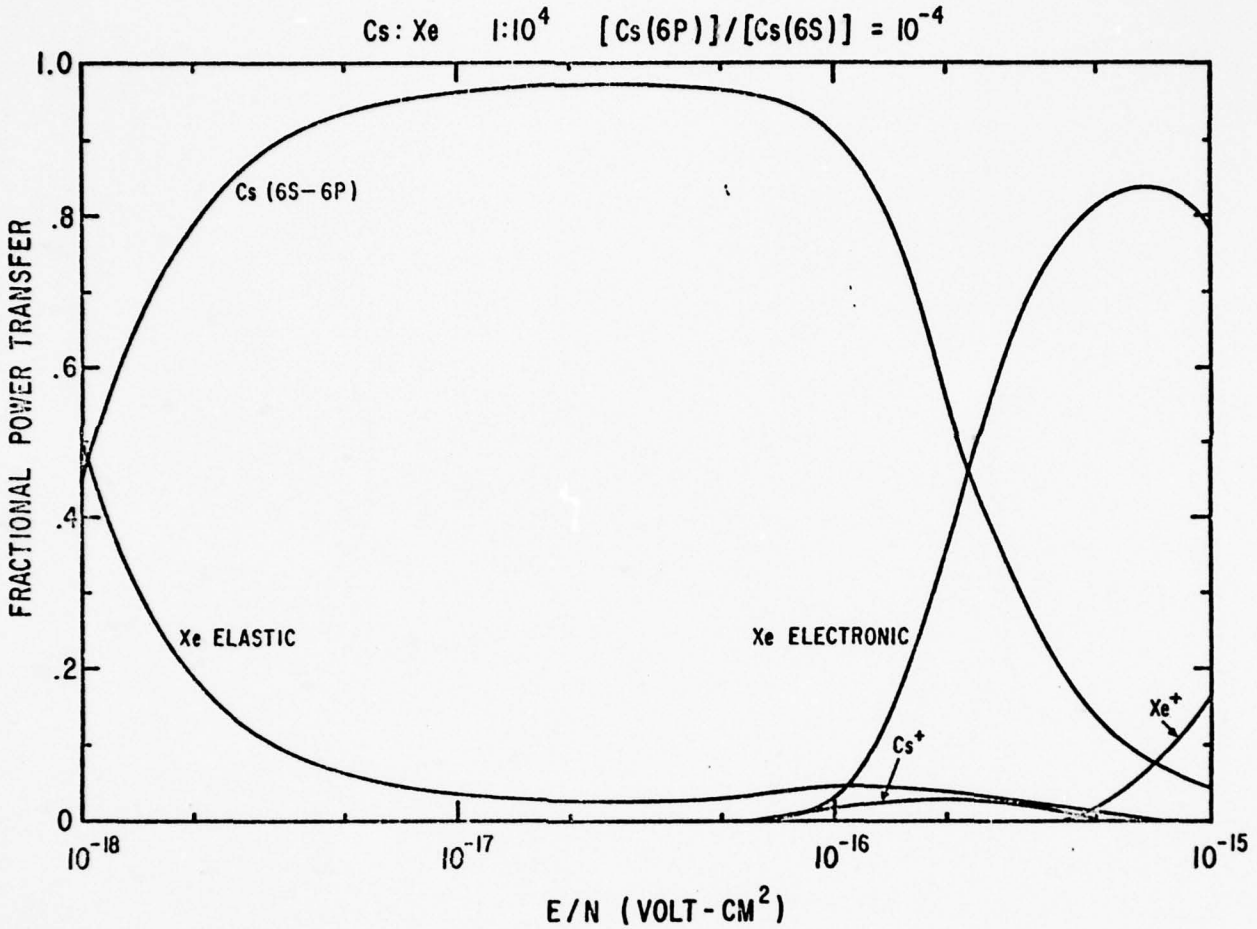

Fig 3 Pumping Efficiency in a Cs/Xe Discharge

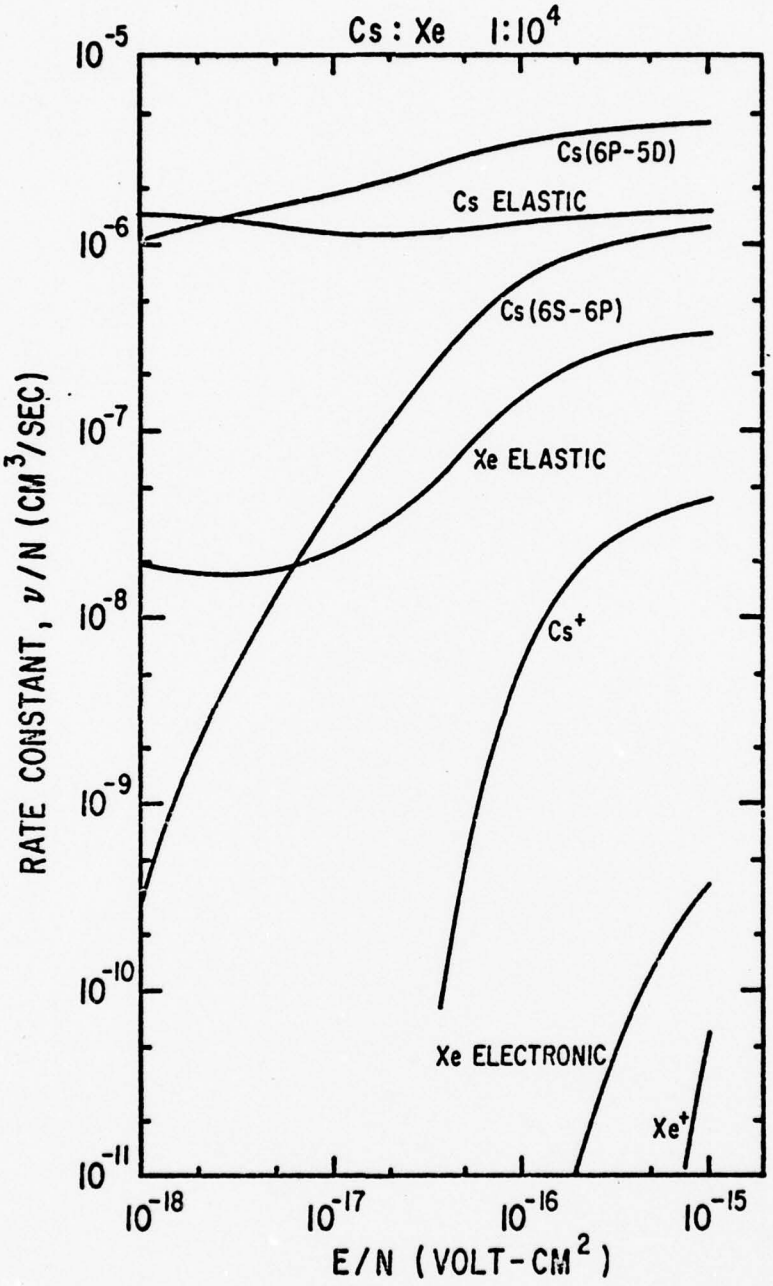

Fig 4 Electron Rate Constants in a Cs/Xe Discharge

than the 6P, for example to the 5D, 7S, etc. Very little information exists on the cross sections for these transitions. The maximum cross section found in the literature was 4 $\mathring{A}^2$ for the 6S-5D transition (Refs 13, 20). This is down by a factor of 30 from the peak resonance cross section (see Fig. A1), and so excitations to higher levels from the ground state is not expected to be significant. The second, and perhaps more important, process is excitation of the $Cs^*(6P)$ atoms to higher levels, especially when a significant fractional population inversion is achieved. Early rough estimates indicated that the ratio of excited to ground state atoms might be in the range of 0.001 to 0.01 for net gain, depending on the temperature. Since the next higher lying level, the 5D, is only 0.4 eV above the 6P, significant losses in the excited population might occur. In the literature, estimates were given only for an "effective" peak cross section of 350 $\mathring{A}^2$ (Ref 13), so the Impact Parameter method (Ref 58) was used to approximate the cross sections as a function of energy (see Appendix A for details). The peak values of these theoretical cross sections agreed with those determined experimentally (Ref 13) to within 15% for the 6P - 5D transition. The cross sections were quite large, 400 $\mathring{A}^2$ for the 6P - 5D transition; however, the two step excitation did not seriously reduce the high efficiency of transferring power to the 6P level, even for fractional inversions of 0.01 (see Fig. A6). However, at a 5% inversion, the peak efficiency is reduced below 80%. The net result of introducing these two perturbations to the original analysis is to change the answer by less than 10%. The original conclusion of high efficiency appears to still be true.

There is one more electron process that has not been mentioned and that is excitation transfer, either between the resonance doublet ($6^2P_{1/2} \leftrightarrow 6^2P_{3/2}$) or between the $A^1\Sigma \leftrightarrow a^3\pi$ potentials. In a discharge it is expected that these pairs will be strongly coupled because of spin exchange collisions (Ref 66). For example, the spin exchange cross sections in Cs ($6^2P_{1/2} \leftrightarrow 6^2P_{3/2}$) are about 2×10^{-14} cm^2 (Ref 12) which gives a rate constant of about 3×10^{-7} cm^3/sec in a discharge, comparable to the excitation rate constant. The rate between the $A^1\Sigma$ and the $a^3\pi$ should be even faster because the energy defect is smaller. In any case, the rates are fast enough to ensure an equilibrium ratio between the respective states.

This concludes the discussion of the electron kinetics pertinent to the proposed Cs_2 electric discharge laser. The principle conclusions are that the electronic pumping should be quite efficient and there does not appear to be any major loss mechanism such as excitation to higher atomic levels.

Gas Kinetics (Atomic and Molecular)

The processes to be considered in this section are of interest to both the postulated Cs_2 laser discharge and the optical emission experiment that was carried out as part of this work. In fact, that experiment was performed to elucidate some of the most important kinetic rates. The gas kinetics can be separated into four general categories: 1) excitation transfer, 2) radiation, 3) molecular formation and dissociation, and 4) intermolecular transitions. The principle atomic states are the Cs $6^2S_{1/2}$, $6^2P_{1/2}$ and $6^2P_{3/2}$ and the primary molecules are the $Cs_2(X^1\Sigma, x^3\Sigma, A^1\Sigma, a^3\pi, B^1\pi)$ and $CsXe(X^2\Sigma_{1/2}, A^2\pi_{1/2}, A^2\pi_{3/2})$. A

summary chart of all the processes mentioned in this section is given in Table II. Preliminary estimates, where available, of the more important rate constants are also listed there. Each of the general categories of processes will be discussed and the equations that describe the steady-state kinetics will be derived. Finally, both the theoretical and experimental determination of some of the important rates will be discussed.

The first process is excitation transfer between the first two excited states of Cs, the resonance doublet. The excitation transfer can occur due to collisions either with Cs or Xe atoms. For Cs atoms, the cross sections are about 6×10^{-16} cm^2 for $P_{1/2} \rightarrow P_{3/2}$ and about 3.1×10^{-15} cm^2 for the reverse process (Ref 36). Using Xe for the transfer reduces the cross sections to 7.2×10^{-21} cm^2 and 2.7×10^{-19} cm^2 respectively (Ref 36). For the operating parameters of the fluorescence experiment. $[Xe] = 6 \times 10^{19}$ cm^{-3} and $[Cs] = 5 \times 10^{16}$ cm^{-3} only the Cs induced excitation transfer will be significant and the rate will be roughly 10^6--10^7 sec^{-1}.

The second type of process of interest in both the Cs/Xe fluorescence experiment and the laser is radiation by excited atoms or molecules. The Xe atoms will all be in the ground state and do not contribute. The Cs atomic fluorescence should be relatively weak because at one torr of Cs, the resonance lines will be optically trapped. The natural lifetime of Cs is about 30 nsec (Ref 41) for either 6P state. But with trapping, the actual lifetime, $1/\Gamma_1$, will probably be increased by a factor of 10 or more, in the fluorescence experiment. In a long discharge laser at these pressures, the resonance lines would have much longer lifetimes and would be, in a sense, metastable states.

Table II

Atomic and Molecular Processes in $Cs/Cs_2/Xe$

Excitation Transfer	Forward-Reverse Constants
$Cs^*(6^2P_{1/2}) + Cs \rightleftarrows Cs^*(6^2P_{3/2}) + Cs$	2×10^{-11}-1×10^{-10} cm^3/sec(Ref 36)
$Cs^*(6^2P_{1/2}) + Xe \rightleftarrows Cs^*(6^2P_{3/2}) + Xe$	2×10^{-16}-10^{-14} cm^3/sec (Ref 36)

Radiation	Rate
$Cs^*(6^2P_{1/2}) \rightarrow Cs(6^2S_{1/2}) + h\nu$	2.9×10^7/sec (Ref 41)
$Cs^*(6^2P_{3/2}) \rightarrow Cs(6^2S_{1/2}) + h\nu$	3.3×10^7/sec (Ref 41)
$Cs_2^*(A^1\Sigma) \rightarrow Cs_2(X^1\Sigma) + h\nu$	4×10^7/sec
$CsXe^*(A^2\pi) \rightarrow CsXe(X^2\Sigma) + h\nu$	3×10^7/sec (Ref 27)

Molecular Formation ($k_f \rightarrow$, $k_d \leftarrow$)	Rate Constant
$Cs^*(6P)+Cs+Cs \rightleftarrows Cs_2^*(A^1\Sigma+a^3\pi) + Cs$	
$Cs^*(6P)+Cs+Xe \rightleftarrows Cs_2^*(A^1\Sigma+a^3\pi) + Xe$	$k_f \simeq 4$-5×10^{-30} cm^6/sec (Ref 66)
$Cs^*(6^2P_{3/2})+Cs+Xe \rightleftarrows Cs_2^*(B^1\pi) + Xe$	
$Cs^*(6^2P_{1/2})+Xe+Xe \rightleftarrows CsXe^*(A^2\pi_{1/2}) + Xe$	$k_f = 8.2\times10^{-32}$ cm^6/sec (Ref 27)
	$k_d = 2.4\times10^{-11}$ cm^3/sec (Ref 27)
$Cs^*(6^2P_{3/2})+Xe+Xe \rightleftarrows CsXe^*(A^2\pi_{3/2}) + Xe$	

Intermolecular Transfer	
$Cs_2^*(A^1\Sigma) \rightleftarrows Cs_2^*(a^3\pi)$	
$Cs_2^*(B^1\pi) + Xe \rightarrow Cs_2^*(A^1\Sigma) + Xe$	
$Cs_2^*(a^3\pi) + Xe \rightarrow Cs_2^*(x^3\Sigma) + Xe$	Quenching
$Cs_2^*(a^3\pi) \rightarrow Cs_2^*(x^3\Sigma)$	Predissociation

Precise determination of Γ_1 depends on the specific geometry. In any case, these atomic decay rates will be relatively slow and, therefore, not too important. Actually, it is the fact that the effective atomic lifetime is long that allows time for the atoms to form the molecules necessary for lasing.

The molecular radiative rates, such as Γ_2 in Fig. 1, are of some interest and can be estimated from the relation $A(\nu)=(\nu/\nu_o)^3 A(\nu_o)$ as already mentioned. $A(\nu)$ is the transition probability per sec for an untrapped transition. The use of $\Gamma(\nu)$ denotes the actual radiative rate which may include some trapping. For an optically thin vapor $\Gamma(\nu)=A(\nu)$. So the molecular radiative rates at any frequency can be referred to the rate at the atomic line center as has commonly been done (Ref 27). Some data is available which indicates that $A_m(\nu_o)$ is about twice $A_a(\nu_o)$ and this will be reviewed in the data analysis sections. Therefore, estimates of these rates are available for any of the allowed transitions. The $a^3\pi$ - $X^1\Sigma$ transition is normally forbidden by spin conservation.

The third category of gas kinetic rates are those of molecular formation and dissociation referred to as R_f and R_d in Fig. 1. The data required are the formation and dissociation rate constants which, for the process $Cs^* + Cs + Xe \rightarrow Cs_2^* + Xe$, are defined by $k_f = R_f/[Xe][Cs]$ and $k_d = R_d/[Xe]$. The formation rate of $Cs_2^*(A^1\Sigma + a^3\pi)$ is one of the most critical kinetic parameters in the laser operation. Prior to this research, there was no data in Cs on which to base an estimate of k_f for the excited state formation. In Ref. 66, York and Gallagher made estimates of k_f with Xe for Na_2^* of 8×10^{-30} cm^6/sec, based on scaling known rate constants of other molecules. Subsequent discharge experiments have shown that rate actually to be 10^{-29} cm^6/sec

(Ref 23). By way of comparison, the formation rate for the process $Cs + Cs + Cs \rightarrow Cs_2 + Cs$ has been estimated from experiment to be about 3×10^{-30} cm^6/sec at 600°K (Ref 24). Since the upper state of Cs_2 is deeper and longer range, it is not unreasonable to expect that the k_f for Cs_2^* might be larger. There is, of course, a dependence of k_f on the polarizability of the third body. The polarizabilities are about 6.3×10^{-23} cm^3 for Cs (Ref 26) and about 4×10^{-24} cm^3 for Xe (Ref 11) so the rate constant for Xe is expected to be smaller than for Cs. There was no conclusive way to predict a specific value, therefore, the preliminary estimate of the Cs_2^* formation rate was made following the arguments of York and Gallagher. They proposed that the ratio of k_f/Γ_2 should be about the same in all the alkali dimers. This leads to an estimate of about $4\text{-}5 \times 10^{-30}$ cm^6/sec for k_f in Cs_2^*. The corresponding dissociation rate constant should be fairly small because the potential wells for $Cs_2^*(A^1\Sigma + a^3\pi)$ are deep, probably more than 5000 cm^{-1} (Ref 66).

Molecular formation into Cs_2^* states other than the $A^1\Sigma + a^3\pi$ from the 6P can be expected since the 6P splits into eight separate states (not counting degeneracies) (Ref 45). By analogy with Li_2, only two of these may be significant, the $B^1\pi_u$ and $b^3\Sigma_g^+$. The others are expected to be repulsive (Ref 66). Nothing is known of the $b^3\Sigma$ in any of the alkalis other than Li_2; however, the $X^1\Sigma$ - $B^1\pi$ transition has been examined photographically in Cs_2 (Ref 38) so some information was available. The formation rate into the $B^1\pi$ should be much lower than for the $A^1\Sigma$ because the potential is only 2200 cm^{-1} deep (Ref 38) compared with an estimated 5-6000 cm^{-1} for the $A^1\Sigma$. The range of the potentials should be about the same. Since the formation rate will be considerably smaller, the $B^1\pi$ state should not drain many of the 6P

atoms that could otherwise form into the $A^1\Sigma$ and $a^3\pi$ states.

There is also molecular formation into the CsXe excited potentials $A^2\pi_{1/2}$ and $A^2\pi_{3/2}$. The $CsXe^*(B^2\Sigma_{1/2})$ should be of no concern because it is repulsive (see Fig. 11 in Chap. III). Although the formation rate constants for $CsXe^*$ have not been measured, those of $RbXe^*$ have. The value for the $A^2\pi_{1/2}$ state was 8.2×10^{-32} cm^6/sec (Ref 8). The $CsXe^*(A^2\pi_{1/2})$ is somewhat shallower but longer range (Ref 27), so the value for RbXe is probably a reasonable estimate for CsXe. The corresponding value of k_d in RbXe is 2.4×10^{-11} cm^3/sec (Ref 8). Since the actual formation rate in CsXe depends on $[Xe]^2$ rather than [Xe][Cs], it is possible that at high Xe densities the excited CsXe potentials will soak up some of the Cs^* atoms. These rates should be considered in the kinetics equations that describe the behavior of $[Cs^*]$.

The final category of processes to be considered are those that involve transfer between molecular states. Here one is concerned primarily with transfer between the $a^3\pi$ and $A^1\Sigma$ states and between the $a^3\pi$ and $x^3\Sigma$ states of Cs_2. Collisionless transitions between the CsXe and Cs_2 states are strictly forbidden because the rotational angular momentum (J) must change by 0 or ± 1 and the molecules have half-integer and integer J values respectively. Collisions may occur which would transfer CsXe molecules into the $B^1\pi$ state of Cs_2. It is possible, however, to get collisionless transfer between the $B^1\pi$ and $A^1\Sigma$, especially if these states approach each other in the attractive region of the $B^1\pi$. York and Gallagher have estimated the rate constant to be about 2.5×10^{-12} cm^3/sec in Na_2 (Ref 66). This would be beneficial to populating the $A^1\Sigma$ state.

Up to this point, the $A^1\Sigma + a^3\pi$ combination has been considered as a single state. To continue to do this requires that they be closely coupled by collisions. The assumption is made that this is true in a discharge by means of electron spin exchange collisions (Ref 66). In the optical emission experiment, the coupling depends on the collisions by Xe to induce the transfer, and there are no data on these cross sections. In addition, by analogy with Na_2, the two states may actually overlap or cross (Ref 2). So the separation between electronic states becomes very indistinct and the effective transfer rate may be quite large. For this reason, the $A^1\Sigma$ and $a^3\pi$ states will be assumed to be closely coupled and can be treated as a single state, at least for the preliminary kinetics equations.

The final intermolecular process involves the possible transfer of molecules from the $a^3\pi$ to the $x^3\Sigma$ repulsive state. This transfer can occur either by predissociation when the potential curves cross, or by collisional quenching by a third body at a point where the molecular potential curves are very close. The occurence of either one of these processes at a point deep in the $a^3\pi$ potential well will likely be detrimental to the concept of a Cs_2 laser. Most of the Cs_2^* would go rapidly to the $x^3\Sigma$ state and then dissociate into ground state atoms with large kinetic energies, thereby heating the gas. York and Gallagher predict that this does not occur, at least not in Na_2 (Ref 66), and so far there has been no substantial analysis of what these rates might be. The transition is allowed by all the selection rules (Ref 29) and, so, if it occurs, it should be fast. Rates of about 10^{12}/sec might be expected for predissociation (a vibrational period) and maybe as high as 10^{10}/sec for quenching, based on hard sphere cross sections and a Xe density of

5×10^{19} cm^{-3}. These processes must very definitely be considered and the fluorescence data should indicate whether or not they occur.

At this point, only the processes shown in Fig. 1 remain, that is formation and dissociation of the $Cs_2^*(A^1\Sigma + a^3\pi)$ state, radiation from the Cs_2^* and quenching or predissociation to the $x^3\Sigma$ state. The rate equation for $[Cs_2^*]$ can be written as follows:

$$\frac{d[Cs_2^*]}{dt} = R_f[Cs^*] - R_d[Cs_2^*] - R_q[Cs_2^*] - R_p[Cs_2^*] - \Gamma_2[Cs_2^*] \qquad (24)$$

where the transfer from the $B^1\pi$ state as well as any collisional transfer from the CsXe states have been neglected. Solving Eq. 24 for steady-state conditions and using the rate constants, gives

$$\frac{[Cs_2^*]}{[Cs^*]} = \frac{k_f[Cs][Xe]}{\Gamma_2 + k_p + [Xe](k_q + k_d)} \qquad (25)$$

where $k_p = R_p$ and $k_q = R_q[Xe]$ and are the rate constants for predissociation and quenching respectively. Equation 25 is the basic tool for determining the various kinetic rates in the fluorescence experiment.

There are two ways to obtain values of $[Cs_2^*]/[Cs^*]$, one theoretical and one experimental. The theoretical approach involves the equilibrium constant K_{eq} which, by the law of mass action (Ref 27) can be written

$$K_{eq} = \frac{[Cs_2^*]_e}{[Cs^*]_e[Cs]_e} = \frac{k_f}{k_d} \qquad (26)$$

for the process $Cs^* + Cs + M \rightarrow Cs_2^* + M$ where M is any third body and the subscript e denotes equilibrium concentrations. This defines the ratio between $[Cs_2^*]$ and $[Cs^*]$ when they are in chemical equilibrium, that is

when k_d dominates all other terms in the denominator of Eq. 25. The equilibrium constant can also be written in terms of the potential curves as (Ref 66)

$$K_{eq} = \frac{g_m}{g_a}\int_0^\infty d^3R e^{-\beta\Delta V(R)}\ P[3/2,-\beta\Delta V(R)] \qquad (27)$$

where $\Delta V(R) = V(R) - V(\infty)$ and $P[3/2,-\beta\Delta V(R)]$ is the normalized incomplete gamma function. The importance of K_{eq} is that for a known Cs density and temperature, the value of $[Cs_2^*]/[Cs^*]$ can be predicted once the potential curves have been determined from the absorption experiment.

One can also make a determination of that ratio by integrating the normalized Cs_2 emission spectrum (I/I_o) multiplied by $(\nu_o/\nu)^4$. This can be seen by writing Eq. 1 in terms of $[Cs_2^*]$ by use of Eq. 27 with $N = [Cs^*]$ so that

$$\frac{I}{I_o} = \left(\frac{\nu}{\nu_o}\right)^4 \frac{[Cs_2^*]}{[Cs^*]}\ \frac{A_m}{A_a}\ 4\pi cR^2\left|\frac{d\nu}{dR}\right|^{-1}\ \frac{e^{-\beta\Delta V}}{\int d^3R e^{-\beta\Delta V_P}} \qquad (28)$$

Integrating both sides over $d\nu$ (the right hand side integral becomes one over dR) one gets

$$\frac{A_a}{A_m}\int\left(\frac{\nu_o}{\nu}\right)^4 \frac{I(\nu)}{I_o}\,d\nu = \frac{[Cs_2^*]}{[Cs^*]} \qquad (29)$$

Since I/I_o is an experimental quantity determined from the fluorescence, one has a method to determine whether the excited molecules and atoms are in equilibrium and, if not, what might be the important loss rates. For example, if the $[Cs_2^*]/[Cs^*]$ ratio is much smaller than expected in equilibrium, then either Γ_2, k_p, or $k_q[Xe]$ are larger than $k_d[Xe]$ in the de-

nominator of Eq. 25. For either of the first two processes, $[Cs_2^*]/[Cs^*]$ will be [Xe] dependent and for the quenching, the ratio will be independent of the Xe density. Therefore, this particular formulation of the kinetics equation gives one a powerful tool for interpreting the fluorescence data.

The key processes in the Cs/Xe system can be summarized as follows. First the pumping efficiency (6S-6P) should be very high. The Boltzmann analysis confirms this as well as providing all the necessary rates involving electrons. The absorption experiment will help determine the potential curves and, therefore, the equilibrium constant. By integrating the normalized fluorescence spectrum, the ratio $[Cs_2^*]/[Cs^*]$ is obtained. This can be compared with that calculated from K_{eq} to determine whether the excited atoms and molecules are in chemical equilibrium. Using this information and the Xe density dependence of $[Cs_2^*]/[Cs^*]$, estimates of k_f and k_d can be made. And, if necessary, one can estimate the quenching rates and predissociation rates.

Chapter III. Experimental Description

Introduction

As previously stated, the purpose of the experiments was to measure the absorption coefficient and normalized emission intensity of Cs_2. Two separate experiments were performed to do this, and they are described in the second and fourth sections of this chapter. The data reduction necessary to determine the absorption coefficient was fairly straightforward and so is included in the experimental description. For the fluorescence experiment, the data reduction was more involved and is presented separately in the fifth section. Because the uncertainties in any experiment are very important, they are discussed in detail within both the absorption and fluorescence experimental description sections. In addition, the more important uncertainties are summarized in separate sections. Since some of the equipment and the cell preparation procedures were common to both experiments, they are enumerated for the absorption experiment only. A third experiment was performed in the course of this thesis, a heat pipe discharge experiment. Because it was not a primary contributor to the overall objective, it is included as Apendix C rather than in the main body of the thesis.

Absorption Experiment Description

The absorption experiment was the first experiment to be performed. A schematic diagram of the experimental layout is shown in Fig. 5. The 150 watt tungsten-halogen projector lamp (General Electric FCS) was powered by a current-regulated (0.1%) dc power supply. The spatially filtered and collimated light from the lamp passed through the pyrex

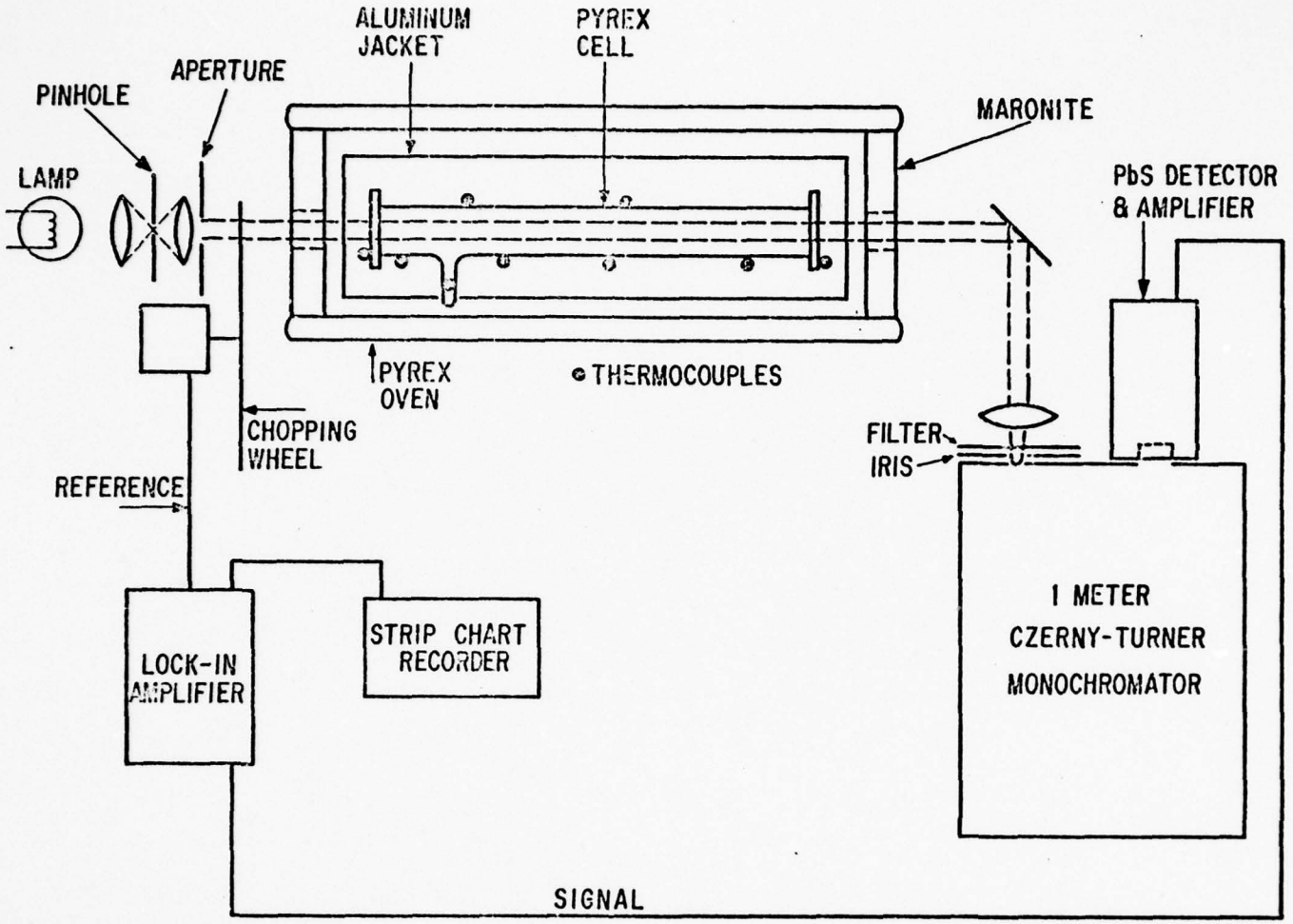

Fig 5 Schematic Diagram of the Absorption Experiment

absorption cell and was focused on the entrance slit of a one meter, Jarrell-Ash, Czerny-Turner scanning spectrometer. A 0.665 micron lower cutoff filter on the spectrometer entrance slit was used to exclude second and higher order spectra. The grating had 1180 lines/mm and a blaze wavelength of 0.75 microns. The dispersion at the exit slit was 8.2 Å/mm and, since the slit width was 1.0 mm, the resolution, for the absorption experiment, can be expressed as approximately 8.2 Å. Synchronous detection was performed at 375 Hz with a room temperature PbS detector and a PAR Model 122 lock-in amplifier. The scanning speed of the spectrometer was either 250 Å/min or 500 Å/min with a lock-in time constant of 1.0 or 0.3 sec respectively. The Santa Barbara Research Model 4598 PbS detector had an area of 0.16 cm^2 and a detectivity of 8.6×10^{10} $cmHz^{\frac{1}{2}}/watt$. A two-stage amplifier enhanced the signal from the detector to the lock-in amplifier. A Hewlett Packard Model 7051 strip chart recorder was used to record the data.

Absorption measurements were made on two different 12 mm diameter pyrex cells, 15.1 and 30.0 cm long. The Cs was 99.95% pure and was obtained from the Research Organic/Inorganic Chemical Co. The cells were cleaned with HCl, HNO_3, and acetone and baked out at about 350°C for at least four hours. The residual pressure was $2\text{-}4 \times 10^{-6}$ torr, and the outgassing was less than 2×10^{-6} torr when the cell was closed off for several hours. The Cs was added, after cleaning, by distillation. The basic geometry of all the cells was the same as the one shown in Fig. 5. The 0.125 in. thick pyrex windows were sealed onto the cell by melting the pyrex slightly at 810°C for five minutes and then allowing a slow cooling and annealing.

Originally, the experiment was set up using a stainless steel pipe with sapphire windows mounted into Varian flanges at the end of the pipe. When the first absorption experiments were conducted, a periodic undulation in the spectrum was observed. The location of these peaks changed with temperature. The pattern was eventually attributed to some type of interference effect in the sapphire window. It could be seen in a single window at any temperature. Because this backgound variation could not be tolerated, the absorption cell was changed to a pyrex tube with pyrex windows. Initial attempts were made to attach the pyrex windows via a ceramic seal. This technique failed also. Eventually the windows were fuse bonded onto the cell. This finally led to the method described above that was used for sealing all the absorption cells. The very slight curvature of the windows that resulted from the melting had no observable effect on the absorption measurements.

The oven shown in Fig. 5 consisted of a three-inch pyrex pipe with three independently controlled heating coils. The exterior of the oven was wrapped with asbestos tape for increased insulation. An aluminum jacket helped achieve fairly uniform temperatures over the cell ($\pm$ 2°C). The ends of the pyrex oven contained maronite plugs and separate heaters. These end heaters were used to maintain the windows at slightly higher ($\sim$10°C) temperatures than the cell body to prevent Cs condensation on the windows. The chromel-alumel thermocouples, which had been calibrated at 0°C and 100°C, were typically within $\pm$ 2°C of the average temperature on the cell body. There was no noticeable deterioration or discoloration of the windows or the cell at temperatures up to 325°C.

Temperature control was probably the most important and difficult aspect of the absorption experiment. One data scan will be used to

explain the temperature measurement and variation. Figure 7 on the next page shows a typical data run from 0.7 to 1.3 microns at an average temperature of 271°C. The series of nine numbers written horizontally are the readings for the nine thermocouples placed around the cell. Their locations are shown in Fig. 6 below. The ones placed at the windows, numbers 1,3,7, and 8, register about 10°C hotter than the ones on the cell body, numbers 2,4,5, and 6. The latter are all within 2°C of each other. Thermocouple #9, which registered 21/22°C, was located at the cold junction of the other thermocouples to ensure that the reference temperature did not change significantly. The reference junction of #9 was located sufficiently far from the oven that it was always at room temperature. Thermocouple #8 was significantly hotter for this scan because it slipped away from the window toward the heater. For this reason, thermocouples were placed just inside the window, e.g. #1 and #7, to better measure the window temperature. The temperature was recorded several times during the 25 min scan, and the variation was usually 1°C or less.

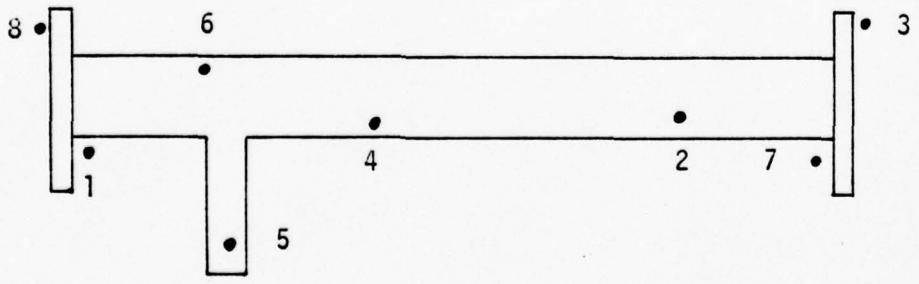

Fig. 6 Thermocouple Arrangement in Absorption Experiment

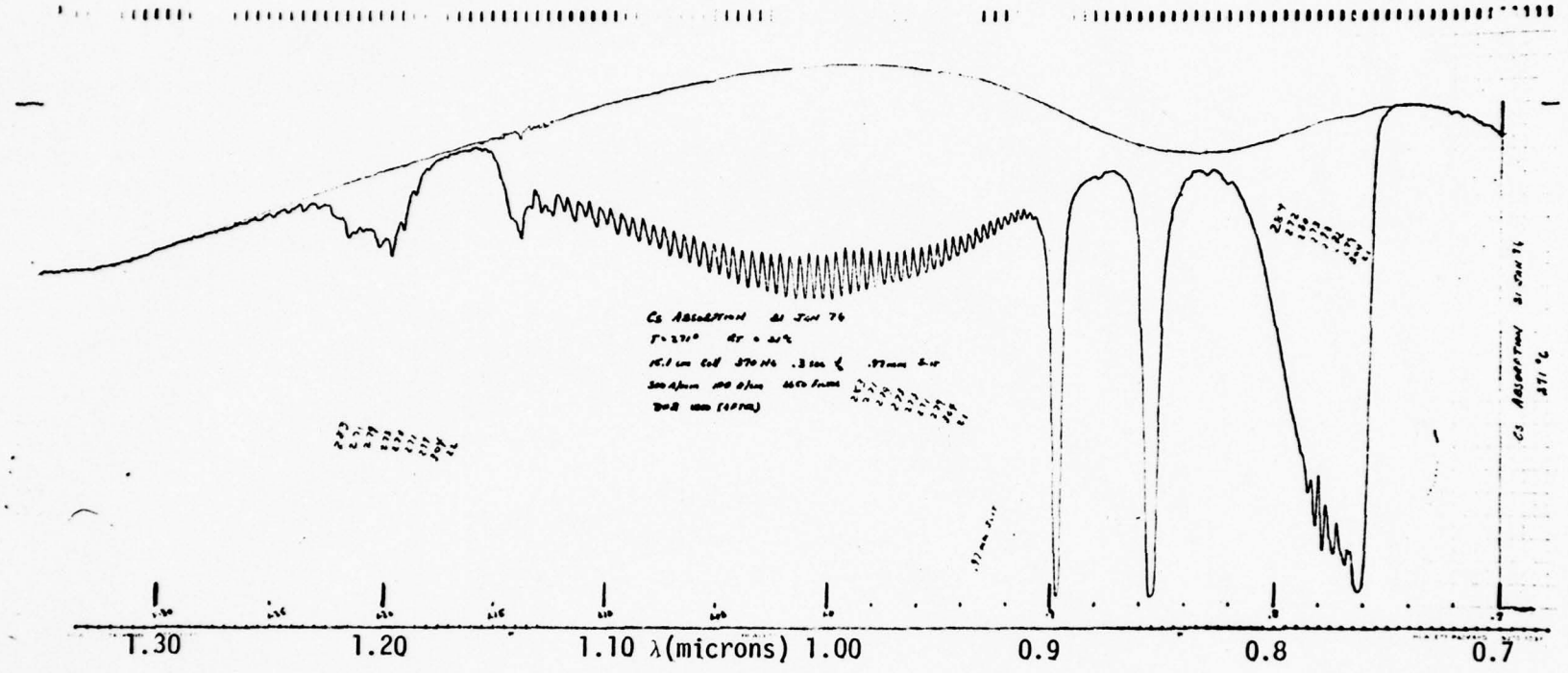

Fig 7 Sample Absorption Data Scan

The Cs vapor pressure P was determined from the average temperature on the body of the cell using the Taylor-Langmuir vapor pressure formula (Ref. 60)

$$LOG_{10}P = 11.0531 - LOG_{10}T - 4041/T \qquad (30)$$

where T is in degrees Kelvin. During and after an experimental run, the Cs condensed fairly uniformly along the cell body rather than in just one cold spot. The average temperature, therefore, seemed to be the best reference for the Cs vapor pressure. Because the temperature at any single point was within $\pm$ 2°C of the average, the temperature uncertainty was estimated to be $\pm$ 2°C. Since the Cs density was calculated from $[Cs] = 9.66 \times 10^{18} P/T$, the uncertainty in the Cs number density was $\pm$ 5% at 325°C and $\pm$ 8% at 182°C.

The data reduction in the absorption experiment was straightforward and the same data scan will be used as an example of the procedure. The upper, smooth curve in Fig. 7, is the background low temperature scan (I_a) taken before and after each high temperature scan (I_b). The system was always allowed to equilibrate for at least one hour at the elevated temperature before I_b was recorded. The absorption coefficient (α) was calculated from $\alpha = -[\ln(I_b/I_a)]/d$, where d is the cell length. In order for a set of data to be acceptable, the before and after scans at low temperature had to agree within 1.0 mm over the entire spectrum. Each major division on the chart paper in Fig. 7 is 1.0 cm. Furthermore, the I_a and I_b scans had to match up in the regions 0.72 - 0.74 microns and beyond 1.30 microns. There was no absorption observed in these regions even for temperatures of up to 390°C, so these regions could be

used as calibration points to be checked each scan. This gave assurance that the system was not changing during the heating and cooling periods. Since the experimental setup was quite stable, over 90% of the data taken met the above requirements. The remaining 10% could not be reliably reduced and were discarded.

Absorption Experiment Error Summary

The two primary sources of uncertainty, or error, in the absorption experiment were in the temperature determination and in the measurement of I_b and I_a. The length of the tube was known to $\pm$ 0.5%, a negligible contribution to the overall error. As previously described, the temperature uncertainty was estimated at $\pm$ 2°C. There was also an uncertainty of less than $\pm$ 1.5% in the vapor pressure predicted by Eq. 30 (Ref. 61) which, when added to the temperature uncertainty, gives an uncertainty in the Cs number density of $\pm$ 6.5% to $\pm$ 9.5%. The uncertainty in I_a was previously stated as 1.0 mm (or $\pm$ 0.5 mm) giving a percentage error of $\pm$ 0.2% to $\pm$ 0.5% depending on the wavelength. The possible error in I_b was also estimated to be 1.0 mm. By differentiating the equation used to determine α, one can determine the variation in α i.e. $\delta\alpha$, for a given variation in I_b, i.e. δI. The result is $\delta\alpha = -\delta I/I_b d$. To do this, the errors in I_b and I_a are ascribed to I_b and the average uncertainty taken to be $\pm$ 0.5%. For the worst case, d = 15.1 cm and $\delta I/I_b = \pm .005$, so $\delta\alpha = \pm .0003$/cm. The percentage error in α, therefore, ranged from $\pm$ 30% to less than 1% depending on the temperature, wavelength, and cell length. As a rough average, the absorption coefficient for 0.9 to 1.22 microns usually had an uncertainty of less than $\pm$ 5% and the uncertainty $\lambda > 1.22$ microns was approximately $\pm$ 10%.

Fluorescence Experiment Description

A schematic diagram of the fluorescence experiment is shown in Fig. 8. The light from the 150 watt lamp was filtered by the pump filter, mechanically chopped at 70 Hz, and focused on the center of the pyrex cell by an F/1 lens. The lamp was controlled by the regulated dc power supply previously mentioned. The fluorescence light from the cell was focused on the front of the same spectrometer used in the absorption experiment. Since the slit width was set at 3 mm, the resolution could be estimated as approximately 25 Å. A 0.665 micron sharp cutoff filter on the spectrometer entrance slit eliminated second and higher order spectra. An intrinsic Germanium photodiode was used to detect the output from the spectrometer. This detector was manufactured by North Coast Optical Systems, had a detectivity of 1.5×10^{13} cmHz$^{\frac{1}{2}}$/watt and an area of 0.25 cm^2. It was operated with a 350 volt reverse bias at 77^{o}K and had a sapphire window. The light exited the spectrometer horizontally, was reflected 90° to the vertical, and focused on the detector by an F/1 lens. Vertical operation of the detector allowed refilling of the surrounding liquid nitrogen dewar without disturbing the detector alignment. The alignment was extremely critical for this experiment so it was imperative that nothing have to be moved during the experiment. The signal from the photodiode was sent through a low pass filter into the lock-in amplifier and the spectra was displayed on the strip-chart recorder. These equipments are not shown in Fig. 8, however, they are the same ones used in the absorption experiment.

The pyrex cells used in the fluorescence experiments are shown in Fig. 8. They were typically 1.0 in. diameter cyclinders and about 1.0 in. long with a short 3/8 in. stem. They were prepared in the same

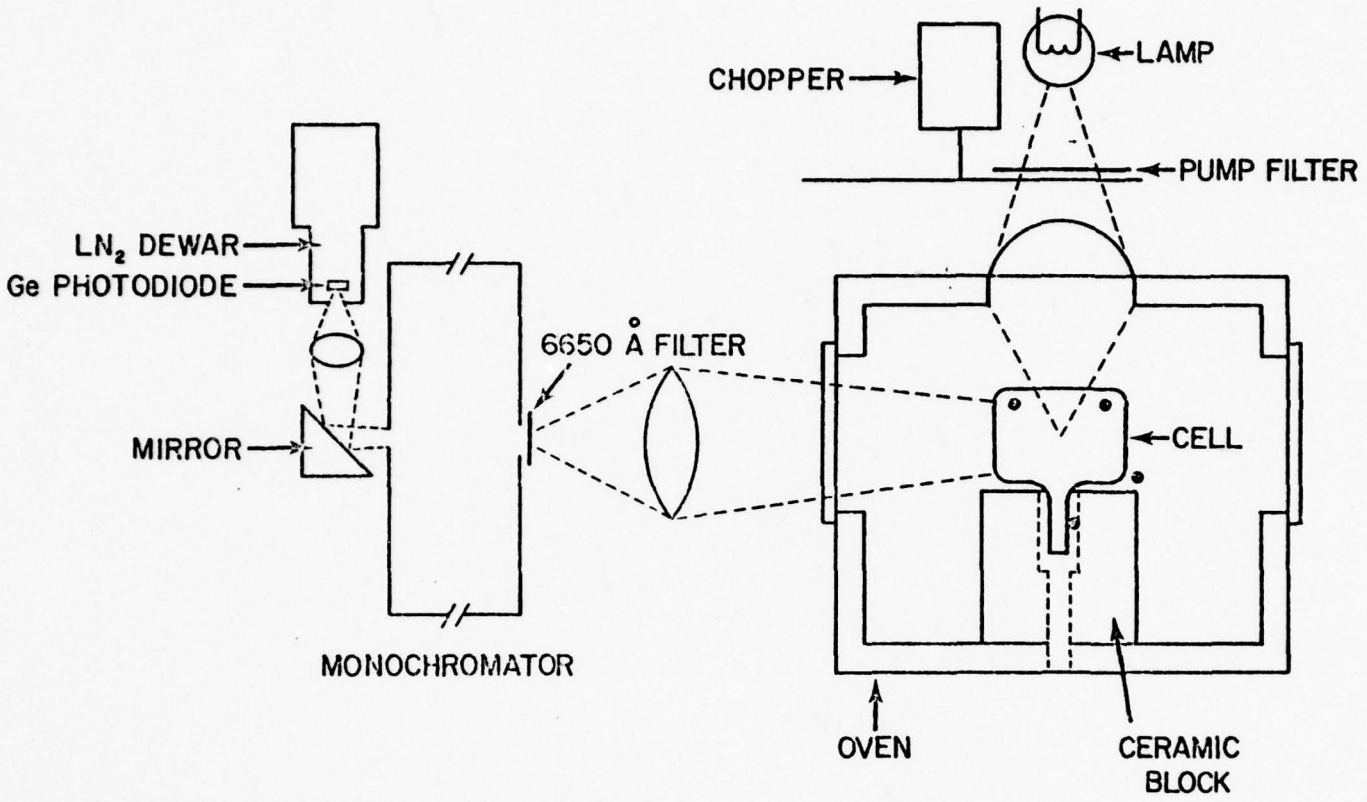

Fig 8 Schematic Diagram of the Fluorescence Experiment

manner as the absorption cells. The Cs was added by distillation after the cells had been cleaned. Finally the cell was filled with Research Grade Xenon to the desired pressure and the cell sealed off. Since the pressure gauge could be read with an accuracy of $\pm$ 0.1 psi, the pressure had an uncertainty of $\pm$ 1% to $\pm$ 7% depending on the Xe pressure. The cells which required densities greater than atmospheric density were filled by freezing the Xe into the cell. This was done by first pressurizing the cell and part of the vacuum system to a pressure determined by the desired Xe density and the ratio of the cell volume to the total volume under pressure. Next the Xe gas bottle was closed off from the cell so that a known and fixed amount of Xe was available. The cell was cooled to liquid nitrogen temperature and, since the vapor pressure of Xe is less than 1.0 torr at 77°K, essentially all of the Xe was frozen into the cell. The cell was then sealed with a torch. The resultant Xe density had an uncertainty of $\pm$ 2%. This is a combination of the uncertainties in measuring the appropriate volumes and in reading the pressure gauge. None of the cells used in the experiment showed any signs of leakage during the course of the observations. A total of six cells were used during these experiments, five with the following Xe densities: 5×10^{19}, 1×10^{19}, 5.5×10^{18}, 2.5×10^{18} cm^{-3} and one cell filled just with Cs. The density limit was 5×10^{19} cm^{-3} because the cells that were filled to a higher density exploded when heated higher than 200°C.

The oven was constructed of maronite, an asbestos insulator, with coiled nichrome wire on each side as the heating element. The front and back of the oven had two-inch holes in the maronite covered by 1/8 in. thick pyrex windows. In the center of the oven a heavy ceramic insulator was used to hold the cell. A hole was cut in the center of

the ceramic for the cell stem. This opening continued through the bottom of the maronite oven so that the stem could be kept at a lower temperature than the rest of the cell. This caused the Cs to condense in the stem rather than on the windows.

In order to determine the temperature of the cell, four thermocouples were used. One thermocouple was placed next to the stem in the ceramic block to measure the cold spot temperature. This was the temperature that determined the Cs vapor pressure. The temperature variation along the bottom of the stem, where the Cs always condensed, was always less than 6°C so the cold point temperature was assumed to be accurate to $\pm$ 3°C for all the experiments. Three more thermocouples were placed around the main cell body, one near the bottom of the cell on the ceramic block and the other two between the middle and top of the cell on either side. Usually, the top two thermocouples were within 2°C of each other. The lower one was about 15°C colder since it was closer to the cold point. Most of the temperature variation occurred in the lower third of the cell--determined by moving the thermocouples to several locations. The average of all three thermocouples was used to specify the cell temperature giving an uncertainty of about $\pm$ 6°C or $\pm$ 1% at 345°C. This average was typically within 25°C of the cold point. The Cs vapor pressure was determined from Eq. 30 using the cold point temperature. The Cs number density was calculated from $[Cs] = 9.66 \times 10^{18} P/T_c$ where T_c was the average cell temperature in degrees Kelvin. Therefore, the uncertainty in the Cs density at 345°C was $\pm$ 8% primarily due to the uncertainty in the cold point temperature. When the estimated error in Eq. 30 was added, the total error in [Cs] was $\pm$ 9.5% for temperatures near 345°C, the temperature where most of the data was taken.

The relative spectral response of the system was measured twice during the course of the fluorescence experiments. A 1000 watt Eppley Standard Lamp (Model ES-7501), with a known spectral irradiance and powered by the previously mentioned precision dc power supply was used. The light from the lamp was chopped and sent through the cell and optical components into the spectrometer and to the Ge detector. The response was measured both with and without the cell and with and without a CaF_2 diffuser. The diffuser was placed between the lamp and the cell to eliminate any chromatic aberrations. The transmission of CaF_2 is essentially independent of wavelength over the range of interest. In all cases, the data was repeatable to within $\pm$ 2%. The resultant spectral response curve is shown in Fig. 9 in terms of relative response per wavenumber. The response at 0.96 microns was set equal to 1.0 because that was the wavelength that was chosen for the normalization. Each of the cells used in these experiments was checked before and after the data acquisition to determine any transmission changes. Although the cells did darken slightly because Cs slowly attacks pyrex at the high temperatures used, only the magnitude of the transmission changed: there were no spectral changes. Therefore, the relative spectral response did not change with time or with cell discoloration.

For most of the experimental effort, three different pump filters were used. The transmission of each shown in Fig. 10. The filter referred to as the Atomic filter was used for optical pumping of both the D1(0.894 microns) and the D2(0.852 microns) lines of Cs. The location of these lines is also shown in Fig. 10. The D1 filter primarily allows pumping of the D1 line, but some direct pumping of the D2 line occurs (10% transmission) also. The D1 filter also permits some direct pumping

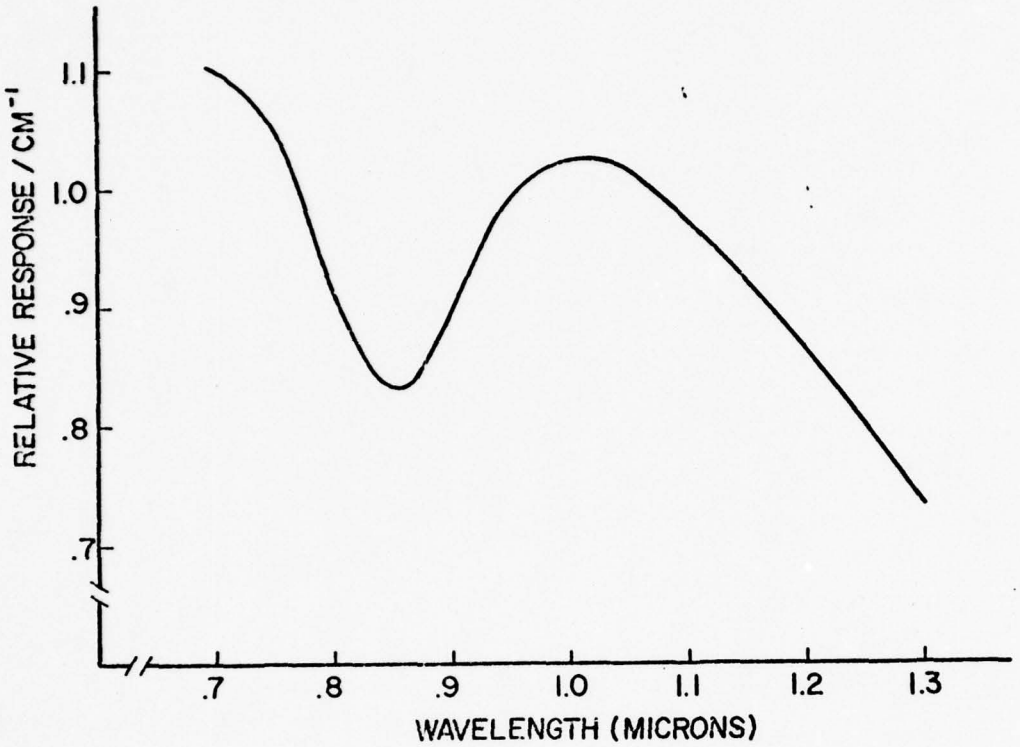

Fig 9 Spectral Response for the Fluorescence Experiment

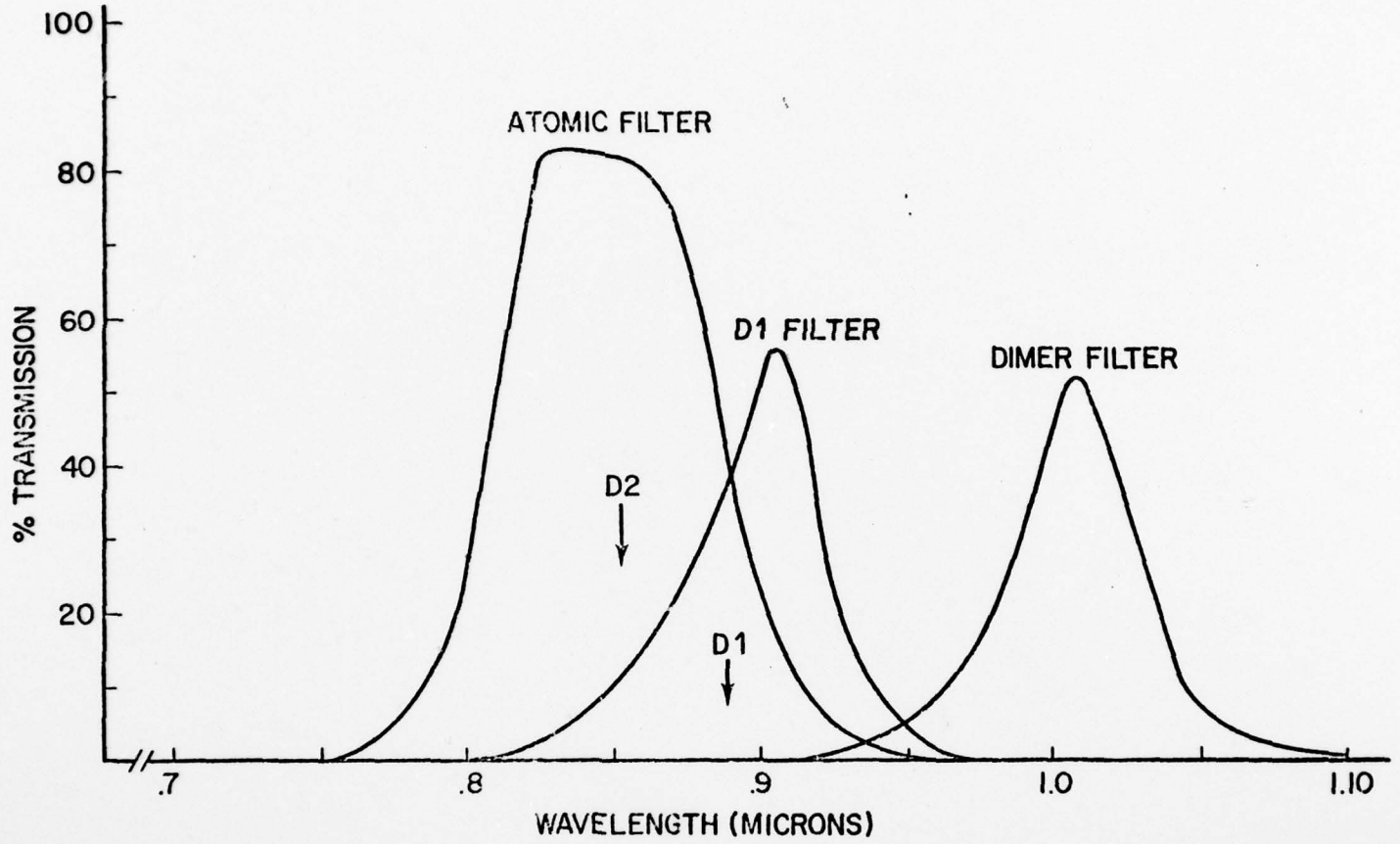

Fig 10 Pump Filter Transmission Curves

of the Cs_2 molecule, although the contribution should not be significant because of the low transmission of the filter in that region. Furthermore, the molecular absorption is not very strong there. Both filters permit considerable pumping on the CsXe wings of each line, but since the $CsXe^*$ and the Cs^* should be in thermal equilibrium with each other, this was about the same as pumping the atom directly. When using the Dimer filter, both the Cs_2 molecule and part of the CsXe D1 red wing were pumped. The Atomic filter was the primary filter used in these experiments because 1) it permitted direct pumping of only the atoms, 2) there was no leakage or scattered light near 0.96 microns, and 3) it gave the strongest fluorescence signal.

In order to conduct the actual fluorescence experiment, the equipment was arranged as shown in Fig. 8. The height of the pump light was adjusted so that the light was focused near the center of the cell. However, because of the large absorption, the pump light near line center was optically trapped within about 1 mm of the top of the cell. Most of the fluorescence originated from this location. This could be seen from the fact that the maximum signal was obtained when this portion of the cell was imaged on the center of the entrance slit. Final adjustments in the alignment were made to maximize the fluorescence signal while also minimizing the amount of light incident on the spectrometer that had been scattered from the edges of the cell. The scattered light outside the filter transmission was, of course, unimportant; however, scattered light from 0.9 to 0.95 microns could affect some of the data and, therefore, was minimized. Light scattered inside the spectrometer from the strong signal region was, for the most part, less than 1%. Corrections made for this are discussed in the data reduction section.

Before each fluorescence scan was made, the cell allowed to equilibrate at the desired temperature for at least one hour. The fluorescence at one particular wavelength, usually on the D1 CsXe red wing, was monitored until it remained steady, within $\pm$ 3%, before recording the data. Most of the data scans were taken from 0.8 to 1.3 microns with occasional runs starting at 0.7 microns to measure any possible $B^1\pi$ fluorescence. The scattered light from a cold cell with the pump filter in place was also measured so that it could later be subtracted from the high temperature scan. The early data was usually taken at 250 Å/min with a 1 or 3 sec time constant. Because the detector sensitivity decreased over a period of weeks, the later data was recorded at 125 Å/min and a 10 sec time constant.

The cause of the decrease in detector capability was thought to be a gradual contamination of the Ge chip due to continual temperature cycling or even very small outgassing of its evacuated container. For proper operation at the advertised detectivity, the intrinsic Ge must be extremely pure and free from contaminants. Even a slight change will significantly affect the signal-to noise ratio. In any case, the major effect of this decrease in sensitivity was to slow down the data taking and, finally, to significantly increase the noise in the data. At the end of the experiments, the detector had to be returned to the manufacturer for repair.

Fluorescence Experiment Data Reduction

There were four separate steps involved in the reduction of the fluorescence data. First the scattered (or leakage) light that had been measured on a cold cell, was subtracted from the signal. This was less

than a few per cent correction except where the signal was very weak. For example, beyond 1.23 microns, the uncertainty in the data was significantly greater than elsewhere because of this correction. Next, the spectrum was adjusted for the relative spectral response. This correction was the largest for the long wavelengths, 25% for 1.26 microns, but had an uncertainty of only about $\pm$ 2%. Therefore, it added little to the overall experimental error. Third, the spectrum had to be corrected for the self-absorption of Cs_2. The appropriate Cs_2 absorption coefficient was determined from Eq. 21 using the potential curves derived in the absorption experiment. The distance from the main fluorescence volume to the cell edge was 1 cm. Since the maximum Cs_2 absorption was 0.12 cm^{-1}, with an uncertainty of 5%, the largest correction was 12 $\pm$ 0.6%. As with the spectral response correction, the Cs_2 correction added little to the overall error.

The fourth step in the reduction of the fluorescence data was the normalization of the Cs_2 emission to the Cs atomic emission, specifically the D1 line. Because, in these experiments, the atomic lines were optically trapped, the dimer emission could not be normalized directly. The normalized emission of CsXe had been measured (Ref 27). Therefore, the dimer emission was normalized to the CsXe emission and, thereby, to the atomic emission. By this process, the Cs_2 emission per excited Cs atom (D1) was obtained. The key to this was the normalized CsXe emission. In Ref 27, the authors measured the relative emission of CsXe to that of atomic Cs for a variety of temperatures. Using that normalized emission of CsXe and a CFCP analysis (Eq. 1), they developed the CsXe potential curves. Those potentials could then be used to calculate the normalized CsXe emission for the temperatures and Xe densities used in this research.

The primary requirement for this procedure was that the Cs^* and $CsXe^*$ be in chemical equilibrium as this is a condition for the validity of Eq. 1. To define what is meant by chemical equilibrium, one must rewrite Eq. 25 for CsXe assuming the only important processes are formation, radiation and dissociation.

$$\frac{[CsXe^*]}{[Cs^*]} = \frac{k_f[Xe]^2}{\Gamma+k_d[Xe]} \tag{31}$$

One says that $CsXe^*$ and Cs^* are in chemical equilibrium when radiation is unimportant, i.e. when $k_d[Xe] >> \Gamma$. This condition is satisfied for Xe densities greater than 4×10^{18} cm^{-3}, but probably not significantly below 2.5×10^{18} cm^{-3} (Ref 27). For this thesis, the assumption was made that equilibrium between Cs^* and $CsXe^*$ existed for Xe densities greater than 2.5×10^{18} cm^{-3}. This assumption was based both on the above mentioned CsXe data and a more detailed study of the Xe density dependence of the RbXe fluorescence (Ref 15). That study concluded that the Rb^* and $RbXe^*$ were in equilibrium for Xe densities greater than 2×10^{18} cm^{-3}. Since the CsXe ($A^2\pi$) potentials are shallower than the RbXe ($A^2\pi$) potentials, one would expect that equilibrium would exist in $CsXe^*$ under the same conditions of temperature and density that it does in $RbXe^*$.

The source of the graphs of the CsXe potentials was Ref 27. In addition to the potential curves, the article had graphs of the CsXe infinite temperature spectrum and the temperature dependence of the normalized emission at one wavelength on each of the CsXe D1 and D2 wings. There was also a plot of $\Delta k(R) = k_o - k$ where k_o is the atomic line center and $k(R) = V_u(R) - V_u(\infty)$. All the variables are in wavenumbers. Each

graph was digitized using a Tektronix Model 4662 digitizer to a precision of $\pm$ 0.01 in. which corresponds to about $\pm$ 10 cm^{-1} on the potentials. These potentials and $\Delta k(R)$ are shown in Fig. 11. By using each graph as a check on the other in conjunction with Eq. 1, an internally consistent model of the temperature dependence of the CsXe D1 and D2 wings was made.

The accuracy of the CsXe potentials has been estimated at about $\pm$ 50 cm^{-1} (Ref 27). The major source of this error was the difference in the CsXe ground states derived from separate analyses of the D1 and D2 wings (see Fig. 11). This uncertainty was reflected in two different ways. First, there was an uncertainty in the temperature dependence of the fluorescence at a particular wavelength. This was of the order of $\pm$ 10% (Ref 27). Second, there was an uncertainty in the shape of the wings which was also about $\pm$ 10% (Ref 27). Putting these together gave an uncertainty in the magnitude of the CsXe spectrum of $\pm$20% at any particular wavelength.

Because of the uncertainty in the shape of the CsXe wing, it was decided to normalize the Cs_2 data to one point on the wing. Then, the measured and predicted wings shapes were compared. As will be seen, the comparison was quite good. Three factors had to be considered in choosing the right normalization wavelength: Leakage of scattered light in the filter wings; D2 wing contributions to the observed D1 fluorescence; and Cs_2 fluorescence in the neighborhood of the normalization point. The first two restricted the choice to a wavelength greater than 0.95 microns. Consideration of the Cs_2 emission meant choosing as short a wavelength as possible. The result was the use of 0.96 microns as the normalization point. The potential curves predicted no D2 CsXe fluorescence

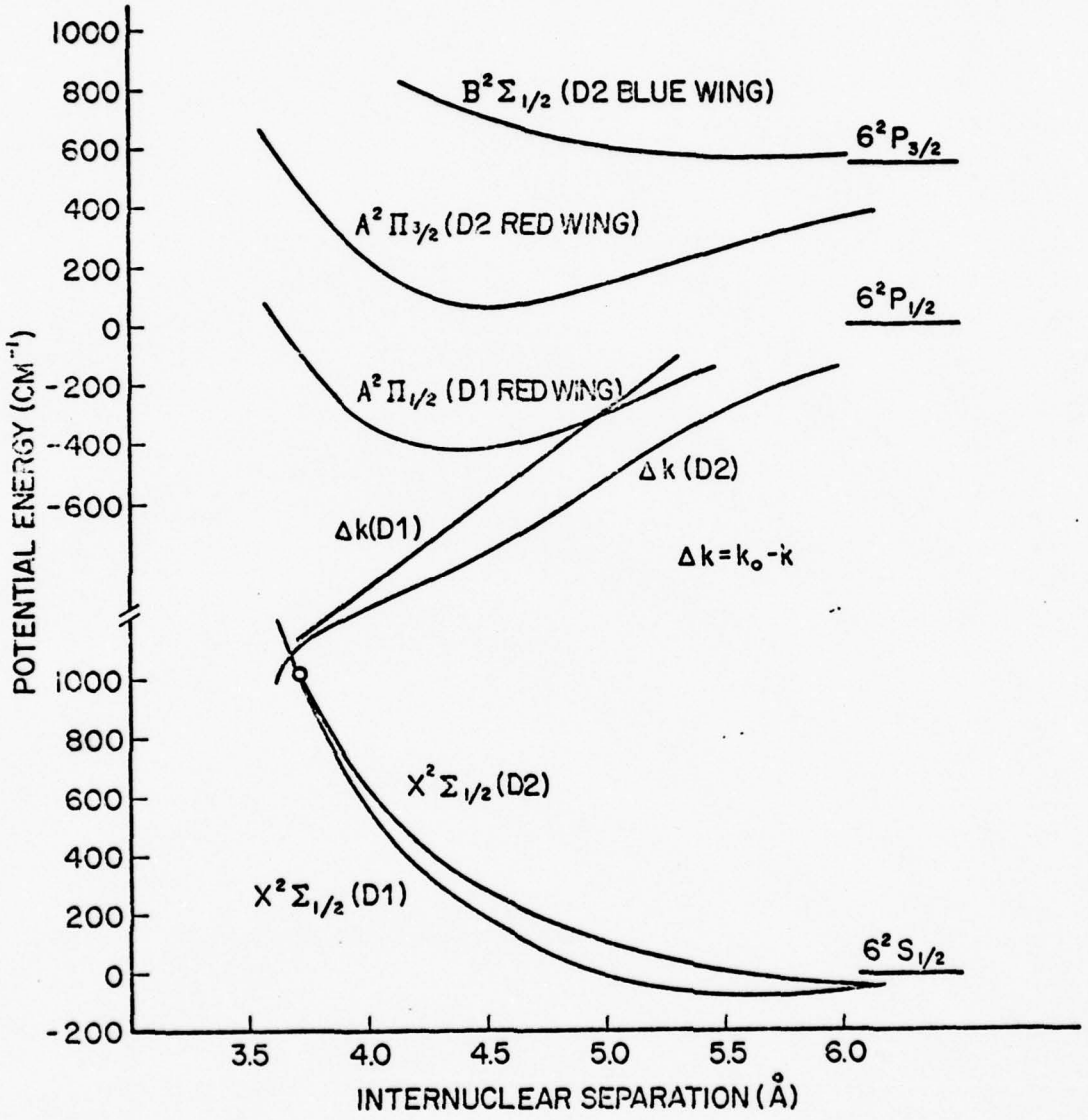

Fig 11 CsXe Potential Energy Curves (Ref 27)

there; no leakage light through the Atomic filter was seen on the cold cell tests; and, except for very low Xe densities, the Cs_2 emission was only a small contribution. Therefore, given the magnitude of the CsXe fluorescence from the CFCP analysis and correcting the observed spectrum for absorption and spectral response, the Cs_2 emission intensity per excited Cs atom could be determined.

Fluorescence Experiment Error Summary

The sources of error in the fluorescence experiment were certainly more numerous than for the absorption, but they were not as critical to the final result. They are recounted here briefly. The error in Xe density varied from $\pm$ 2% to $\pm$ 7% as [Xe] varied from 5×10^{19} to 2.5×10^{18} cm^{-3}. The temperature uncertainty was about $\pm$ 3°C for the cold spot and $\pm$ 6°C for the cell body giving a total variation in Cs density of $\pm$ 9.5%. The spectral response and absorption corrections contributed another $\pm$ 2% and $\pm$ 1% to the uncertainty of the fluorescence data respectively. The CsXe normalization error from the potential curves was estimated at about $\pm$ 20%. There are additional uncertainties ($\sim$5%) due to the signal-to-noise ratio, but these vary from scan to scan and have to be considered individually. Finally, at the low Xe densities, there are additional normalization errors because of the Cs_2 fluorescence near 0.96 microns. These will be discussed for each case, where they are important, in Chapter IV.

Chapter IV. Results and Analysis

The purpose of this chapter is to present the results of the absorption and fluorescence experiments and to discuss the analysis of these data. The absorption spectra are analyzed according to the CFCP and the primary result is the development of the Cs_2 potential curves. The fluorescence data is used to determine the fractional inversions necessary for gain in Cs_2 and to quantify the principle kinetic processes. The results of the fluorescence analysis are then used to model the behavior of the Cs_2 molecule and to explain the variations in the Cs_2 spectra for different Xe densities. Finally, the implications of this behavior on the viability of Cs_2 as a laser are discussed. Throughout the rest of this paper, all energy or frequency variables will be put in wavenumbers (cm^{-1}).

Absorption Results

The absorption of Cs/Cs_2 was measured over a temperature range of 182°C to 323°C. This represents a Cs density range of $8x10^{14}$ cm^{-3} to $5.45x10^{16}$ cm^{-3}. The data was reduced using the procedures discussed in Chapter III. The temperature dependence of the absorption was then used to determine the $A^1\Sigma$ potential curve from Eq. 21. In this section the absorption spectra, their interpretation, and the CFCP analysis, are discussed.

The experimental absorption spectra of Cs/Cs_2 vapor for five different temperatures and Cs densities are shown in Fig. 12. The respective Cs densities, starting with A, are $5.45x10^{16}$, $2.76x10^{16}$, $1.4x10^{16}$, $3.98x10^{15}$, and $2.12x10^{15}$ cm^{-3}. These spectra are typical of all the

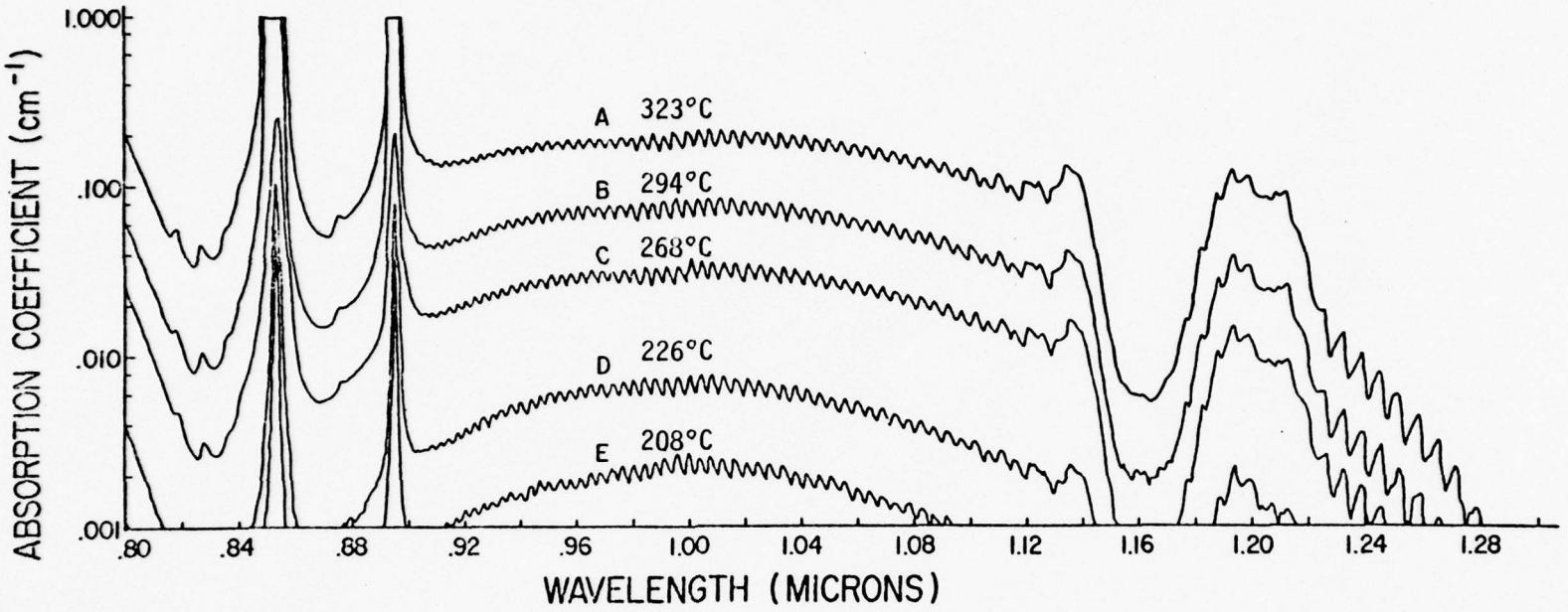

Fig 12 Experimental Absorption Coefficient in Cs/Cs_2

data taken from 182°C to 323°C. Below 182°C no molecular absorption could be seen and above 323°C the transmission in the region of strongest absorption was less than 5%. No reliable data could be taken when this occurred.

The strong absorption near 0.8 microns is part of the $X^1\Sigma_g^+ - B^1\pi_u$ transition of Cs_2. This transition has been photographically analyzed in detail by Kusch and Hessel (Ref 37), wherein they determined the first four vibrational constants for each state. The entire band can be seen in Fig. 7, which shows the unreduced absorption data. The peaks near 0.817 and 0.827 microns have been explained as absorption to the B-state and predissociation to a repulsive state that dissociates into 6P and 6S states of atomic Cs (Ref 37). The band near 0.877 microns, also reported by Loomis and Kusch (Ref 41) could possibly be absorption to high vibrational levels in the $A^1\Sigma$ state from the $X^1\Sigma$ ground state. The two large peaks centered at 0.8521 and 0.8944 microns are the D2 and D1 resonance lines of Cs, respectively. They are collisionally broadened by the Cs since there is no other broadening gas present. Because the resolution of the spectrometer was about 8 Å and because of the large optical depth, the linewidths could not be compared with those measured by other researchers such as Chen and Phelps (Ref 9).

The remainder of the spectrum is attributed to Cs_2, and there are several features of interest. First is the main sequence of bands from 0.9 - 1.14 microns, which are identified as the $X^1\Sigma_g^+ - A^1\Sigma_u^+$ transition both here and others (Refs 4, 33, 59). They are red-shaded which indicates that the equilibrium internuclear radius for the upper state is greater than that for the ground state (4.47 Å) (Ref 38).

Specifically, it is the relative size of the rotational constant $B_v = B_e - \alpha_e(v+1/2)$ of each of the two states that determines the shading (Ref 29). B_e is the equilibrium rotational constant and α_e the coupling constant between the rotational and vibrational energy. However, as will be shown, the difference in the B_e's of each state is large relative to the α_e's, so for the lower vibrational levels ($v < 40$) involved in this study, the relative sizes of the B_e's determine the shading. One higher resolution scan was taken wherein the spacing of the major peaks could be seen to vary from 37 cm^{-1} to 42 cm^{-1}. The larger spacing occurred near 1.0 microns and decreased in value in either direction. The observed spacing is consistent with the vibrational constant, ω_e, of 42 cm^{-1} given by Kusch and Hessel (Ref 37) for the ground state ($X^1\Sigma$) of Cs_2.

The second feature of the spectrum is the gap between the 1.135 micron and 1.195 micron peaks where the absorption is significantly decreased. This gap is thought to arise from the crossing of the $A^1\Sigma$ and the $a^3\pi$ states. The result of the crossing is a perturbation between the two electronic states that shifts the energy levels of each state away from their "normal" position (Ref 29). Since some levels are displaced to higher energies, and some to lower, there are now more energy levels available above and below the crossing, and so the absorption increases on either side of the gap. The gap itself represents the region of the unperturbed or zero-approximation energy levels. The density of the levels in this region has been significantly reduced because of the perturbation. Therefore, the absorption is substantially less than would be expected. A similar, although narrower, gap has been seen in Rb_2 and it also is thought to arise from the

crossing (Ref 16).

The third spectral region of interest is that from 1.22 microns to 1.30 microns. Here the absorption is reduced considerably from the 1.19-1.21 micron peak, and the vibrational spacing is about 40 cm^{-1}. In higher (3.5 Å) resolution scans, there appears to be several sequences of subsidary peaks spaced about 50 cm^{-1} apart. All the absorption peaks in this region are shaded to the blue rather than to the red as was observed for $\lambda < 1.13$ microns. The blue shading implies that the upper state has an equilibrium separation less than 4.47 Å, that of the Cs_2 ground state. Therefore, these blue-shaded peaks are assumed to arise from a different transition than the $X^1\Sigma$ - $A^1\Sigma$ responsible for the red-shaded bands. This new state necessarily lies below the $A^1\Sigma$ state and is believed to be the $a^3\pi_u$ state first predicted by Mulliken (Ref 45). The $X^1\Sigma$ - $a^3\pi$ is normally a forbidden transition; however, in a heavy molecule like Cs_2, the spin-orbit coupling is thought to be sufficient to weakly allow the transition (see discussion below). In addition to the region 1.22-1.30 microns, there are some blue-shaded peaks on the 1.19-1.21 micron hump. This also indicates the presence of two different electronic states at these wavelengths. Previous authors (Refs 4, 33, 59) have identified the 1.13 micron peak with the $A^1\Sigma$ state and the 1.19-1.21 micron peak with the $a^3\pi$ state. The blue-shaded peaks from 1.22-1.30 microns can be seen in Bayley's (Ref 4) and Kostin's (Ref 33) data but they are not discussed.

Before continuing this discussion, a few words must be said about allowed versus forbidden transitions for the case of large spin-orbit coupling. Hund originally described several coupling cases for molecules, two of which are of importance here, case (a) and case (c).

(see for example Herzberg, Ref 29, and Mulliken, Ref 45). Case (a) refers to the situation where the electronic motion is strongly coupled to the internuclear axis and case (c) occurs when the interaction between the resultant molecular orbital angular momentum (L) and spin (S) are more closely coupled to each other. In case (a), both Λ, the component of electronic orbital angular momentum along the internuclear axis, and Σ, the spin component along the internuclear axis are good quantum numbers. The resultant electronic angular momentum quantum number is given by $\Omega = |\Lambda+\Sigma|$. For case (c), L and S are strongly coupled to form a resultant total angular momentum J^a. The only good quantum number is $\Omega = |M_{J_1} + M_{J_2}|$ where M_J is the component of the resultant atomic angular momentum along the internuclear axis. The pertinent selection rules for case (a) are $\Delta\Lambda = 0, \pm 1$ and $\Delta\Sigma = 0$, whereas for case (c) the corresponding selection rule is $\Delta\Omega = 0, \pm 1$. The case (a) states use $\Lambda = 0,1,2...$ to designate the states as Σ, π, Δ... states, etc. For case (c), Ω is used and the states are denoted by 0,1,2...

In a heavy molecule such as Cs_2, the spin-orbit coupling is fairly large and the molecular states might be characterized as case (a) or case (c). The halogen homonuclear molecules have been treated this way for years (Ref 45). The effect of the large spin-orbit coupling is a breakdown in the $\Delta\Sigma = 0$ selection rule. Previously, the $a^3\pi - X^1\Sigma$ transition has been referred to as forbidden by spin consveration. If one uses case (c) nomenclature, this would become the $a0_u^+ - X0_g^+$ or $a1_u - X0_g^+$ transition, depending on the value of Ω. Both of these transitions are allowed. When referring to the $a^3\pi$, the value of Ω should be specified also, such as $a^3\pi_{0u}$ or $a^3\pi_{1u}$, rather than the entire $a^3\pi$ manifold. However, there was no way to distinguish them.

Most likely Cs_2 could be described as belonging to either or both coupling cases. The case (a) terminology will be used because it is more common, with the proviso that the singlet-triplet (intercombination) transition may be partially allowed.

The traditional type of vibrational analysis of the absorption data was not attempted because the resolution was not good enough to unambiguously assign the band heads in a Deslandres Table. The sensitivity of the PbS detector limited the resolution. Therefore Eq. 21, which gives the absorption coefficient according to the Classical Franck-Condon Principle, was used to analyze the data. In using this approach, several assumptions and approximations were made. The theory developed in Chapter II was based on the assumption that the spectrum is a smooth function of wavelength. As seen in Fig. 12, the vibrational structure is only about a 25% variation on top of a smooth average spectrum. Therefore, that assumption is reasonably valid, except in the region of the crossing. That region is an exception to the entire quantitative analysis because it presents a breakdown of the Born-Oppenheimer approximation (separation of electronic and nuclear wavefunctions).

Another assumption made in the development of Eq. 21 was that the electric dipole moment M was not a function of nuclear coordinates, i.e., $M \simeq M_0$ in Eq. 5. There is no direct experimental evidence in Cs_2 to confirm or deny this assumption. Some work has been done in Na_2 on this question and the most recent results indicate that M is constant with R (Ref 6). Previous experiments have indicated a variation (Ref 30); however, those results have been severely called into question and the latest work maintains that M is independent of R (Ref 6). This result is used in Eq. 21. The third assumption concerns

the magnitude of $A_m(\nu_o)$. Using ν_o as the Cs D1 line, the molecular A-coefficient at ν_o was assumed to be twice as strong as the atomic A-coefficient. This was predicated on the fact that there are two "outer" electrons that can participate in the transition. Also past work on Na_2 and K_2 B-state lifetimes (Ref 3) and on the Na_2 A-state lifetimes (Ref 17) indicate that this ratio varies between a factor of 1.5 to 2.0. This gives $A_m(\nu_o) = 5.9 \times 10^7$/sec since τ_a = 34 nsec (Ref 39) for the D1 state.

The final assumption is that ν is a single-valued function of R. However, $\nu(R)$ is not truly single-valued since it goes through a minimum near 1.22 microns giving the quasistatic satellite mentioned in Chapter II, the last part of which can be seen as a shoulder on the 1.19 - 1.22 micron hump. Contributions to the absorption from radii greater than the satellite radius (R_s = 6.0 Å) are negligible, except at very high temperatures, because they originate high in the ground state potential well. This satellite denotes the closest approach of the $X^1\Sigma$ and $A^1\Sigma$ potential curves. Therefore, any absorption from the $X^1\Sigma$ state at longer wavelengths, other than the motional broadening resulting from the breakdown of the stationary phase approximation, must be to a different state, i.e., the $a^3\pi$.

The temperature dependence of the absorption at specific wavelengths was determined by plotting $\alpha/[Cs]^2$ vs 1/T. According to Eq. 21, the slope gives $V_1(R) - V_1(\infty)$, so one can identify the depth in the ground state well from which the absorption originates. These data, together with the ground state potential, are later used to predict the observed spectrum. The temperature dependences of five different wavelengths are plotted in Fig. 13. The slopes are 3650, 3410, 2970, 2310, and

3810 cm^{-1} respectively. In fact, for all wavelengths shorter than 1.22 microns, the slopes varied from 1800 to 3650 cm^{-1}. The 1.228 micron temperature dependence will be discussed later. All of the slopes were determined using a least squares fit to the data. The one sigma variations were always less than 10% and mostly less than 5%. In addition, there was the estimated $\pm$ 12% uncertainty in $[Cs]^2$, so the total uncertainty was about $\pm$ 17%. As will be seen, the agreement between experiment and theory is much better than that. There was one more minor source of uncertainty. At the higher temperatures (T>300°C), where the transmission through the absorption cell was less than 10%, the scattered light in the spectrometer became noticeable. The scattered light was approximately 1% of the background level. The effect was to increase the temperature dependence slightly, less than 2%.

The second step was to attempt to match the magnitude and shape of the spectra using Eq. 21. The ground potential well, obtained from the spectroscopic constants of Kusch and Hessel (Ref 37) by the Rydberg-Klein-Rees (RKR) method (Ref 54), was used as a starting point. The RKR method is described in Appendix B. The $X^1\Sigma$ potential curve will be discussed further in the next section. The next step was to assume $\nu(R)$, or equivalently $k(R)$, using the temperature dependence together with the ground state, and compute the spectrum from Eq. 21. After several iterations, a k(R) curve was determined that resulted in agreement with the data over all temperatures. In order to get good quantitative agreement with the experimental data, a well depth(D_e) of 3420 cm^{-1} was required. This compares with a D_e = 3197 $\pm$ 80 cm^{-1} from Kusch and Hessel (Ref 37). The uncertainties in this analysis, in the Cs number density, and the A-coefficient, result in an uncertainty of about

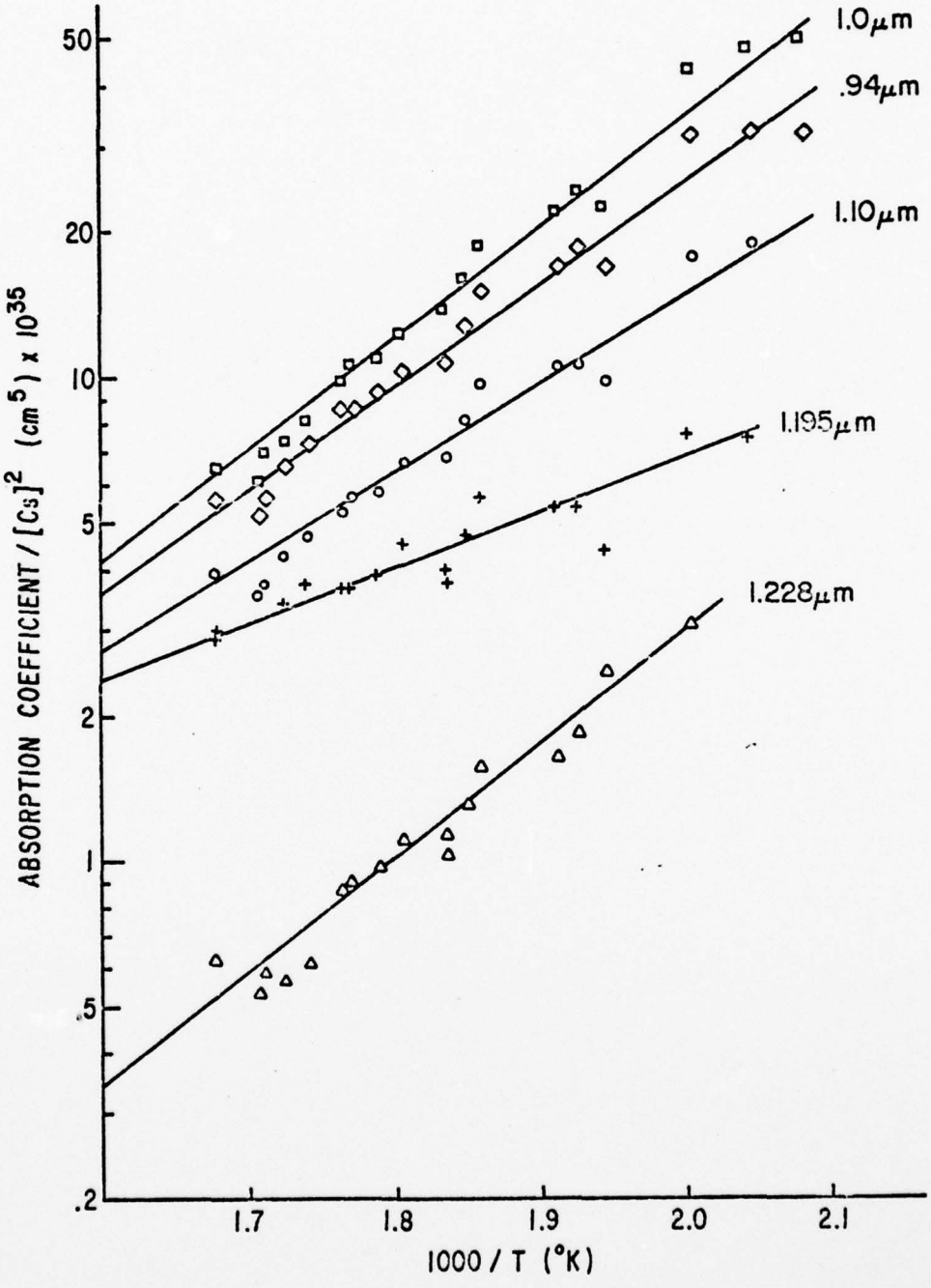

Fig 13 Temperature Dependence of Cs_2 Absorption

$\pm$ 200 cm^{-1} in the estimate of D_e. Therefore, the variation between the D_e of Kusch and Hessel and the one developed here appears to be within the range of the combined uncertainties.

A sample comparision of the measured spectrum and the one calculated by Eq. 21 is shown in Fig. 14. As can be seen in that figure, the entire spectrum is very well matched in shape for $\lambda < 1.14$ microns. For longer wavelengths, the crossing severely perturbs the spectrum. The CFCP theory cannot account for the gap around 1.16 microns nor the "extra" absorption around 1.2 microns. Using Eq. 21 and averaging over about 10 Å on either side of the discontinuity at 1.215 microns where $\left|\frac{d\nu}{dR}\right| \to 0$, the quasi-static satellite can be approximated as shown by the dotted line in Fig. 14. The magnitude is uncertain again because of the proximity of the crossing; however, the sharp dropoff for $\lambda > 1.215$ microns is according to the CFCP (neglecting the slight nuclear motional broadening). For all of the temperatures, the agreement between the experimental and theoretical spectra was better than 15% and usually better than 5%. The absorption beyond 1.22 microns could not be reproduced using the CFCP and a single upper state.

The ground state potential used for this analysis is shown in Fig. 15. Also given in that figure are the locations in the well from which the absorption at several different wavelengths originates. The radial position is determined from the spectrum matching and the well depth from the slope of the temperature dependence curves. The error bars represent only the one sigma deviation obtained from the least squares fit. There is also the $\pm$ 12% uncertainty in $[Cs]^2$. If this were included, it would put the potential well within all the error limits. To improve the agreement, one could have assumed $A_m(\nu_o) = 5 \times 10^7$/sec.

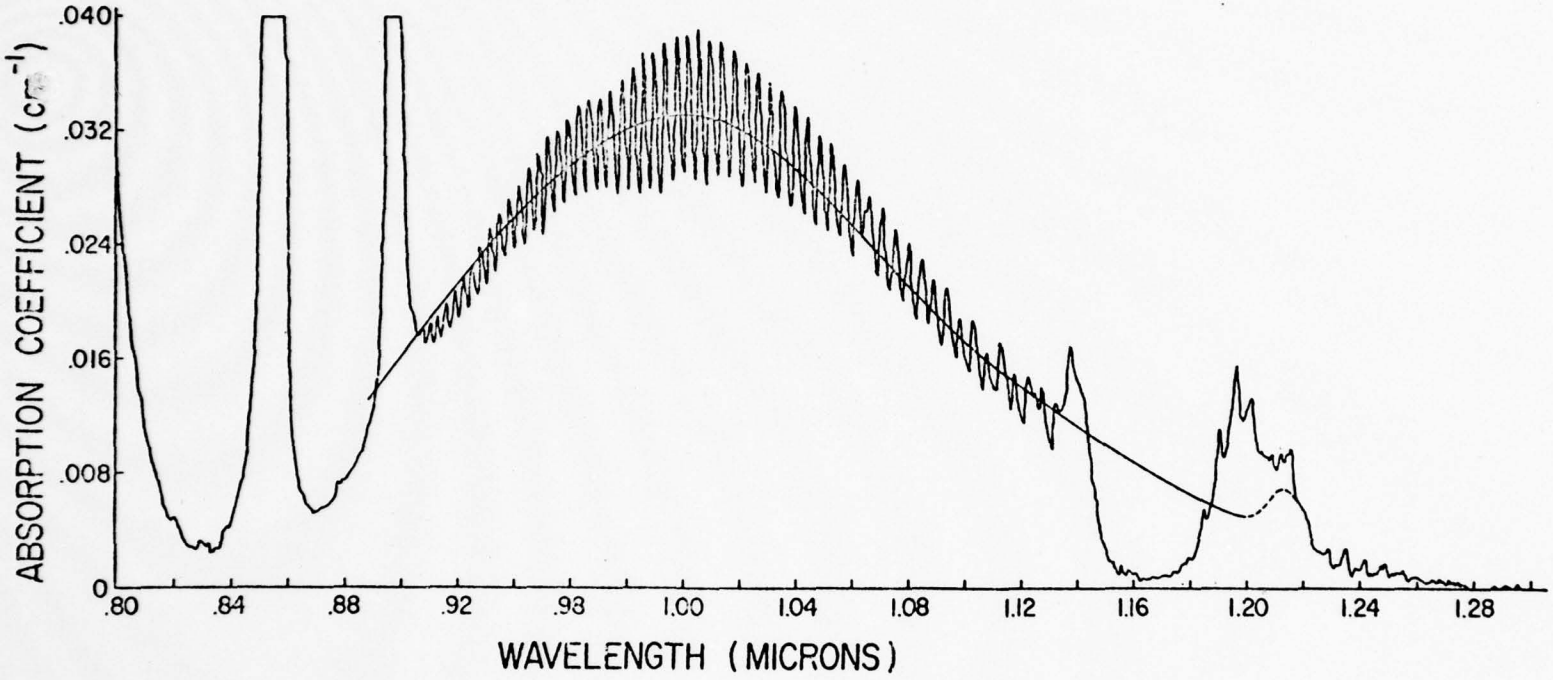

Fig 14 Comparison of Experimental Absorption Coefficient and Coefficient Calculated from Cs_2 Potentials at 271°C

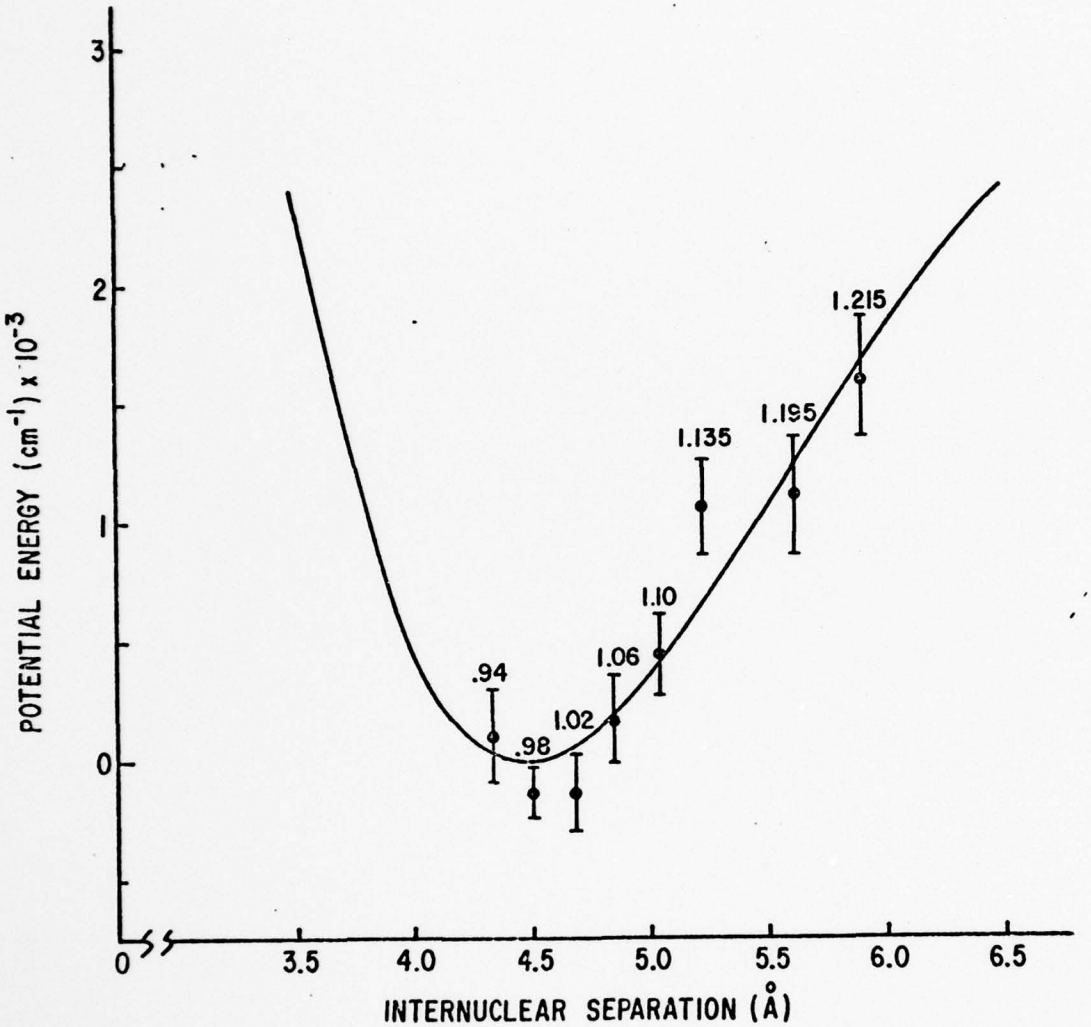

Fig 15 Cs_2 Ground State Potential Showing Location of Several Absorption Wavelengths (in Microns)

Then all the temperature dependences, except for 1.135 microns, would have fallen within the one sigma range. However, in order to match the spectrum in magnitude also, D_e would have to be equal to 3500 cm^{-1} or 300 cm^{-1} larger than that obtained by Kusch and Hessel. As a compromise, the previously mentioned values of $A_m(\nu_o) = 5.9 \times 10^7$/sec and D_e = 3420 cm^{-1} were used. The anomalous temperature dependence at 1.135 microns is probably related to the perturbation and a spectrometer anomaly at that wavelength (see Fig. 7). Thus both the temperature dependence and the spectral matchup confirm the belief that the 1.13 and 1.19 micron humps are part of the same $X^1\Sigma$ - $A^1\Sigma$ transition rather than split between the $X^1\Sigma$ - $A^1\Sigma$ and $X^1\Sigma$ - $a^3\pi$ transitions as others have mentioned (Refs 4, 37, 59).

Previously, Kostin and Khodovoi (Ref 33) have measured the absorption of Cs_2 and, although the shapes and features of the data in this work are essentially identical to theirs, the magnitude of their absorption was approximately a factor of four smaller for temperatures between 280°C and 320°C. This difference could be caused by a temperature error of 20°C. Some early absorption data obtained by Wechsler (Ref 65) over a narrow wavelength range and only at 329°C agrees with the absorption data in this work to within 30%. Based on the CFCP analysis and the corroboration of Wechsler's data, the conclusion is made that the absorption coefficient obtained is accurate at least to within 20%.

As previously mentioned, the entire spectrum, 0.9 to 1.3 microns, could not be matched in the CFCP analysis using a single upper state. The absorption beyond 1.22 microns could not be obtained from the analysis. The temperature dependence of the blue-shaded peaks beyond 1.22 microns - for example see Fig. 13: λ = 1.228 microns - exhibited a

steeper slope than any others, especially the nearby peaks such as the one at 1.195 microns. This steep slope implies that these peaks originate near the bottom of the ground state. In fact, the slope is 3800 cm^{-1} which is considerably deeper than the previous analysis shows the ground state to be. Since the absorption was very weak ($<10^{-3}$ cm^{-1}) at low temperatures, the slope has a greater uncertainty than for the regions of stronger absorption. See, for example, the relationship of $\delta\alpha$ to α in Chapter III. Also, the vibrational structure is a major part of the spectra in this region, much more so than the 25% variation on the continuum seen at shorter wavelengths. Since this represents a more severe breakdown of the random phase approximation, the CFCP analysis is not as useful or as appropriate as for the $X^1\Sigma$ - $A^1\Sigma$ transition. A vibrational analysis, using a Deslandres Table, was attempted but again the ambiguity of placement was too great. Nevertheless, it is apparent that these blue-shaded peaks do not belong to the same transition as the red-shaded ones. This further confirms the belief that they identify the $X^1\Sigma$ - $a^3\pi$ transition.

Cs_2 Potential Curves

The ground state potential of Cs_2 is shown in Figs. 15 and 16. It was calculated from the spectroscopic constants determined by Kusch and Hessel (Ref 37) which are shown in Table III. The first four constants are the coefficients in the vibrational term value, G(v), as shown in Eq. 32

$$G(v) = \omega_e(v+\tfrac{1}{2}) - \omega_e x_e(v+\tfrac{1}{2})^2 + \omega_e y_e(v+\tfrac{1}{2})^3 + \omega_e z_e(v+\tfrac{1}{2})^4 \qquad (32)$$

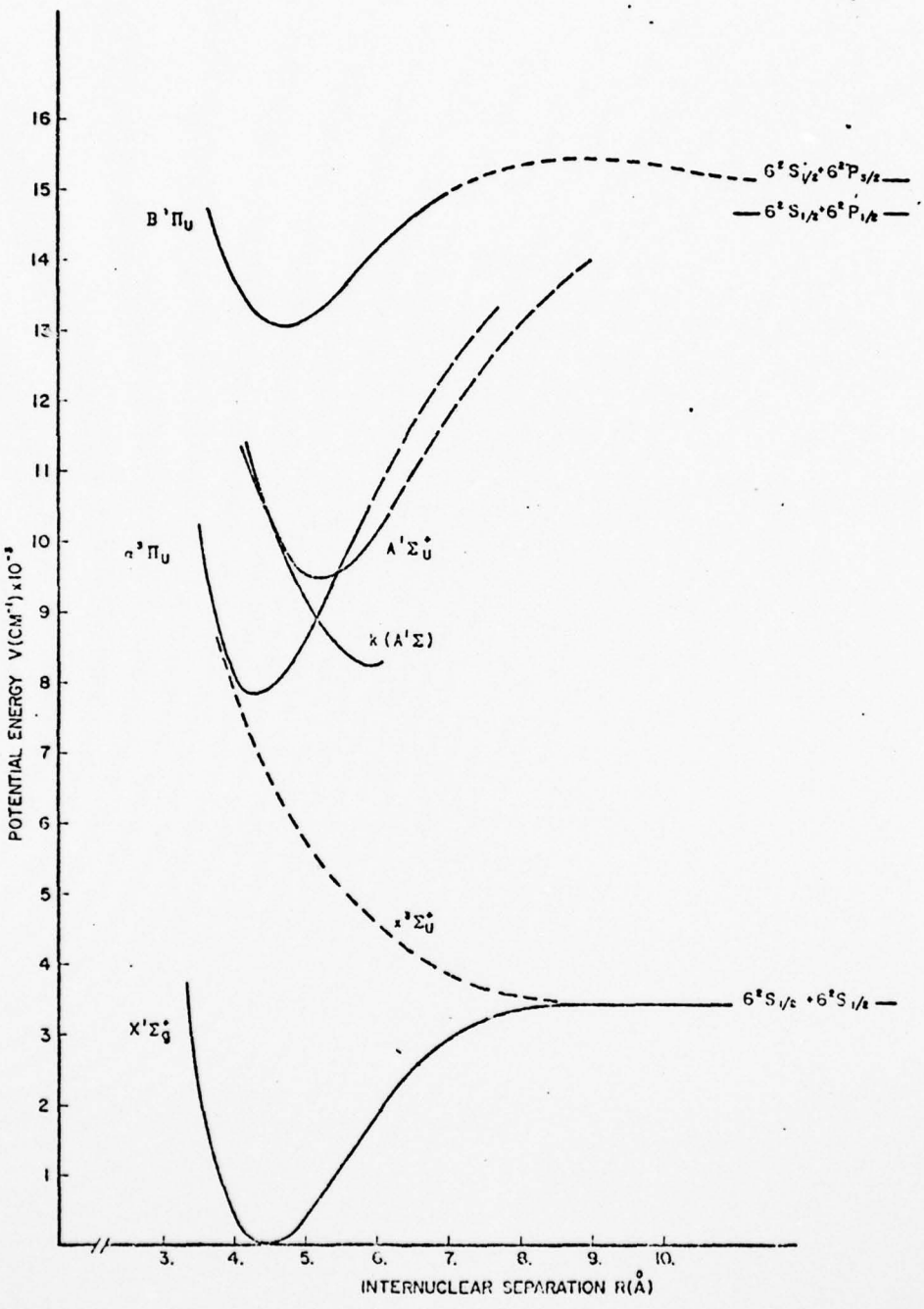

Fig 16 Cs_2 Potential Energy Curves

The technique used to calculate the potential curves is known as the Rydberg-Klein-Rees method and is explained in more detail in Appendix B. The $B^1\pi$ potential was calculated in the same manner and from spectroscopic constants of Kusch and Hessel (Ref 37). The potential is shown in Fig. 16 and the constants in Table III.

Table III

Spectroscopic Constants For Cs_2 ($X^1\Sigma_g^+$ and $B^1\pi_u$)(Ref 37)

	$X^1\Sigma_g^+$	$B^1\pi_u$
$\omega_e(cm^{-1})$	42.0267	34.3293
$\omega_e x_e(cm^{-1})$	8.3482×10^{-2}	7.9962×10^{-2}
$\omega_e y_e(cm^{-1})$	2.361×10^{-5}	1.511×10^{-4}
$\omega_e z_e(cm^{-1})$	1.5371×10^{-6}	2.86×10^{-7}
R_e(Å)	4.47	4.66
$\alpha_e(cm^{-1})$	2.635×10^{-5}	2.8×10^{-5}

The potential curve for the $A^1\Sigma$ state of Cs_2 is also shown in Fig. 16. Since the radial distribution of the photon energy, hck(R), is known from using Eq. 21 to match the spectrum, the upper state is determined by the sum of photon energy and the $X^1\Sigma$ potential energy at each R. In cm^{-1} units $k(R) = V_u(R) - V_l(R)$. Because the ground state is known reasonably well, the principle uncertainty in the upper state arises from k(R). In the CFCP analysis, where k(R) was determined, the value of k(R) could not be changed more than 100 cm^{-1} without altering the spectrum by at least 50%. This places an approximate bound on the uncertainty of the $A^1\Sigma$ potential curve. The equilibrium internuclear radius, R_e, is 5.25 Å and, therefore, the B_e of this state is considerably less than that of the ground state (0.0092 cm^{-1} vs 0.0127

cm^{-1}). Since $\alpha_e = 2.6 \times 10^{-5}$, $B_{v'} - B_{v''}$ will be negative for $v < 40$, so all the $X^1\Sigma - A^1\Sigma$ band heads will be shaded to the red. Therefore, any blue-shaded bands must arise from some other transition. The value of the vibrational constant, ω_e, was determined to be about 34 cm^{-1} by a parabolic approximation [$V \propto (R-R_e)^2$] near the bottom of the well. This compares favorably with the higher resolution (2.5 Å) absorption data which show subsidiary peaks in the $X^1\Sigma - A^1\Sigma$ spectrum with spacing of about 34 ± 2 cm^{-1}. The only other spectroscopic constant that could be estimated was the dissociation energy. Its value was about 5100 cm^{-1} assuming that the $A^1\Sigma$ state originates from the $6^2S_{1/2} + 6^2P_{1/2}$ combination of free Cs atoms. There was no information obtained in the absorption experiment that allows a determination of the parent atomic state for either the $A^1\Sigma$ or $a^3\pi$ states. The assumption is made that the $6^2S_{1/2} + 6^2P_{1/2}$ combination splits to form both the $A^1\Sigma$ and $a^3\pi$.

The $a^3\pi$ potential curve is also presented in Fig. 16. The method of construction is as follows. The Morse Potential form was used where

$$V(R) = D_e[1 - e^{\beta'(R-R_e)}]^2 \tag{33}$$

and β' is given by (Ref 29)

$$\beta' = D_e(2\pi^2 c\mu/D_e h)^{1/2} \tag{34}$$

Assuming that the spacing of the subsidiary peaks mentioned previously represents the vibrational spacing of the $a^3\pi$ state, $\omega_e = 50$ cm^{-1}. The origin of the state is assumed to be the $6^2S_{1/2} + 6^2P_{1/2}$ combination of free Cs atoms. Using the $6^2P_{3/2}$ would change D_e, but not the relative

location of the potential. The location is fixed by the wavelengths and the crossing. The middle of the gap in the spectrum, 1.165 microns, was taken as the crossing point of the $a^3\pi$ and $A^1\Sigma$. According to the CFCP analysis, this occurred at R = 5.4 Å. The only other information available was the energy of the transitions and the fact that the peaks were blue-shaded implying an R_e for the $a^3\pi$ state less than that of the $X^1\Sigma$ state, 4.47 Å. Next R_e was calculated from the known V at R = 5.4 Å and, then, the potential was calculated from Eq. 33. This approach clearly does not lead to a unique solution. The point was to show an approximate shape and location for the $a^3\pi$ state. The curve in Fig. 16 fits all the available information, as would several others, and represents a kind of average potential curve. The most significant point is that the repulsive portion of the curve will necessarily fall at very short radii which enhances the possibility of a crossing by the repulsive $x^3\Sigma$ ground state. The parameters of the $A^1\Sigma$ and $a^3\pi$ states are summarized in Table IV. One new parameter has been added, T_e, which is the energy of the potential minimum relative to the minimum of the $X^1\Sigma$ ground state.

Table IV

Spectroscopic Constants For Cs_2 ($A^1\Sigma_u^+$ and $a^3\pi_u$)

	$A^1\Sigma_u^+$	$a^3\pi_u$
ω_e (cm^{-1})	34	50
D_e (cm^{-1})	5150	6750
T_e (cm^{-1})	9470	7850
R_e (Å)	5.25	4.3

Figure 16 also shows an estimate of the $x^3\Sigma$ repulsive potential. Its location is based on a rough analogy with the location of the $X^1\Sigma$ and $x^3\Sigma$ in Na_2 and Li_2 where there are theoretical calculations of the $x^3\Sigma$ state (Refs 2,39). The main point is that the $x^3\Sigma$ and $a^3\pi$ states will approach each other in the repulsive region of the $a^3\pi$ potential. More evidence this will be presented in later sections of this chapter.

Now that the potential curves are available, the equilibrium constant can be calculated for each of the states using Eq. 27. This was done for several temperatures and the expected ratios of $[Cs_2^*]/[Cs^*]$ from $K_{eq} = [Cs_2^*]/[Cs^*][Cs]$ for the $A^1\Sigma$ state are shown in Table V. It is also possible using Eq. 1 and Eq. 21 to write I/I_o in terms of $\alpha(\nu)$. The expression becomes

$$\frac{I}{I_o} = \frac{\alpha(\nu)}{[Cs]} \frac{8\pi c}{\lambda^3} \tau_a \lambda_o \left(\frac{g_m}{g_a}\right)_u \left(\frac{g_a}{g_m}\right)_l \exp[-1.44(k - k_o)/T] \qquad (35)$$

Using this expression in Eq. 29, the ratio $[Cs_2^*]/[Cs^*]$ was calculated from the absorption data for three of the four temperatures shown in Table V. The fourth temperature, 346°C with a Cs density of 4.5×10^{16} cm^{-3}, was chosen because that is the temperature where most of the fluorescence data was taken. The absorption predicted ratio for this temperature was extrapolated from the 323°C data using the temperature dependences developed earlier. For all temperatures, the ratio predicted from the absorption gave larger numbers.

Table V

Equilibrium Molecular Fractions $[Cs_2^*]/[Cs^*]$

Temp(°C)	$[Cs](cm^{-3})$	$A^1\Sigma(K_{eq})$	$A^1\Sigma(Abs)$	$a^3\pi(K_{eq})$
250	$8.4x10^{15}$	0.35	0.40	79
305	$3.6x10^{16}$	0.42	0.50	61
323	$5.4x10^{16}$	0.43	0.53	56
346	$4.5x10^{16}$	0.23	0.29	26

The difference could be caused by the increased absorption near 1.20 microns, but more likely it is due to the sensitivity of K_{eq} to the dissociation energy of the $A^1\Sigma$ state. An increase of 60-80 cm^{-1} in D_e would bring both ratios within 5% of each other. The $D_e(A^1\Sigma)$ depends on the $D_e(X^1\Sigma)$ because the atomic states are separated by 11180 cm^{-1}. Any uncertainty in the well depth of the ground state is, therefore, an uncertainty in the upper state. Since $D_e(X^1\Sigma)$ has an uncertainty of $\pm$ 200 cm^{-1}, the range of uncertainty of $[Cs_2^*]/[Cs^*]$ from K_{eq} overlaps that from absorption. The absorption-based calculation of $[Cs_2^*]/[Cs^*]$ does not depend on the dissociation energy of either state, as can be seen in Eq. 35. Therefore, it is more likely to represent the true situation and it will be used for comparison with the fluorescence data. The conclusion from the data in Table V is that, in an equilibrium situation, 25-50% of the excited atoms should be formed into molecules. In performing these calculations, it was assumed that the $A^1\Sigma$ state dissociates into the $6^2S_{1/2} + 6^2P_{1/2}$ combination. If it goes into the $6^2P_{3/2}$, the dissociation energy would be larger and the resulting $[Cs_2^*]/[Cs^*]$ bigger since k_o would then be the D2 line. The increase would be about a factor of four depending on the temperature.